# Time Scale Analysis and Synthesis in

# Electrical Energy and Life Sciences

by

**Shaleena Jaison**

A dissertation

submitted in partial fulfillment

of the requirements for the degree of

Doctor of Philosophy in Engineering and Applied Science

College of Science and Engineering,

Idaho State University

December 2017

# Photocopy and Use Authorization

In presenting this dissertation in partial fulfillment of the requirements for an advanced degree at Idaho State University, I agree that the library shall make it freely available for inspection. I further state that permission for extensive copying of this dissertation for scholarly purposes may be granted by the Dean of the Graduate Studies, Dean of the College of Science and Engineering, or by the University Librarian. It is understood that any copying and publication of this dissertation for financial gain shall not be allowed without my written permission.

Signature: ______________________________

Date: 11-19-2017

To the Graduate Faculty:

The members of the committee appointed to examine the dissertation of Shaleena Jaison find it satisfactory and recommend that it be accepted.

______________________________Major Advisor

Dr. D. Subbaram Naidu (Professor Emeritus, Idaho State University)

______________________________Co-Advisor

Dr. R. Eugene Stuffle (Professor of Electrical Engineering)

______________________________Committee Member

Dr. S. Hossein Mousavinezhad (Professor of Electrical Engineering)

______________________________Committee Member

Dr. Ken Bosworth (Professor of Mechanical Engineering)

______________________________Committee Member

Jake P. Gentle (Industry Advisor, Idaho National Laboratory)

______________________________Graduate Faculty Representative (GFR)

Dr. Jim Creelman (Professor Emeritus of Physical & Occupational Therapy)

# Acknowledgements

I would like to thank Dr. Naidu, very much and very sincerely, for being a great advisor. I have been very fortunate to have had the opportunity to work with him for both my Master's and Ph.D. His greatness, in my eyes, has been his readiness to always make time for me, to discuss various challenging as well as the very trivial questions I might have had. In my opinion, I have come across very few professors, like him, who have students as their *first* priority. Even though he moved to the University of Minnesota, Duluth, during the early years of my Ph.D., I was very fortunate, and honored, to have continued to work with him as my advisor. I have always cherished meeting with him in person for any questions or discussions. But even while he was away, his promptness in replying to my emails, and the detailed feedback he provides through emails, relayed a sense of priority and commitment that he has towards his students. Thank you very much Dr. Naidu for your endless support and guidance, it has been a rewarding experience working with you.

I would also like to thank Dr. Stuffle, my co-advisor, for helping me with the class registrations and internship paper work. Thank you for being so kind and always ready to help.

I would also like to thank Dr. Mousavinezhad for helping me in my endeavors and his ceaseless support, especially with the Internship at Rambus, CA during my Master's. I would also like to thank him for being extraordinarily kind and for having only my best interests at heart.

I would also like to thank Dr. Bosworth for I have not seen a professor whose classes are so much fun. Being in his class I never felt intimidated by all the really menacing problems, he always had a way to explain them in a very effective and convivial manner.

I would also like to thank Dr. Creelman for accepting my request to be the GFR on my committee and for the insightful discussions at my presentation.

Besides all my professors at ISU, I am very grateful to Jake to having offered me an internship at the Idaho National Laboratory (INL) in Idaho Falls, ID, and to work for the Dynamic Line Rating Project under his mentorship.  I would also like to acknowledge the U.S. Department of Energy Wind Energy Technologies Office for supporting my internship. As an engineering student, it was a fantastic industry experience to see the theoretical and research aspects getting implemented in practice. I would also like to express my sincere gratitude to Dr. Ellis for recommending me for this tremendous opportunity to work at INL.

Finally and most importantly, I am profoundly grateful to my family for their love, support and prayers. I would like to express my deep appreciation to my husband for being my best critic. His ideas and feedback were invaluable in every step. I am very blessed to having reached this juncture in life, and, the years of my Ph.D. have been made very special, as we welcomed little *Augustus* into our lives. I have no words to thank my husband for the countless hours he watched over our baby while I dwelled in my research. I thank you very much for your unwavering love and support, and for the ceaseless words of encouragement.

# Publications

1. S. Jaison, J. P. Gentle, D. S. Naidu, "Time Scale Analysis and Synthesis for Electrical Transmission Lines in a Smart Grid", *SusTech 2015: IEEE Conference on Technologies for Sustainability*, Utah, USA, 2015.
2. J. P. Gentle, W. L. Parsons, M. R. West and S. Jaison, "Modernizing An Aging Infrastructure Through Real-Time Transmission Monitoring," in *2015 IEEE Power & Energy Society General Meeting*, Denver, CO, 2015.
3. S. Jaison, D. S. Naidu, J. P. Gentle, "Divide and Conquer Strategies for Enhanced Resiliency in Electrical Transmission Lines", *6th Resilience Engineering Association (REA) Symposium*, Lisbon, Portugal, 2015.
4. S. Jaison, D. S. Naidu, D. Zydek, "Time Scale Analysis and Synthesis of Deterministic and Stochastic Wind Energy Conversion Systems", *WSEAS Transactions on Systems and Control*, 2014.
5. S. Jaison, D. S. Naidu, D. Zydek, "Time Scale Analysis and Synthesis of Wind Energy Conversion Systems", *WSEAS – 4th International Conference on Circuits, Systems, Control and Signals*, Valencia, Spain, 2013.

# Table of Contents

# List of Figures

# List of Tables

## List of Abbreviations

| | | |
|---|---|---|
| AAC | - | All Aluminum Conductor |
| AAAC | - | All Aluminum Alloy Conductor |
| ACAR | - | Aluminum Conductor, Alloy Reinforced |
| ACSR | - | Aluminum Conductor, Steel Reinforced |
| AIDS | - | Acquired Immune Deficiency Syndrome |
| ARE | - | Algebraic Riccati Equation |
| ART | - | Antiretroviral Therapy |
| CFD | - | Computational Fluid Dynamics |
| DLR | - | Dynamic Line Rating |
| DNA | - | DeoxyriboNucleic Acid |
| EMS | - | Energy Management System |
| GHE | - | Global Health Estimates |
| GIS | - | Geographic Information Systems |
| GLASS | - | General Line Ampacity State Solver |
| HAART | - | Highly Active Antiretroviral Therapy |
| HAWT | - | Horizontal Axis Wind Turbine |
| HIV | - | Human Immunodeficiency Virus |
| IEEE | - | Institute of Electrical and Electronics Engineers |
| ISTI | - | Integrase Strand Transfer Inhibitors |
| IVP | - | Initial Value Problem |
| LQG | - | Linear Quadratic Gaussian |

| | | |
|---|---|---|
| LQR | - | Linear Quadratic Regulator |
| NRTI | - | Nucleoside Reverse Transcriptase Inhibitors |
| NNRTI | - | Non-Nucleoside Reverse Transcriptase Inhibitors |
| ODE | - | Ordinary Differential Equations |
| PI | - | Protease Inhibitors |
| PFC | - | Power Factor Correction |
| RNA | - | RiboNucleic Acid |
| RTI | - | Reverse Transcriptase Inhibitors |
| SCADA | - | Supervisory Control And Data Acquisition |
| SD-DRE | - | State Dependent – Differential Riccati Equation |
| SIR | - | Susceptible-Infectious-Recovered |
| SP | - | Singular Perturbation |
| SPaTS | | Singular Perturbation and Time Scales |
| WECS | - | Wind Energy Conversion Systems |
| WHO | - | World Health Organization |

# Nomenclature

| Time Scale Analysis and Synthesis | |
|---|---|
| ***Symbol*** | ***Description*** |
| $A$ | State matrix of high-order system |
| $A_f$ , $A_s$ | State matrices of reduced-order, fast and slow subsystems |
| $B$ | Control matrix |
| $B_f$ , $B_s$ | Control matrices of reduced-order, fast and slow subsystems |
| $C$ | Output matrix |
| $J$ | Performance index of full-order  system |
| $J_f$ , $J_s$ | Performance indices of reduced-order, slow and fast subsystems |
| $K$ | Regulator gain of full-order system |
| $K_f$ , $K_s$ | Regulator gain of reduced-order, fast and slow subsystems |
| $P$ | Algebraic Riccati equation matrix of the full-order system |
| $P_f$ , $P_s$ | Algebraic Riccati equation matrices for fast and slow subsystems |
| $Q$, $R$ | Weights of full-order system |
| $Q_f$ , $Q_s$ , $R_f$ , $R_s$ | Weights of reduced order subsystems |
| $u$ | Control vector of full order system |
| $u_f$ , $u_s$ | Fast and slow subsystems' control vectors |
| $x$ | Slow state vector |
| $x_f$ , $x_s$ | State vectors of fast and slow subsystems |
| $z$ | Fast state vector |

| Time Scale Analysis and Synthesis | |
|---|---|
| ***Symbol*** | ***Description*** |
| $\varepsilon$ | Singular perturbation parameter or small parameter |

| Overhead Power Transmission Lines | | |
|---|---|---|
| ***Symbol*** | ***Description*** | ***SI Units*** |
| $A'$ | Projected area of conductor ($m^2$/linear m) | $m^2$/linear m |
| $C$ | Solar azimuth constant | deg |
| $C_{pi}$ | Specific heat of $i^{th}$ conductor material | J/kg-°C |
| $D_0$ | Outside diameter of conductor | m |
| $H_c$ | Altitude of sun (0 to 90) | deg |
| $H_e$ | Elevation if conductor above sea level | m |
| $i_L$ | Line current | A |
| $K_{angle}$ | Wind direction factor | - |
| $K_{solar}$ | Solar altitude correction factor | - |
| $k_f$ | Thermal conductivity of air | W/(m-°C) |
| $L$ | Line inductance | H |
| $Lat$ | Degrees of latitude | deg |
| $mC_p$ | Total heat capacity of conductor | J/(m-°C) |
| $m_i$ | Mass per unit length of ith conductor material | kg/m |
| $N$ | Day of the year | - |
| $N_{Re}$ | Dimensionless Reynolds number | - |
| $q_{cn}$, $q_{c1}$, $q_{c2}$, $q_c$ | Convection heat loss rate per unit length | W/m |

| Overhead Power Transmission Lines | | |
|---|---|---|
| ***Symbol*** | ***Description*** | ***SI Units*** |
| $q_r$ | Radiated heat loss rate per unit length | W/m |
| $q_s$ | Heat gain rate from sun | W/m |
| $Q_s$ | Total solar and sky radiated heat intensity | W/m$^2$ |
| $Q_{se}$ | Total solar and sky radiated heat intensity corrected for elevation | W/m$^2$ |
| $R(T_{avg})$ | AC resistance of conductor at temperature, $T_{avg}$ | Ω/m |
| $T_a$ | Ambient air temperature | °C |
| $T_{avg}$ | Average temperature of aluminum strand layers | °C |
| $T_s$ | Conductor surface temperature | °C |
| $T_{film}$ | Average temperature of the boundary layer $(T_s + T_a)/2$ | °C |
| $T_{low}$ | Low average conductor temperature for which ac resistance is specified | °C |
| $T_{high}$ | High average conductor temperature for which ac resistance is specified | °C |
| $v_{source}$ | Source voltage of the transmission line | V |
| $V_{load}$ | Voltage drop due to a resistive load $R_{load}$ | V |
| $V_w$ | Speed of air stream at conductor | m/s |
| $Z_c$ | Azimuth of sun | deg |
| $Z_l$ | Azimuth of line | deg |
| $\alpha$ | Solar absorptivity (.23 to .91) | - |
| $\delta$ | Solar declination (–23.45 to +23.45) | deg |
| $\varepsilon$ | Emissivity (.23 to .91) | - |
| $ø$ | Angle between wind and axis of conductor | deg |

| Overhead Power Transmission Lines | | |
|---|---|---|
| ***Symbol*** | ***Description*** | ***SI Units*** |
| $\rho_f$ | Density of air | $kg/m^3$ |
| $\theta$ | Effective angle of incidence of the sun's rays | deg |
| $\mu_f$ | Absolute (dynamic) viscosity of air | kg/m-s |
| $\chi$ | Solar azimuth variable | - |
| $\omega$ | Hour angle relative to noon, 15*(Time-12), at 11AM, Time = 11 and the Hour angle= –15 deg | deg |

| Human Immunodeficiency Virus (HIV) Infection | | |
|---|---|---|
| ***Symbol*** | ***Description*** | ***SI Units*** |
| $D$ | Death rate of healthy T- cells | no. per day |
| $k$ | Virus productivity rate | no. per cell |
| $s$ | Source of healthy T- cells | no. per $mm^3$ per day |
| $u_1, u_2$ | Control variables corresponding to RTI and PI drugs | - |
| $u_{1tar}^*, u_{2tar}^*$ | Target control values | |
| $\Delta u_s^{opt}, \Delta u_f^{opt}$ | Optimal control laws for slow and fast subsystems | |
| $x_1, x_2, x_3$ | Concentration of uninfected $CD4^+$ T-cells, infected $CD4^+$ T-cells and free virus | no. per $mm^3$ |
| $x_1^*, x_2^*, x_3^*$; $x_{1tar}^*, x_{2tar}^*, x_{3tar}^*$ | Steady state and target values of states | |
| $X_1, X_2, X_3$ | Dimensionless variables of state variables $x_1$, $x_2$ and $x_3$ | - |
| $\varepsilon$ | Singular perturbation parameter | - |

| Human Immunodeficiency Virus (HIV) Infection | | |
|---|---|---|
| ***Symbol*** | ***Description*** | ***SI Units*** |
| $\mu_1$ | Death rate of viruses | no. per day |
| $\mu_2$ | Death rate of infected T- cells | no. per day |
| $\beta$ | Infectivity rate | no. per (mm$^3$ × day) |
| $\theta$ | Ratio of death rate of infected T cells to death rate of free virus- | - |

| Measles Infection | |
|---|---|
| ***Symbol*** | ***Description*** |
| $b$ | Population influx/birth rate |
| $I$ | Infected population |
| $R$ | Recovered population |
| $S$ | Susceptible population |
| $\mu$ | Death rate |
| $\alpha$ | Recovery rate |
| $\beta(t)$ | Periodic contact rate function |
| $\beta_0$ | Constant contact rate |
| $T$ | Time period of infection |

# Abstract

Control Theory and its applications span a broad spectrum of disciplines, Electrical Engineering at one end to Life Sciences at the other end. In this doctoral dissertation, research problems in Overhead Power Transmission Lines and HIV/AIDS (Human Immunodeficiency Virus /Acquired Immune Deficiency Syndrome) infection are chosen, from these vastly varied domains, for synthesizing and developing Advanced Control Strategies. This research aims to provide optimum solutions through the application of Singular Perturbation and Time Scale (SPaTS) methods, specifically, Time Scale Analysis and Synthesis. Measles, another infectious disease in Life Sciences, is briefly investigated for the application of SPaTS methods. These methods achieve model order reduction by a time scale separation procedure that guarantees excellent eigenvalue approximations of the original system. Moreover, decoupling of dynamics facilitates simple, lower order, slow and fast controllers designs, thereby enhancing the reliability of controllers and significant reduction in real-time computations. The model approximation, using this methodology does not impair the system dynamics in any way. The analysis and synthesis is carried out for deterministic optimal control problems with the objective of, mitigating perturbations in the transmission line, and developing a feasible long term HIV treatment plan with minimum side effects. The proposed control strategies are validated through extensive simulations. The results of the simulations and research provide valuable insights into the development of closed-loop, real-time, optimal controllers that are computationally more efficient and feasible for Smart Grid /Dynamic Line Rating technology and long term treatments of HIV infection.

# Chapter 1

# Background & Purpose of Research

## 1.1 Introduction

This doctoral dissertation encompasses two research problems, one in the field of Electrical Engineering and the other in the field of Life Sciences. In Electrical Engineering, the focus is on electric power systems, specifically, Overhead Power Transmission Lines. This research opportunity was presented as a funded internship[1] at the Idaho National Laboratory, Idaho Falls, ID from Summer 2014 – Summer 2015. The second research problem is in the context of Life Sciences, specifically, Infectious Diseases, with focus on Human Immunodeficiency Virus (HIV) Infection. Measles, another serious infectious disease, is briefly investigated. The research aims at designing and developing Advanced Control Strategies to provide optimum solutions using Singular Perturbation and Time Scale (SPaTS) methods, specifically, Time Scale Analysis and Synthesis. The Doctoral Dissertation further expands on the author's Master's research interests where the control principles were previously applied to Renewable Energy Systems. This chapter introduces the research problems in Electrical Engineering and Life Sciences, followed by the formulation of problem statements and purpose of research. An outline of the subsequent chapters in the report is provided at the end of this chapter.

---

[1] The research was supported by the U.S. Department of Energy Wind Energy Technologies Office contract with the Idaho National Laboratory.

### 1.1.1 Research Problem 1 – Overhead Power Transmission Lines

The energy demands of the modern world and extreme weather conditions have brought about high stresses on the existing energy infrastructure. Power outages due to severe weather conditions are likely to increase in the future as climatic changes alter the frequency and intensity of natural events [1]. These growing concerns have led to the research and development of 'smart' electric grids that will efficiently manage power demands while providing a reliable and resilient power grid for tomorrow. One of the Smart Grid Transmission & Distribution Infrastructure Metrics outlined by the U.S. Department of Energy to monitor the progress of smart grid implementation was Dynamic Line Rating (DLR) technology [2].

Overhead transmission lines are currently operated based on *static ampacity ratings* which limit the amount of electrical current that the lines can safely carry, without overheating the line and violating clearance requirements. They are determined using steady-state heat balance equations, as outlined in the national standard defined by the Institute of Electrical and Electronics Engineers (IEEE). The IEEE Standard 738 [3] provides guidelines for calculating the current–temperature relationship of bare overhead line conductors, under the assumption that electrical current, conductor temperature, and weather conditions remain constant. In other words, the static ratings are based on "near" worst case scenarios and pre-load conditions and utilities/power systems do not operate at their potential transmission capacity.

*Dynamic line ratings* of transmission lines, on the other hand, are determined based on real-time weather and load flow conditions, enabling utilities to take advantage of the additional line capacity when it is available. A simple graphic in Figure 1.1 demonstrates the concept of DLR. In areas where wind plants are being deployed, there is potential to take advantage of concurrent cooling, where wind enables wind plants to produce electricity while also cooling the existing transmission lines [4].

**Figure 1.1**: Dynamic Line Rating – concurrent cooling enables increased transmission line capacity and renewable energy integration [4]

Concurrent cooling is advantageous for power companies as it helps increasing transmission capacity limits thereby reducing operating costs for power companies and wind facilities. Figure 1.2 shows the unused headroom in transmission lines that is possible with DLR without violating the thermal limits of the conductor [5].

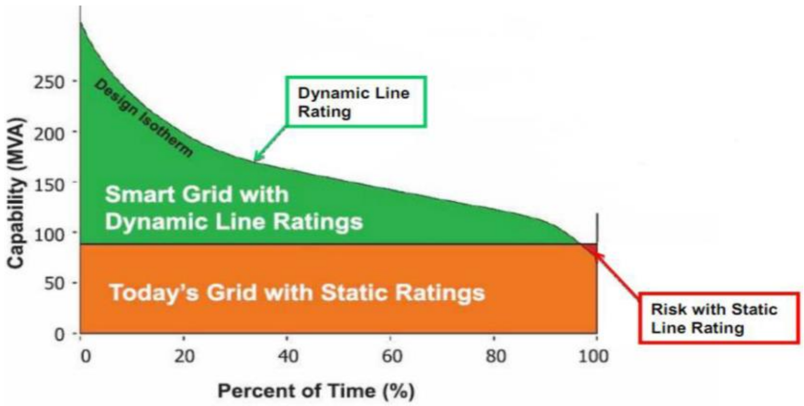


**Figure 1.2**: Dynamic line ratings vs. static line ratings for transmission lines [5], [6]

Weather components such as air temperature, solar radiation, wind speed and direction have a significant impact on the current carrying capacity of transmission lines. Research conducted at the Idaho National Laboratory (INL) corroborates this fact by showing that the cooling effect of wind, on power transmission lines could increase the current carrying capacity of the power lines by 10 to 40% [7].

Implementation of DLR technology entails real-time monitoring, management and control of power through transmission lines. Real-time monitoring becomes crucial in understanding the true ampacity of a transmission line, which requires calculations of instantaneous values of line current and line temperature. Line current and line temperature are two important dynamic variables in a transmission line that decide the amount of power that could be safely transmitted. Calculations of these two variables in real-time are considerably challenging as transmission lines involve complex electrical and thermal dynamic interactions. A thorough literature review did not result in significant information on transmission line models, which would account for both the electrical and thermal dynamics. A good reference in literature for understanding the line temperature dynamics is the IEEE Standard 738 [3]. Even though it describes the dynamics of transmission line temperature in detail, it fails to capture the electrical dynamics. This exists simultaneously and interacts with the thermal dynamics. Electrical dynamics operate at a faster time scale than thermal dynamics by virtue of its response characteristics. The simultaneous presence of slow and fast dynamics renders any system '*stiff*' for computations. The inherent time scale characteristics of a transmission line need to be captured to ensure efficient and accurate computations of line ampacity, during normal times of operation and in the event of system perturbations.

As the existing electric grid evolves into a 'smart' grid, power management decisions will become part of controller strategies to meet daily power demands. For example, utilities supplying power based on real-time demand metrics, and increasing ampacity levels of existing transmission lines based on real-time weather conditions [8]. These utility operations will be associated with the controller strategies in Energy Management Systems (EMS) and Supervisory Control And Data Acquisition (SCADA) systems, to meet daily power demands. Software control and decision making become deeply integrated into the electric power system. However, the increased dependence on cyber infrastructure in today's digital age, makes it vulnerable to malicious cyber-attacks. Thus, in addition to efficient power management, the control strategies in place must be resilient to electrical faults and malicious attacks.

This work focuses on developing a dynamic model that accounts for the electrical and thermal dynamics in a transmission line to assist implementing DLR technology. The proposed model is subjected to time scale analysis through which separation of the slow and fast dynamics is achieved. A controller design, employing Singular Perturbation and

Time Scale Methods (SPaTS), particularly, Time Scale Analysis and Synthesis is proposed that facilitates real-time implementations, while assuring stability, reliability, and resiliency of transmission lines in the event of failure/cyber-attacks.

### 1.1.2 Research Problem 2 – Human Immunodeficiency Virus (HIV) Infection

The second research problem is rooted in the field of Life Sciences. One might ask a question here: How can Engineering play a pivotal role in Life Sciences? A recent study in IEEE Transactions on Biomedical Engineering [9] underscores the importance of Engineering oriented solutions in Physical and Life Sciences. Advances in technological innovations in the field of Engineering bring cutting edge solutions that are changing how treatments are designed and drugs are delivered. This research also predicts, for the next 20 years, the direction in which research in Life Sciences is headed and the inevitable convergence of the three branches – Life Sciences, Physical Sciences and Engineering.

One of the branches of Life Sciences, is the study of *Infectious Diseases*, an interdisciplinary field that links biology, mathematics and engineering for the control and treatment of infections. Throughout human history, infectious diseases have caused suffering and mortality to large portions of the human population. 'Black Death or the Bubonic Plague', 'Spanish Flu' and Cholera epidemics, to name a few. A recent report of Global Health Estimates (GHE) by the World Health Organization (WHO) shows that infectious diseases claimed about 8.9 million lives in 2015, accounting for 15.7% of all deaths (56.4 million) in the same year [10]. These diseases are caused by pathogenic microorganisms, such as bacteria, viruses, parasites or fungi, and can be spread directly or indirectly, from one person to another.

Figure 1.3 [10] illustrates the infectious disease mortality in 2015 where major death tolls were incurred by respiratory infections, diarrheal diseases, tuberculosis and Acquired Immune Deficiency Syndrome (AIDS). Measles was reported as one of the leading causes of death among children globally and is categorized under ‘Childhood-cluster diseases’ in the figure. One of the diseases that caused about 1 million deaths in 2016 and which continues to be a pandemic is the Human Immunodeficiency Virus (HIV) infection/AIDS.

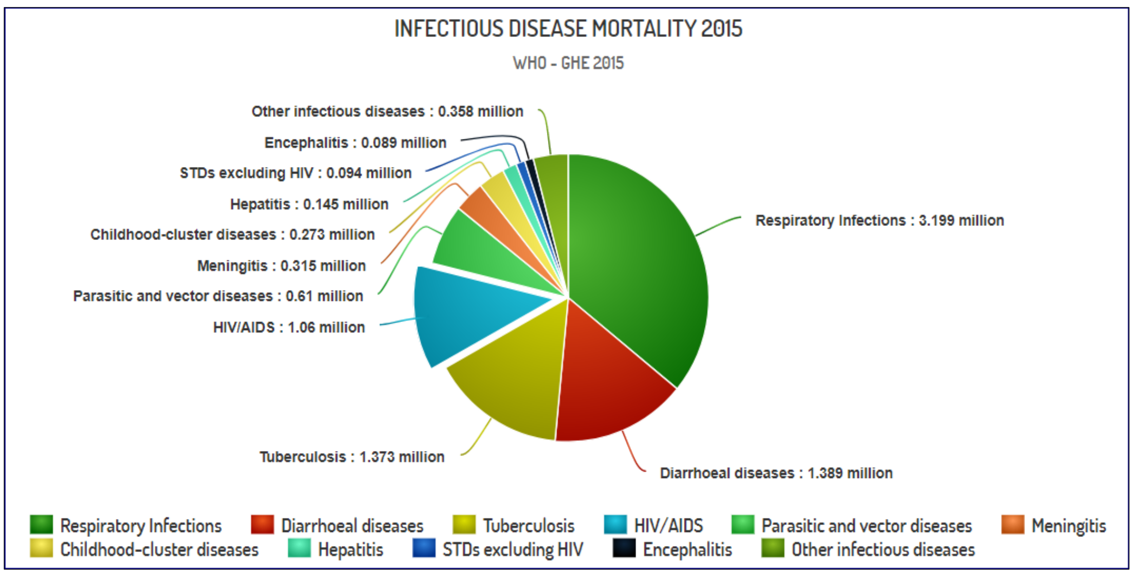


**Figure 1.3**: Mortality in 2015 due to infectious diseases [10]

HIV, the etiological agent for AIDS is a virus that attacks the immune system by depleting the key immune cells (*CD4*$^+$ T cells) that fight off infections and diseases. Loss of *CD4*$^+$ T cells makes the person susceptible to opportunistic infections and leads to the immunodeficiency that characterizes AIDS [11]. Even though HIV/AIDS was not reported in the WHO’s list of ‘2015’s top 10 leading causes of death’ [12], an estimated 36.7 million people were living with HIV, including 1.8 million children, by the end of

2016 [13]. Figure 1.4 depicts the distribution of HIV infected individuals around the globe. Eastern and southern African regions were reported to have the highest number of infected individuals compared to other parts of the world.

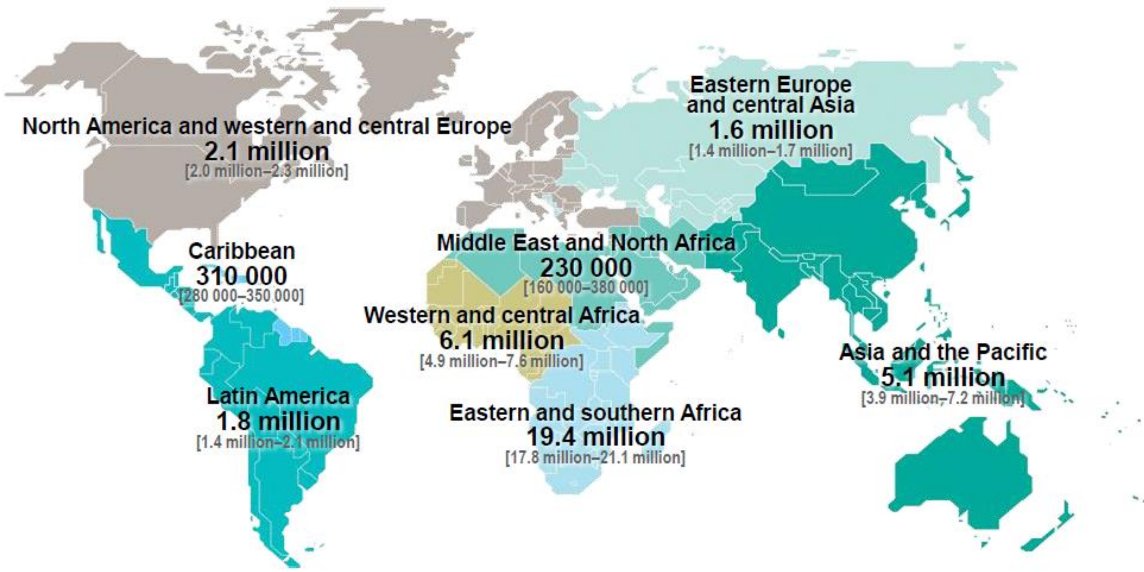


**Figure 1.4**: Global estimates of adults and children living with HIV in 2016 [14]

Since the start of the epidemic, an estimated 78 million people have become infected with HIV and 35 million people have died of AIDS-related illnesses [15]. The advent of Highly Active Antiretroviral Therapy (HAART), or Antiretroviral Therapy (ART), in 1996, was a major breakthrough in the treatment of HIV that transformed, what was once a fatal diagnosis, to a chronically managed disease [16]. HAART is a combination of different classes of medications that control viral load, delay or prevent the onset of symptoms or progression to AIDS, thereby prolonging survival in people infected with HIV and reducing the risk of HIV transmission. [16]. Figures 1.5 and 1.6 show that there has been a 16% reduction in the number of new infections since 2010 across the globe, and a reduction in AIDS related deaths from 1.5 million in the year 2000 to 1 million in 2016. A major milestone was achieved in 2016, when it was found for the first time, that more than half of all the people currently living with HIV (53%) have access to life-saving treatment [13].

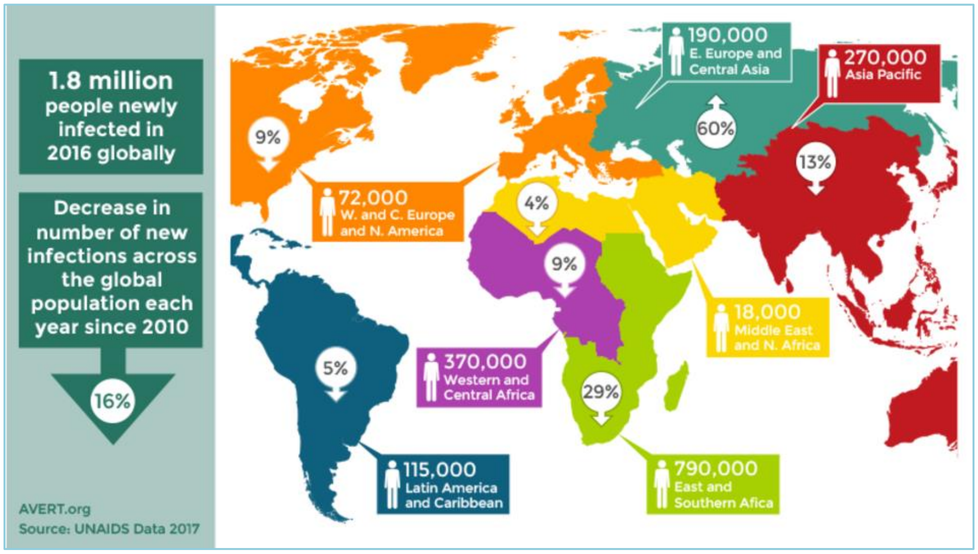


**Figure 1.5**: Number of new infections and percent changes globally since 2010 [17]

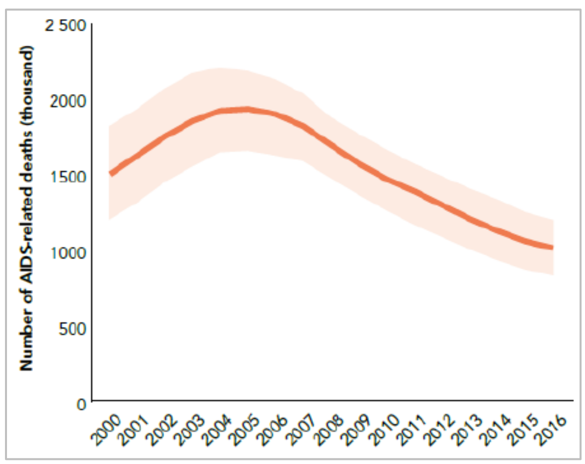


**Figure 1.6**: AIDS related deaths, all ages, global, 2000-2016 [15]

The success of ART is attributed in part, to the significant research milestones achieved in the last couple of decades and clinical trials that helped in designing these treatment strategies. ART would not be a success without the efforts undertaken by various governments and health organizations across the globe in making the treatment accessible to people in need. Mathematical modeling combined with clinical and experimental data analysis have made significant contributions towards understanding HIV dynamics, especially in areas of viral pathogenesis, virus interactions with the host, immune response to infection and ART. An abundance of mathematical models of varying complexity are found in literature that describes the HIV dynamics, immune system's response to infection, and various treatment strategies. Publications referenced in [11, 18, 19, 20, 21] are a few examples. Analysis and synthesis of optimal scheduling of drugs for HIV treatment are also a mainstream area of research, as ART comes at the cost of significant side-effects from its potent drugs. Since ART cannot clear the body of HIV, the treatment has to be continued for life [16] while minimizing its harmful side effects. This necessitates a long term, optimal chemotherapy schedule that suppresses the viral load (or boosts the patient's uninfected $CD4^+$ T cells) and minimizes the harmful effects that chemotherapy might incur. Several optimal treatment strategies have been proposed in literature that achieves this balance; a few examples are presented in [22], [23] and [24]. One of the optimal control schemes of interest due to its simplicity and robustness properties is the Linear Quadratic Regulator (LQR) [25], [26]. Even though the design procedure is straightforward for low order HIV models, the design process becomes computationally intensive when comprehensive HIV models are involved, and implementing higher order control laws for treatments may not be feasible. Models ranging from a 1$^{st}$ order [11] to 8$^{th}$ order [27] are reported in literature that takes into account of the various aspects of an HIV infection. (A list of HIV model dimensions and their references in literature are, 2$^{nd}$ order - [28] in 3$^{rd}$ order - [25], 4$^{th}$ order - [26], 5$^{th}$ order - [29], 6$^{th}$ order - [11], 7$^{th}$ order - [30], 8$^{th}$ order - [27]). Developing an optimal control law with thorough models becomes a tedious and computationally challenging task, without the aid of much needed model order reduction techniques.

One of the intrinsic features of HIV dynamics and the host systems' interactions is the *time scale* at which the dynamics occur. As pointed out in the pioneering research work by Perelson and Nelson [11], the disease AIDS, which develops on an average time span of 10 years, is characterized by very rapid dynamical processes that occur on time scales of a few hours to days, and slower processes that occur on a time scale of weeks to months. This realization was brought forth when clinical data obtained through drug trials, were interpreted by simple mathematical models of HIV dynamics. As revealed in [11] and in other publications [31, 32, 33], the slow process was identified as the declination of uninfected T-cells in the body and the fast processes were identified as rapid multiplication of virus in the body and rapid clearance rate of virus with antiretroviral drugs [11]. This slow and fast behavior categorizes the HIV dynamics into time scale systems, a special group of systems that comprehends elegant model order reduction features.

SPaTS methods are recognized in Control Theory literature [34], [35] for its exquisite model order reduction capabilities that facilitates design of simple and feasible control strategies, and guarantees excellent eigenvalue and time response approximations of the original system. The intrinsic time scale feature of the HIV dynamics provides an opportunity to design an optimal control strategy that minimizes the cost of therapy for HIV treatment, through the application of Time Scale Analysis and Synthesis.  Potential applications of SPaTS methods are briefly investigated for measles.

## 1.2 Research Problem Statements

### 1.2.1 Overhead Power Transmission Lines

Overhead power transmission lines are characterized by complex electrical and thermal dynamics. The presence of slow and fast dynamics and their interactions results in '*stiffness*' in numerical computations of line current and line temperature. Transmission line models that account for both the dynamics and its interactions are seldom found in literature, including the IEEE Standard 738, which defines the guidelines for calculating the static and dynamic ratings for transmission lines. The time scale characteristic renders real-time monitoring and controller implementation very challenging for achieving progress in DLR efforts. True ampacity values have to be calculated in real-time, and maintained at nominal values, during normal times of operation and in the event of perturbations or failures.

Investigating a dynamic model that captures the inherent *electrical and thermal* dynamics of a transmission line, and designing a stable and reliable, optimal control strategy utilizing SPaTS methods, for mitigating perturbations in a transmission line in the event of faults/attacks.

### 1.2.2 HIV Infection/AIDS

Mathematical modeling has played a key role in designing and evaluating the treatment strategies for controlling HIV/AIDS. Due to potency of the ART, long term optimal control schemes are being investigated that suppresses viral loads while keeping the side effects to a minimum. Comprehensive mathematical models accounting for various aspects of an HIV infection, could offer more insights into designing better and effective treatment plans, but the high model dimensions associated with detailed modeling pose a significant design challenge. Design of feasible and optimal treatment strategies that minimizes the viral load and cost of treatment become a complex and computationally intensive task.

Investigating an optimal control design, through the application of Time Scale Analysis and Synthesis, for suppressing viral loads while minimizing the cost of HIV treatment.

## 1.3 Purpose of Research

- To investigate and simulate, a dynamic model that accounts for the electrical and thermal dynamics of a transmission line, and perform analysis and synthesis of controllers for mitigating perturbations in transmission lines using SPaTS methods.
- To investigate and identify the inherent time scale behavior in a HIV model and design an optimal treatment scheme, for suppressing viral loads and minimizing the treatment's side effects, through the application of SPaTS methods.

The effectiveness of time scale methods is tested by designing reduced order optimal controllers (Linear Quadratic Regulators) for the proposed transmission line model and HIV infection model using SPaTS methods, and comparing it to a general, full order control design.

## 1.4 Chapter Outline

This research is organized as follows:

Chapter 2 forms the mathematical framework for the SPaTS methods. The standard representations of singularly perturbed/ time scale systems are presented, and the criteria for identifying slow-fast behavior in dynamic models are discussed. Time scale analysis method involving separation of physical systems into independent slow and fast subsystems is provided. These slow and fast subsystems form the basis of Time Scale Synthesis which results in control laws that are suitable for real-time implementations. Time scale synthesis is demonstrated for standard control laws such as state feedback and optimal control. A formulation of the general (full order) control design is also provided for comparison with the time scale design.

Chapter 3 presents the applications of time scale methods in Electrical Engineering, where the primary focus is on Overhead Power Transmission Lines. Time domain modeling of transmission lines is presented that accounts for the inherent dynamics of transmission lines. System analyses are performed, to mathematically identify the slow and fast behavior of the system. Time scale synthesis of an optimal control law for mitigating perturbations in a transmission line is presented. The efficacy of this design approach is compared to that of a general, full order, optimal control through MATLAB® simulations. Reliability and resiliency of the time scale optimal control design are also evaluated. A brief account of the research work done in the field of Renewable Energy is provided to exemplify the significance of SPaTS methods in Electrical Engineering.

Chapter 4 addresses Infectious Diseases in Life Sciences and the role of SPaTS methods in achieving an optimal treatment strategy. HIV infection is the major focus of this chapter where a time domain model of an HIV infection is analyzed and simulated to understand the dynamics of an HIV infection. The time scale behavior is explicitly indicated in the HIV model through suitable mathematical procedures. An optimal long term treatment strategy for the HIV infection is developed using time scale methods. The effectiveness of this control approach is compared to that of a full order optimal control scheme. A preliminary research on measles, conducted during the initial research period is also presented in this chapter.

Chapter 5 summarizes the significant findings of this research and the directions of future work.

# Chapter 2

# Time Scale Analysis and Synthesis

This chapter delves into the mathematical concepts underlying the theory of Singular Perturbation and Time Scales (SPaTS). A literature survey is conducted in the areas of science and engineering which emphasizes the extent of this theory's applications. Mathematical representations of singularly perturbed/ time scale systems are provided and the criteria for identifying slow-fast behavior in dynamic models are discussed. SPaTS methods, specifically Time Scale Analysis and Synthesis are presented in this research that entails separation of full order systems into slow and fast subsystems, and design of separate slow and fast controllers. The time scale design, that renders lower order control laws for achieving the desired system performance, is demonstrated for state feedback control and deterministic optimal control.

## 2.1 SPaTS Theory in Engineering & Science

SPaTS are well recognized in Control Theory, and its applications span a multitude of fields in science and engineering. An extensive survey conducted by authors in [35] is proof that SPaTS is an evolving and very active research area in systems and control engineering. This theory has presented itself as a suitable method for modeling and understanding the intricacies of physical systems in the fields of science and engineering; for example biological systems, chemical systems, nuclear systems, electrical and electronics circuits, power systems, aerospace systems, fluid dynamics and renewable energy systems [35]. SPaTS methods offer excellent model order reduction and significant computational savings, which facilitates online, real-time implementation of controllers [34]. Some of the applications of SPaTS theory in Electrical Engineering and Life Sciences are discussed below.

### 2.1.1 SPaTS in Electrical Engineering

In Electrical Engineering, an electric power system is an example where multiple time scales are observed. Dynamic processes in a power system range from lightning discharges in microseconds, to thermal dynamics in minutes [36]. Figure 2.1 portrays the various time scale phenomena in electric power systems.

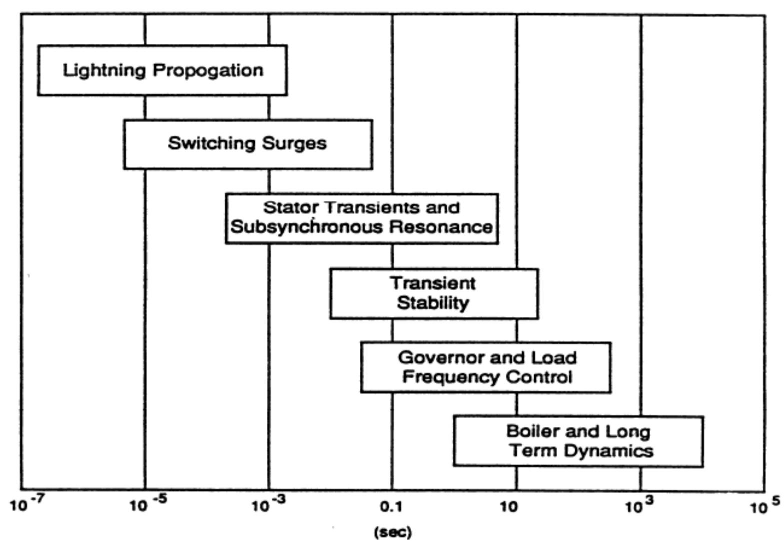


**Figure 2.1**: Time scale phenomena in electric power systems [36]

Time scales arise due to difference in speeds of response of devices. This is very evident in electro-mechanical systems. For instance, in [37], a permanent-magnet synchronous generator (PMSG) was modeled, where mechanical variables (such as generator speed, drive train torque and rotor rotational speed) constituted the slow dynamics, and electrical variables (such as generator stator currents) constituted the fast dynamics. However, time scales could also exist within purely mechanical or electrical subsystems.

Authors in [38] observed time scale nature within the mechanical systems of a wind energy conversion system. This was by virtue of the difference in inertia of the large wind turbine rotor and the relatively small inertia of the generator - drive train systems. Time scales are also observed within electrical systems, for example, in individual power system components, like transformers and IEEE Exciters [39]. In a transformer, the slow dynamics was associated to flux linkage and the fast dynamics was associated to electric voltage.

Systems identified with time scale behavior often adopt SPaTS theory to achieve model order reduction for control design purposes. Consequently, literature provides ample proof of power system models that employs SPaTS theory for reducing model dimensions. A few examples are provided here. One of them is the publication [40] in which the authors presented a method based on singular perturbation approach for sliding mode control of an induction machine. The development of control law was based on the separation of slow and fast and modes of the system. The fast dynamics of the system was assigned to zero which simplified the control design process.

A multi time-scale power system model was considered in [41] which described the dynamics of a synchronous generator, transmission line, transformer, and an induction motor load. Model order reduction of this large model was achieved by neglecting the fast dynamics (generator damping winding flux, load electromotor rotor flux) in the system. Another publication on power system modeling was presented in [42] which performed voltage stability analysis of a general power system model using SPaTS theory. The power system was represented in a standard singular perturbation (SP) form (with the small perturbation parameter, $\varepsilon$) where the fast dynamic variables were equated to zero to derive a quasi-steady state model (i.e. the reduced order model obtained by neglecting the small parameter).

DC-DC converters were analyzed in [43] where singular perturbation theory, specifically time scale separation method (of interest in this research), was employed to improve the performance of power factor correction (PFC) converters. The simulations indicated that extremely simple controllers derived from time scale separation techniques on a PFC converter produced good line current waveforms.

### 2.1.2 Time Scales in Biology and Life Sciences

As seen in Electrical Engineering, SPaTS theory are employed in a multitude of modelling and control design scenarios, in various disciplines, and Life Sciences is no exception. A literature survey in the field of Biology and Life Sciences presented an astounding number of publications that employed SPaTS methods. A few interesting examples are discussed here.

Singular perturbation theory has been applied to solve modeling problems in *biological systems*. Research presented in [44] deals with a complex biological phenomenon featuring a multi-time scale behavior, a photosynthetic process coupled with irradiance for the growth of microalgae. While the characteristic time of micro algal growth is in hours, light and dark reactions occur in milliseconds. The dynamic second order model of the system is reduced to a single dimensional model by regulating the fast dynamics. The reduced model was used to compute an optimal control law to maximize algal biomass production.

Another interesting example of SPaTS theory is in the work [45], where retroactivity phenomena in *bio-molecular systems* were studied. Retroactivity are ‘impedance – like effects’ at interconnections in biomolecular systems, both upstream and downstream, that have to be minimized for seamless signal propagation. The authors demonstrated that for an interconnected molecular system, whenever the dynamics of a system evolves on a timescale faster than its upstream system dynamics, the retroactivity to the output can be arbitrarily attenuated. This realization was achieved as a result of quasi-steady state approximations of bio-molecular system’s time scale model by the application of singular perturbation techniques. Stochastic modeling and signal processing of a nano-scale protein based *biosensor* was presented in [46] where the theory of time scales was used to understand the conductance levels of the ion channels in response to analyte concentrations.

*Epidemiology*, one of the major branches of biology that studies the factors affecting the health of populations, was seen to be benefitted by the SPaTS theory. Mathematical modeling in infectious disease epidemiology was significant in identifying possible approaches to control, including vaccination programs. Time scale theory was seen in literature as preferred tools for developing control strategies of infectious diseases. For example, authors in [47] presented an epidemic model of measles for which optimal vaccination strategies were realized using the theory of time scales. Time scale behaviour stems from the fact that the disease dynamics (short periodic outbursts) operates much faster than the human population dynamics (host's life span – births and deaths). A quasi-steady state approximation of the measles model was derived by assigning the singular perturbation parameter to zero. A similar application of time scales was observed in [48] where Song *et.al.* presented a model of tuberculosis to investigate the role of close and casual contacts in disease transmission. The theory of time scales was introduced in this paper to reduce the high model dimensions incurred by the addition of both types of contacts' dynamics in the disease model.

**Time Scales in HIV Modeling**

Most of the search results returned by search engines/databases with the keyword 'time scale' referred to the durations of the distinct phases in HIV disease progression (acute infection (2-4 weeks), clinical latency (10 years or longer) and AIDS (3 years) [49]). However, time scales with reference to singular perturbations or slow-fast behavior yielded only a few publications. One of them [50] presented a nonlinear feedback control of HIV infection with a singular perturbation approach. The presence of two time scales in HIV dynamics was identified graphically. The feedback control law was designed using singular perturbation theory which reduced the ODE of the fast viral dynamics to an algebraic equation, thereby facilitating simple control law.

A model incorporating HIV mutation and treatment with enzyme inhibitors were presented in [51] to study the long term dynamics and multiscale aspects of HIV. The model was reorganized into a standard singularly perturbed form, which was reduced into lower dimensions by equating the viral dynamics to zero.

### 2.1.3 Summary of Literature Review

From the various contributions in literature, both in Electrical Engineering and in Life Sciences, it was observed that SPaTS theory was widely adapted for reducing model dimensions of a complex *slow-fast* system. This was achieved by neglecting the *fast* dynamics in an effort to make control designs more tractable. Complexities arise due to the interactions between the slow and fast modes resulting in '*stiffness*' for mathematical computations (numeric solvers). Even though neglecting the fast dynamics facilitates ease of controller design, the solutions obtained from such a reduced order model does not satisfy all the boundary conditions of the original system [34].

SPaTS methods –Time Scale Analysis and Synthesis discussed in this work are employed to overcome the loss of boundary conditions, preserve the system dynamics and at the same time reduce model orders [34], [52].

## 2.2 Mathematical Definition of Singularly Perturbations and Time Scale Systems

Mathematically, singularly perturbed systems are described by differential equations with a small parameter '$\varepsilon$' multiplying the highest derivative of the dependent variable. The small parameter can be small time constants, masses, moments of inertias, resistances, inductances or capacitances which are responsible for increasing the order of the system.

Consider a system described by a linear second order boundary value problem [34], [52],

$$\varepsilon\ddot{x} + \dot{x}(t) + x(t) = 0, \tag{2.1}$$

with boundary conditions,

$$x(t=0) = x_i, \quad x(t=1) = x_f, \tag{2.2}$$

where the small parameter, $\varepsilon$ multiplies the highest derivative $\ddot{x}$. As $\varepsilon$ tends to zero either from positive or negative values,

$$\begin{aligned} &\lim_{\varepsilon\to 0_+}\{x(t,\varepsilon)\} = x_f e^{(1-t)},\ 0 < t \le 1, \\ &\lim_{\varepsilon\to 0_-}\{x(t,\varepsilon)\} = x_i e^{-t},\ 0 \le t < 1, \end{aligned} \tag{2.3}$$

the *degenerate (unperturbed)* problem,

$$\dot{x}^{(0)}(t) + x^{(0)}(t) = 0, \tag{2.4}$$

obtained by suppressing the small parameter, $\varepsilon$ (in (2.1)), has the boundary condition $x^{(0)}(t=1) = x_f$ if $\varepsilon$ tends to $0_+$ and $x^{(0)}(t=1) = x_i$ if $\varepsilon$ tends to $0_-$. In either case, one boundary condition is sacrificed in the process of degeneration.

The important features of singular perturbations are summarized as follows:

1. The problem (2.1) where the small parameter $\varepsilon$ is multiplying the highest derivative is called a "*singularly perturbed*" problem if the order of the problem becomes lower for $\varepsilon = 0$ than for $\varepsilon \neq 0$.
2. There exists a boundary layer where the solution changes rapidly (Figure 2.2).

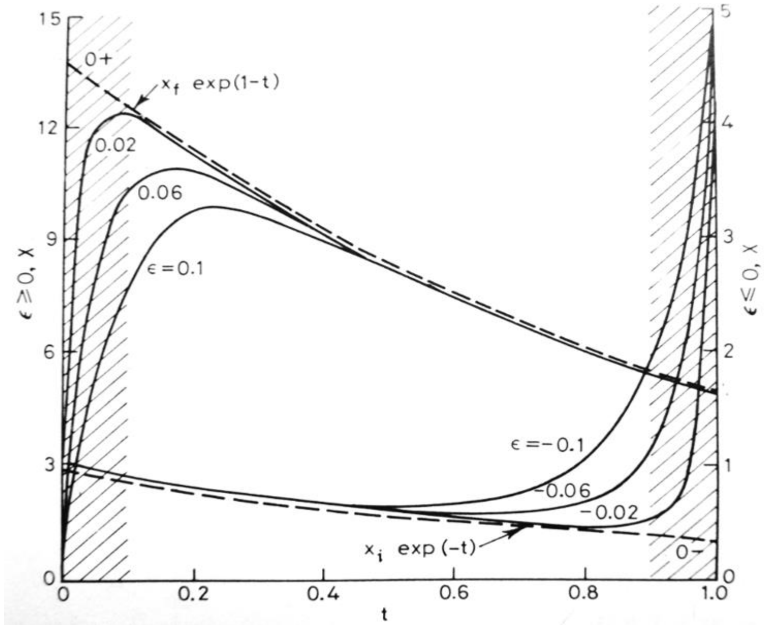


**Figure 2.2**: Boundary layer (shaded regions) represented by $0(\varepsilon)$ [52]

3. The degenerate problem, also called the "*unperturbed*" problem, is of reduced order and cannot satisfy all the given boundary conditions of the original (full, or perturbed) problem. The dashed line in Figure 2.2 represents the solution of the system (2.1) with $\varepsilon = 0$ and does not satisfy the original boundary conditions of the system, $x(t=0) = x_i$.

4. The singularly perturbed problem (2.1) has two widely separated characteristic roots giving rise to "*slow*" and "*fast*" modes in its solution. Thus, the singularly perturbed problem possesses a "two time-scale" property. The simultaneous presence of "slow" and "fast" phenomena makes the problem "*stiff*" from the numerical solution point of view.

The slow and fast phenomena are characterized by small and large time constants, or by system eigenvalues that are clustered into two disjoint sets [53]. The slow system variables correspond to the set of the eigenvalues closer to the imaginary axis, and the fast system variables are represented by the set of eigenvalues located far from the imaginary axis (Figure 2.3). The real part of the furthest eigenvalues should be at least 5 times away from the real part of the smallest eigenvalue in the group [34].

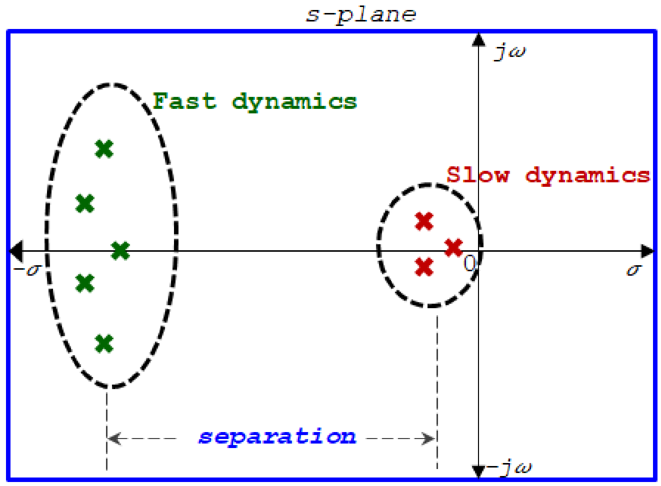


**Figure 2.3**: Eigenvalue separation for a time scale system

### 2.2.1 Standard Singular Perturbation Model

A nonlinear system exhibiting time scale behavior is expressed in the standard singular perturbation form as [34],

$$\begin{aligned} \dot{x}(t) &= f(x, z, u, \varepsilon, t), \\ \varepsilon \dot{z}(t) &= g(x, z, u, \varepsilon, t), \end{aligned} \tag{2.5}$$

where $x$ and $z$ are the $m$- and $n$- dimensional state vectors, $u$ is an $r$-dimensional control vector and $\varepsilon$ is the small, scalar, positive parameter responsible for causing singular perturbation in the sense that when $\varepsilon$ is neglected, the order of the system is reduced.

A linear singularly perturbed system is of the form,

$$\begin{aligned} \dot{x} &= A_{11}x + A_{12}z + B_{11}u, \\ \varepsilon \dot{z} &= A_{21}x + A_{22}z + B_{21}u, \end{aligned} \tag{2.6}$$

where $x$ and $z$ are the $m$- and $n$- dimensional state vectors, $u$ is an $r$-dimensional control vector and the matrices $A_{ij}$ and $B_{ij}$ are of appropriate dimensions.

## 2.3 Time Scale Analysis

The main goal of the SPaTS theory is to separate the slow and fast signals and process them independently. Time Scale Analysis is used to decouple a full order system into reduced order subsystems. The decoupling procedure relieves the system of its '*stiffness*' as the subsystems are now independent and interactions between them are minimized. This method also facilitates control design with lower order subsystems compared to a single higher order model offering significant computational savings. The other advantages of decoupling the dynamics are:

1) Reduction in on-line and off-line computational requirements,

2) Parallel and distributed processing of information,

3) Processing information independently with corresponding sampling rates (slow with slow sampling rate, fast with fast sampling rate).

4) Improved reliability of the system, due to the presence of multiple controllers in place of a single or centralized controller.

For performing a time scale analysis, the time scale system need not be in the singularly perturbed form (Section 2.2.1), i.e. a small parameter multiplying the highest derivative or some of the state variables multiplied by a small parameter. The primary requirement is that the linear system should possess widely separated groups of eigenvalues. A singularly perturbed structure is only one form of the two-time scale systems [34].

### 2.3.1 Standard Two-Time Scale System

A general representation of the two-time scale, linear system is given as [34],

$$\begin{aligned} \dot{x} &= A_1 x + A_2 z + B_1 u, \\ \dot{z} &= A_3 x + A_4 z + B_2 u, \end{aligned} \tag{2.7}$$

where $x$ and $z$ are the $m$- and $n$- dimensional state vectors, $u$ is an $r$-dimensional control vector and the matrices $A_i$ and $B_i$ are of appropriate dimensions. In this representation, $n$ eigenvalues of the system are assumed to be small and the remaining $m$ eigenvalues are large, giving rise to slow and fast responses respectively.

### 2.3.2 Decoupling Process

The decoupling into slow and fast subsystems is achieved using a two-stage linear transformation [34],

$$\begin{aligned} x_s &= x - M z_f, \\ z_f &= z + Lx, \end{aligned} \tag{2.8}$$

where the subscripts '*s*' and '*f*' denote slow and fast respectively, and $L$ ( $n \times m$ ) and $M$ ( $m \times n$ ) are solutions of the nonlinear Lyapunov-type equations,

$$\begin{aligned} LA_1 + A_3 - LA_2 L - A_4 L = 0, \\ \left(A_1 - A_2 L\right) M - M\left(A_4 + LA_2\right) + A_2 = 0. \end{aligned} \tag{2.9}$$

The slow and fast subsystems after decoupling can be represented as,

$$\begin{aligned} \dot{x}_s(t) &= A_s x_s(t) + B_s u(t), \\ \dot{z}_f(t) &= A_f z_f(t) + B_f u(t), \end{aligned} \tag{2.10}$$

where,

$$
\begin{aligned}
A_s &= A_1 - A_2 L, \\
A_f &= A_4 + L A_2, \\
B_s &= B_1 - MLB_1 - MB_2, \\
B_f &= B_2 + LB_1.
\end{aligned}
\tag{2.11}
$$

The calculation of *L* and *M* are described in the following section. From the decoupled subsystems (2.10), it is seen that variables $x_s$ and $z_f$ can be solved independently of each other.

### 2.3.3 Calculation of *L* and *M* Matrices

The *L* and *M* matrices are calculated iteratively using the high accuracy Newton method [53]. Newton's algorithm converges quadratically in the neighborhood of the sought solution, at the rate of $O(\varepsilon^{2^i})$ where $i = 1, 2... i_{max}$. This rate of convergence makes it faster than the fixed point algorithm which is another commonly found iterative method in literature with a rate of convergence of $O(\varepsilon)$. The sufficient condition for the convergence of Newton's algorithm is given in reference [54]. The iterative procedure to calculate the *L* and *M* values is given below:

Step 1: Choose the sample number of maximum iterations ($i_{max}$) for running the algorithm.

Step 2: Initialize the value of *L* and *M* as $L^{(0)} = A_4^{-1} A_3$ and $M^{(0)} = A_2 A_4^{-1}$ respectively.

Step 3: In the iterative loop, calculate the following:

$$
\begin{aligned}
&Q^{(i)} = A_3 + \varepsilon L^{(i)} A_2 L^{(i)}, \\
&D_1^{(i)} = A_4 + \varepsilon L^{(i)} A_2, \\
&D_2^{(i)} = -\varepsilon \left( A_1 - A_2 L^{(i)} \right), \\
&D_1^{(i)} L^{(i+1)} + L^{(i+1)} D_2^{(i)} = Q^{(i)}, \\
&M^{(i+1)} D_1^{(i+1)} + D_2^{(i+1)} M^{(i+1)} = A_2.
\end{aligned}
\tag{2.12}
$$

Note: The solutions of the last two equations in (2.12) are solved as Sylvester type equations which has the form,

$$AX + XB + C = 0. \tag{2.13}$$

### 2.4 Time Scale Synthesis

Once the full order system is decoupled, control laws can be implemented on the slow and fast subsystems to achieve the desired system performance. Control laws such as Proportional-Integral-Derivative (PID) control, state feedback control, optimal LQR control [38], [55], optimal Linear Quadratic Gaussian (LQG) control [38], robust $H_\infty$ control [56], and model predictive control [57] can be implemented with the time scale approach. Time scale control design differs from the conventional design process in that control laws are designed separately for each of the slow and fast subsystems, instead of one central control. This unique procedure minimizes the '*stiffness*' involved in the controller design as the slow and fast controllers process system data independently. The following sections demonstrate time scale synthesis of two standard control strategies – state feedback control and optimal LQR control. The conventional, full order control designs are presented alongside for comparison purposes.

#### 2.4.1 State Feedback Control

One of the common and simplest design approaches for physical systems represented in state space form is the state feedback control. The poles of the system are chosen to achieve a desired system response and the control law is developed such that the closed loop system delivers the desired system response. A general state feedback control is described first which is then compared to its corresponding time scale design.

### State Feedback Control – Full Order Design

The single-input system dynamics are given by,

$$\begin{aligned} \dot{x}(t) &= Ax(t) + Bu(t), \\ y(t) &= Cx(t), \end{aligned} \tag{2.14}$$

where $A$, $B$ and $C$ are the system, control and output matrices respectively. The poles of the system are given by the eigenvalues of system matrix, $A$ which influence the dynamic characteristics of the system such as sensitivity to disturbances, stability, and decay of oscillations. The goal of state feedback control is to influence the system ($A$) such that it modifies its eigenvalues to achieve the desired system response. The block diagram representing the state feedback control is represented in Figure 2.4 [58].

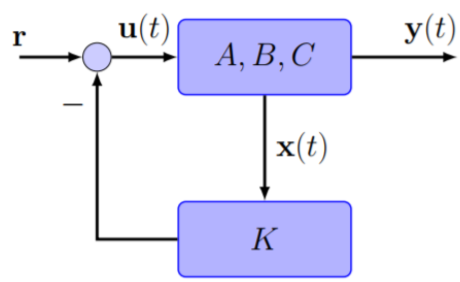


**Figure 2.4**: Simple schematic of a state-feedback control system [58]

The full-state feedback for the system is defined as,

$$u(t) = r - Kx(t), \tag{2.15}$$

where, $r$ is an external reference input having the same dimensions as $u(t)$ and $K$ is the feedback gain of the closed loop system. When $r=0$, the state feedback control becomes a state regulator. The closed loop dynamics with the state feedback control is obtained as,

$$\begin{aligned}\dot{x}(t) &= (A-BK)x(t)+Br,\\ y(t) &= Cx(t).\end{aligned} \tag{2.16}$$

The necessary and sufficient condition for arbitrary pole placement is that the pair ($A$, $B$) must be controllable, and it is assumed that all the states are measurable.

**Simple Design Example**

The control objective is to design a state feedback matrix $K$ for the system defined by,

$$\dot{x}(t) = \begin{bmatrix}1 & 1\\ 1 & 2\end{bmatrix}x(t)+\begin{bmatrix}1\\ 0\end{bmatrix}u \tag{2.17}$$

such that the poles of the closed loop system $\dot{x}(t)=(A-BK)x(t)$ is stable with the desired poles at $s$ = -5 and -25 and no overshoot.

*Design:*

The stability of the open loop system was evaluated through the roots of its characteristic equation,

$$\begin{aligned}&|sI-A| = (s-1)(s-2)-1 = s^2-3s+1=0\\ &\Rightarrow s = 2.616; 0.382 \quad \Rightarrow \textit{ unstable!}\end{aligned} \tag{2.18}$$

A unit step input response of the linear system (2.17) in MATLAB® (Figure 2.5) shows

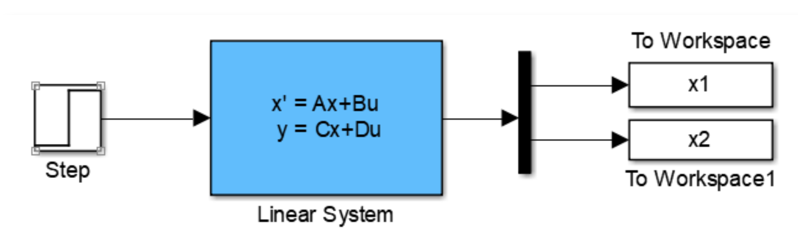


**Figure 2.5**: Simulink model for open loop system

that both the state responses were observed to be unstable as predicted by its eigenvalues (Figure 2.6).

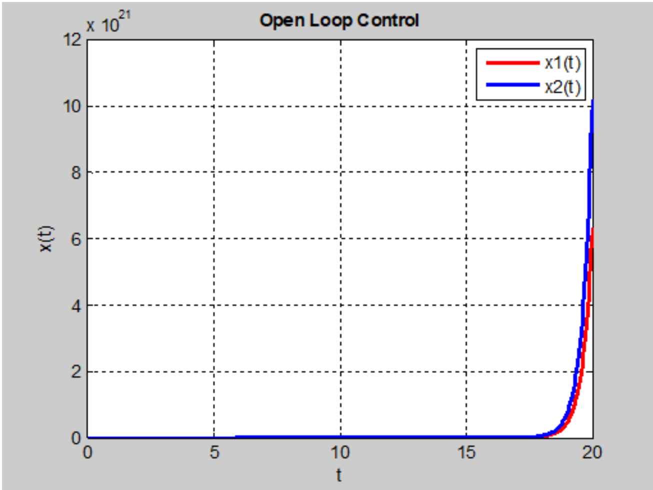


**Figure 2.6**: State response with no feedback control

The state feedback control law is defined as,

$$\begin{aligned} u &= -\begin{bmatrix} k_1 & k_2 \end{bmatrix} x(t) \\ &= -Kx(t), \end{aligned} \tag{2.19}$$

where $K$ is the state feedback gain that results in the closed loop system $\dot{x}(t) = (A - BK)x(t) + Br$ . The closed loop dynamics is defined as,

$$A - BK = \begin{bmatrix} 1 & 1 \\ 1 & 2 \end{bmatrix} - \begin{bmatrix} 1 \\ 0 \end{bmatrix} \begin{bmatrix} k_1 & k_2 \end{bmatrix} = \begin{bmatrix} 1-k_1 & 1-k_2 \\ 1 & 2 \end{bmatrix} \tag{2.20}$$

which has the characteristic equation,

$$\begin{aligned} \left| sI - (A - BK) \right| &= (s - (1 - k_1))(s - 2) - (1 - k_2) = 0 \\ &= s^2 + s(k_1 - 3) + (-2k_1 + k_2 + 1) = 0 \end{aligned} \tag{2.21}$$

The characteristic equation with the desired poles at $s$ = -5 and -25 is given by,

$$(s+5)(s+25) = s^2 + 30s + 125 = 0; \tag{2.22}$$

Comparing this equation to the closed loop characteristic equation (2.21) results in,

$$\left.\begin{array}{r} k_1 - 3 = 30 \\ -2k_1 + k_2 + 1 = 125 \end{array}\right\} \Rightarrow \begin{array}{l} k_1 = 33 \\ k_2 = 190 \end{array} \Rightarrow K = [33 \quad 190]. \tag{2.23}$$

The linear system (2.17) with feedback control (full order) was simulated in MATLAB® and is shown in Figure 2.7. The gain block in the model holds the value of –*K*.

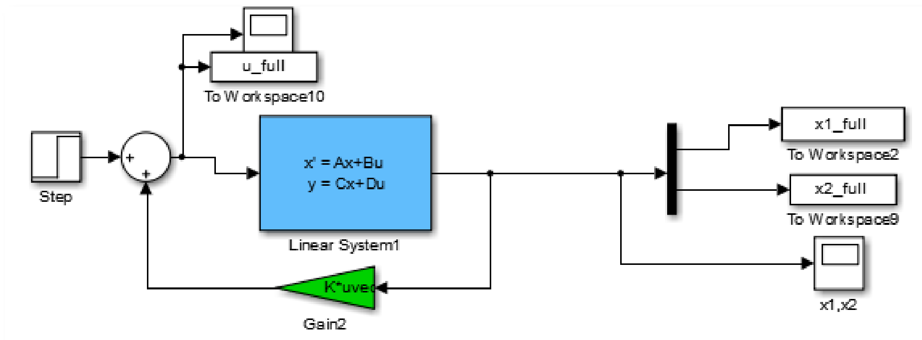


**Figure 2.7**: Simulink model for state feedback control – *full order* case

The step response of the closed loop feedback system is provided in Figure 2.8. Both states of the closed loop system were observed to be stable, with a slight overshoot for state $x_1(t)$ and zero overshoot for state $x_2(t)$.

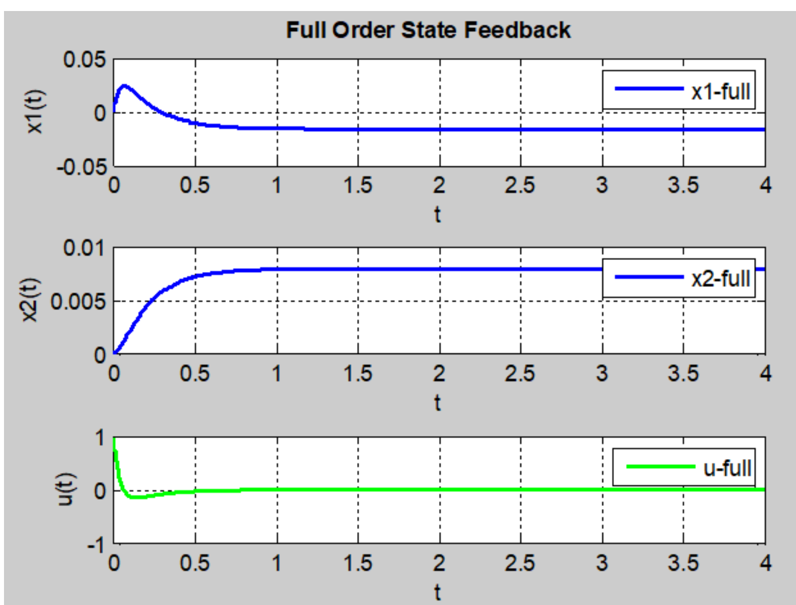


**Figure 2.8**: States of the *full order* system with feedback control

**State Feedback Control - Time Scale Synthesis**

The time scale synthesis involves separate feedback control for each of the slow and fast subsystems. The control laws for the slow and fast subsystems, $x_s(t)$ and $x_f(t)$, respectively, are defined as,

$$\begin{aligned} u_s(t) &= -K_s x_s(t), \\ u_f(t) &= -K_f x_f(t), \end{aligned} \tag{2.24}$$

where $K_s$ and $K_f$ are the slow and fast gains of the corresponding subsystems. The slow and fast control is combined to form a composite state feedback control, $u_c(t)$ which is fed back to the linear system, i.e.,

$$u_c(t) = u_s(t) + u_f(t). \tag{2.25}$$

The time scale synthesis of state feedback control is illustrated in Figure 2.9.

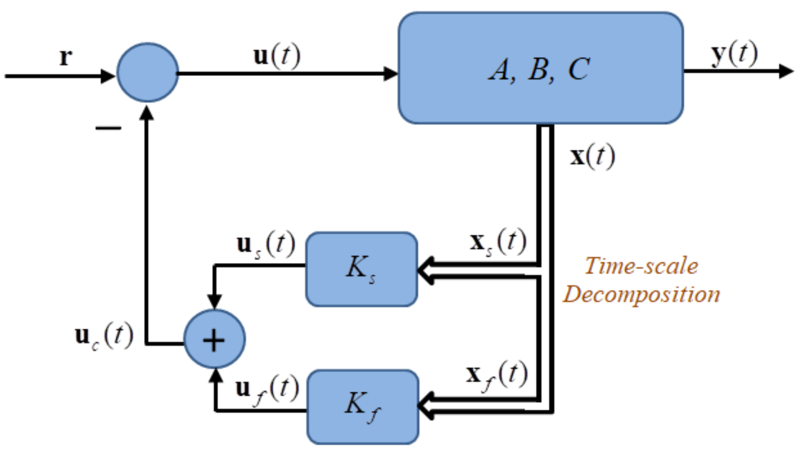


**Figure 2.9**: Time scale synthesis of state feedback control

**Slow and Fast Subsystems**

The eigenvalues of the system (2.17) were evaluated to verify time scale behavior for performing time scale analysis. The eigenvalues were found to be 0.38197 and 2.618, which are different from each other by an order of magnitude thereby verifying time scales in the system. The linear system (2.17) was then decoupled into slow and fast subsystems through time scale analysis (described in Section 2.3.2). The 1st order subsystems were obtained as,

$$\begin{aligned} A_s &= [0.38197], \quad A_f = [2.618], \\ B_s &= [0.72361], \quad B_f = [0.61803], \end{aligned} \tag{2.26}$$

The characteristic equation of the *slow* subsystem is formulated as,

$$\begin{aligned} &|sI_s - (A_s - B_s K_s)| = 0 \\ &|s - (0.3819 - 0.723K_s)| = 0 \\ &s + (-0.3819 + 0.723K_s) = 0 \end{aligned} \tag{2.27}$$

and for the fast subsystem it is,

$$\begin{aligned} &|sI_f - (A_f - B_f K_f)| = 0 \\ &|s - (2.618 - 0.618K_f)| = 0 \\ &s + (-2.618 + .618K_f) = 0 \end{aligned} \tag{2.28}$$

The desired eigenvalues have an eigenvalue separation ratio of 1:5. Keeping the same separation ratio, the eigenvalues for the time scale design were chosen as -20 (slow eigenvalue) and -100 (fast eigenvalue). The corresponding desired characteristic equations are,

$$\begin{aligned} &slow\ subsystem : (s + 20) = 0 \\ &fast\ subsystem : (s + 100) = 0 \end{aligned} \tag{2.29}$$

Comparison of closed loop and desired characteristic equation results in single order matrices $K_s$ and $K_f$ as,

$$\begin{aligned} &s + (-0.3819 + 0.723K_s) \Rightarrow s + 20; && s + (-2.618 + .618K_f) \Rightarrow (s + 100) \\ &\Rightarrow -0.3819 + 0.723K_s = 20; && \Rightarrow -2.618 + .618K_f = 100 \\ &\Rightarrow K_s = 28.191. && \Rightarrow K_f = 166.05. \end{aligned} \tag{2.30}$$

A Simulink® model for the time scale synthesis was implemented to observe the controllers' performance (Figure 2.10).

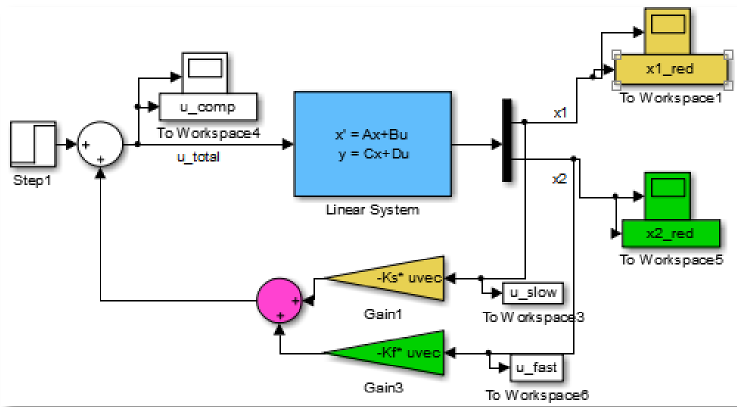


**Figure 2.10**: Simulink model for state feedback control – *reduced order* case

The state responses in Figure 2.11 indicates that the composite state feedback control was able to render the system stable, with overshoot values very similar to the full order case, i.e. zero overshoot for $x_2(t)$ and a slight overshoot for $x_1(t)$.

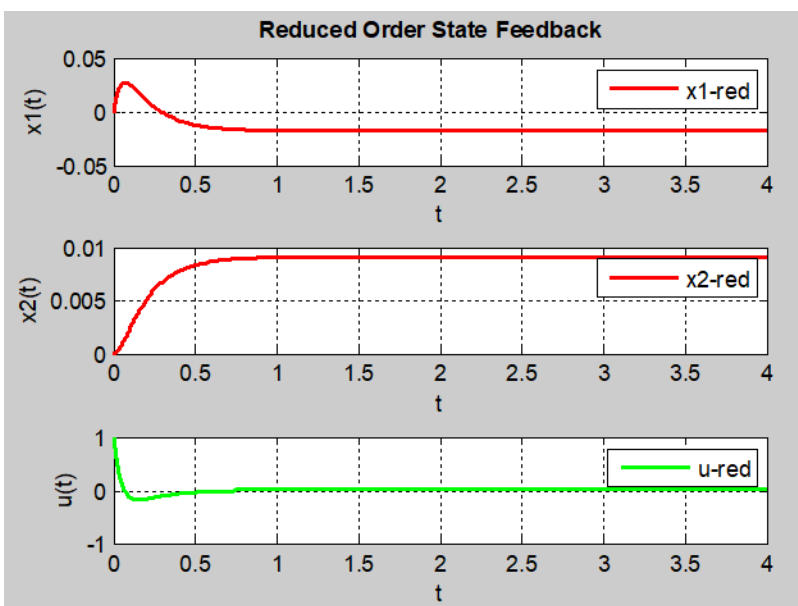


**Figure 2.11**: States of the *reduced order* system with feedback control

**Comparison of Full Order and Reduced Order Design**

The state feedback design for the full order system resulted in a $2^{nd}$ order gain matrix, $K = [33 \quad 190]$ while the time scale design resulted in two single order gains, $K_s = 28.191$ and $K_f = 166.05$. Both the designs were able to stabilize the system, and met a 'zero overshoot' requirement for one of the states. The state responses and control performance are compared in Figure 2.12. The results manifests the capabilities of the time scale synthesis that a very comparable control performance was achieved with lower order controllers. This design example could certainly be extended to complex, higher order systems for designing feasible controllers that require less online and offline computations.


**Figure 2.12**: Full order vs. reduced order state feedback control design

### 2.4.2 Optimal Control Time Scale Systems

Time scale synthesis was successfully applied to state feedback control. Another example chosen to demonstrate the scope of this design is Optimal Control. The formulation of control laws are provided in this section, and the simulation and results are presented in Chapters 3 and 4, as part of the transmission line and HIV research.

In general, an optimal control design provides the best possible performance for a given performance index or cost function. When the performance index is quadratic, and the optimization is over an infinite horizon, the resulting optimal control law obtained by minimizing the cost function is called a Linear Quadratic Regulator (LQR). In the event of perturbations, the objective of an LQR control is to bring the perturbed states to zero. It is assumed that 1) all the states are measurable, 2) the control signal is unconstrained for design purposes and 3) the system is controllable. The performance index is chosen to minimize the error between the perturbed state and the desired state (which is zero) for an infinite time period.

Conventional optimal control design involves design of a single controller for the full order system. In the following sections, time scale synthesis of LQR control is presented where separate LQR controllers are formulated for each of the slow and fast subsystems. In the following sections, LQR design of a *full order* transmission line is presented as a comparison for the *reduced order* LQR design (time scale approach).

**LQR – Full Order Design**

Given, a linear system of the form,

$$\dot{\boldsymbol{x}}(t) = A\boldsymbol{x}(t) + Bu(t), \tag{2.31}$$

where $\boldsymbol{x}$ and $u$ are the state vector and control input respectively, the performance index,

$J$ as,

$$J = \frac{1}{2}\int_{t_0}^{\infty}\left[\mathbf{x}^T(t)Q\mathbf{x}(t) + u^T(t)Ru(t)\right]dt, \tag{2.32}$$

where $Q$ and $R$ are the symmetric positive definite matrices, and the boundary conditions as $\mathbf{x}^T(t_0)$; $\mathbf{x}^T(\infty) = \begin{bmatrix}0 & 0\end{bmatrix}^T$, the optimal state, $\mathbf{x}^*(t)$ and the optimal control signal $u^*(t)$ are defined as [59],

$$\dot{\mathbf{x}}^*(t) = \left[A - BR^{-1}B^TP\right]\mathbf{x}(t), \tag{2.33}$$

$$u^*(t) = -R^{-1}B^TP\mathbf{x}^*(t) = -K\,\mathbf{x}^*(t), \tag{2.34}$$

where $P$ is the solution of the algebraic Riccati equation,

$$PA + A^TP + Q - PBR^{-1}B^TP = 0, \tag{2.35}$$

and $K$ is the regulator gain. A block diagram describing the optimal control of a full order linear system is shown in Figure 2.13. As seen in figure, all states of the system are fed to a single controller for processing the control signal.

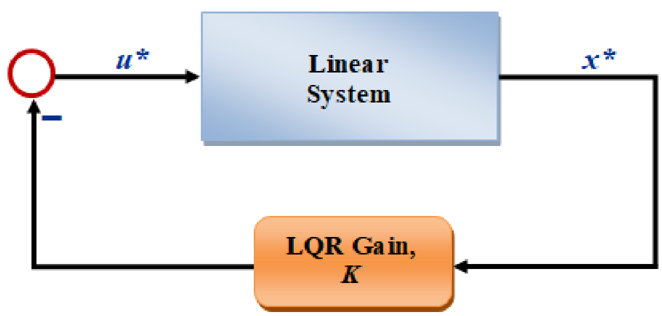


**Figure 2.13**: LQR control block diagram for the full order, linear system

### LQR – Reduced Order Design

In the time scale design, the eigenvalues of the original system are first verified and subjected to time scale analysis (Section 2.3.2) which extracts the slow and fast subsystems. The control laws are derived separately for the slow and fast subsystems, and they work in parallel towards bringing the system perturbations to zero. The slow subsystem, $x_s(t)$ defined in (2.10), has a performance index,

$$J_s = \frac{1}{2}\int_{t_0}^{\infty}\left[ x_s^T(t) Q_s x_s(t) + u_s^T(t) R_s u_s(t) \right] dt, \tag{2.36}$$

where $Q_s$ and $R_s$ are the weighting matrices for the slow subsystem. The control signal $u_s^*(t)$ for the slow subsystem is defined as,

$$u_s^*(t) = -K_s x_s(t) = -R_s^{-1} B_s^T P_s x_s(t), \tag{2.37}$$

where $K_s$ is the regulator gain of the slow subsystem and $P_s$ is the solution of the slow algebraic Riccati equation,

$$P_s A_s + A_s^T P_s + Q_s - P_s B_s R_s^{-1} B_s^T P_s = 0 \tag{2.38}$$

Similarly, for the fast subsystem, LQR control is derived as,

$$u_f^*(t) = -K_f x_f(t) = -R_f^{-1} B_f^T P_f x_f(t), \tag{2.39}$$

where $K_f$ is the regulator gain of the fast subsystem, and $P_f$ is the solution of the fast algebraic Riccati equation,

$$P_f A_f + A_f^T P_f + Q_f - P_f B_f R_f^{-1} B_f^T P_f = 0. \tag{2.40}$$

$Q_f$ and $R_f$ are the weighting matrices for the fast subsystem. The slow and fast control signals are processed independently, and fed back to the system as a *composite* control signal, $u^*(t)$ i.e.,

$$u^*(t) = u_s^*(t) + u_f^*(t). \tag{2.41}$$

A block diagram describing the time scale LQR design is presented in Figure 2.14.

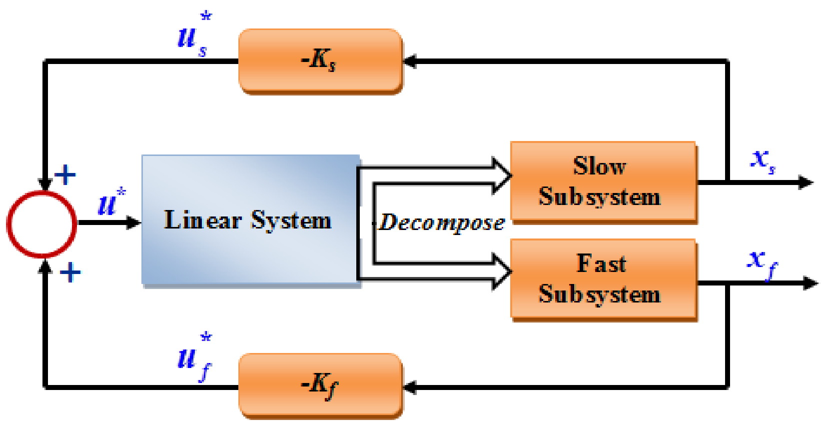


**Figure 2.14**: LQR control design using time scale approach

## 2.5 Conclusion

SPaTS methods are well recognized in control theory and its applications span numerous fields in science and engineering. Literature surveys in the field of Power System Engineering and Life Sciences revealed that these methods were applied as a means of model order reduction to make control designs more tractable. Once the model was realized in the standard singular perturbation form, the fast dynamics were neglected to simplify control design, or system information is lost in the process. To overcome the loss of system information, SPaTS methods are presented that achieve model reduction while keeping the fast dynamics intact. A decoupling process separates the full order system into slow and fast subsystems, guaranteeing excellent eigenvalue approximations of the original system. The reduced order approximations are key in designing software controllers that can be implemented real-time, as the separated subsystems are of lower order and require less computational efforts. The applications of SPaTS methods are well suited for controller design in DLR technology and smart grids, especially for power management and control, and also for designing feasible treatment strategies for an HIV infection.

# Chapter 3

# Time Scale Analysis and Synthesis in Electrical Energy

This chapter presents the applications of Time Scale Analysis and Synthesis in Electrical Engineering, with focus on Overhead Power Transmission Lines. Time domain models of overhead power transmission lines are developed and simulated to gain insights into its inherent dynamic behavior. A second order, nonlinear state space model that accounts for both electrical and thermal dynamics is presented. The eigenvalues of the system were analyzed, which indicate the slow - fast behavior of the transmission line system. Using time scale analysis, a full order transmission line model is decoupled into independent, lower order, slow and fast subsystems. These decoupled subsystems are the basis for the Time Scale Synthesis of an optimal control scheme for state regulation (Linear Quadratic Regulator). The efficacy of this control approach is compared to that of a full order optimal control design. Reliability and resiliency of Time Scale Synthesis are also discussed in this chapter. A brief overview of the application of SPaTS methods in Wind Energy Conversion Systems is provided to highlight the extent of time scale methods in Renewable Energy.

## 3.1 Introduction to Overhead Power Transmission Lines

In an electric grid, energy flows from the power generating stations to the customers over a network of overhead and underground transmission lines. Figure 3.1 [60] demonstrates various elements of a power supply network. Overhead power lines are either high voltage transmission lines (69 kV to 765 kV) that connect power plants to substations, or local distribution lines (4 kV to 69 kV) that cover shorter distances, from substations to residential/commercial customers. Overhead transmission lines are a reliable, low cost, easily maintained, and established method to transport bulk electricity across long distances. Underground transmission, on the other hand, costs approximately 4 to 14 times more than overhead lines of the same voltage and same distance, and is more complicated to construct than overhead lines due to their different physical, environmental, and construction requirements [61].

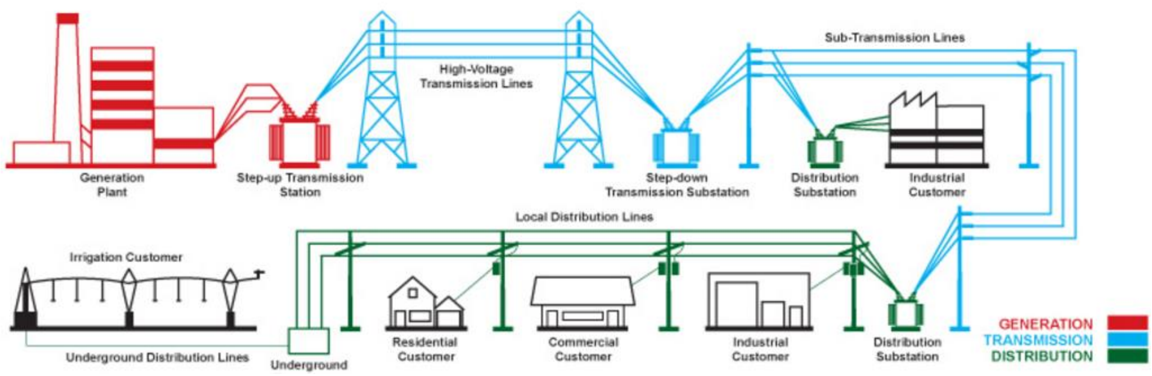


**Figure 3.1**: Electric power supply network [60]

Two significant technical challenges for underground power transmission are,

1) providing sufficient insulation so that cables can be within inches of grounded material; and 2) dissipating the heat produced during the operation of the electrical cables [61]. For these reasons, additional cabling, insulations and cooling materials are required to achieve the same reliability as overhead lines, which also translate to higher costs of installation. In contrast, overhead lines are air cooled and widely spaced for safety. Figure 3.2 [62] shows the size comparison of an underground cable to an overhead cable.

**Figure 3.2**: Underground cable and smaller overhead conductor [62]

For reasons mentioned earlier, only overhead power transmission lines are considered in this research.

### 3.1.1 Components of Overhead Power Lines

Overhead power lines are employed for transmission and distribution of electric power. A typical transmission line is displayed in Figure 3.3.

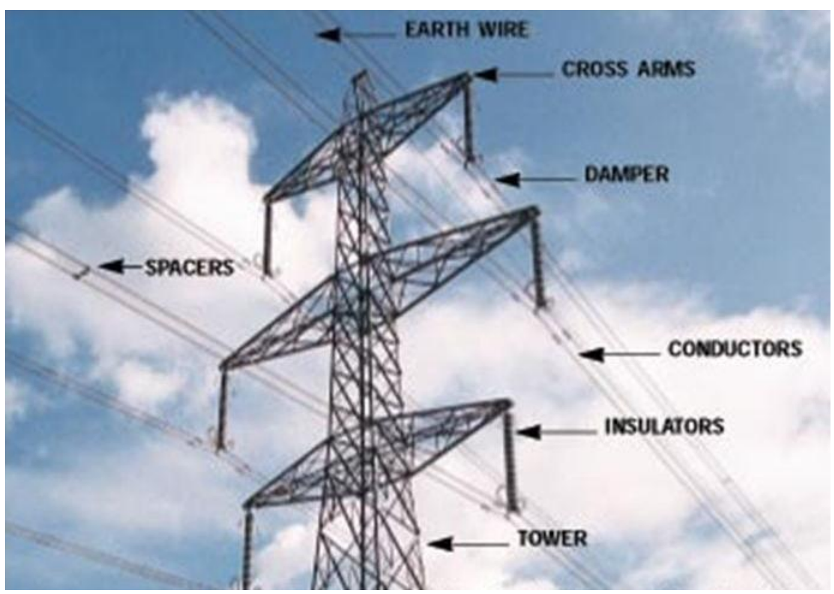


**Figure 3.3**: Components of an overhead power line [63]

In general, the main components of an overhead line are,

- Conductors – carry electric power from the generating station to the receiving end station.
- Supports – structures such as poles or towers that keep the conductors at a suitable height above the ground.
- Insulators – dead end structures that are attached to supports and insulate the conductors from the ground.
- Cross arms – provide support to the insulators.
- Dampers – reduce the vibrations and oscillations on the transmission lines due to wind.
- Spacers – prevent wind induced conductor motion damages.

### 3.1.2 Conductor Materials

Aluminum, copper, and steel are the materials commonly used in conductors. The utility industry initially transmitted electricity over copper conductors, but eventually converted to conductors made from aluminum and steel, since copper weighs and usually costs considerably more than aluminum conductor of the same resistance. Modern overhead transmission line conductors are bare, and stranded with two to four layers of aluminum over a galvanized steel core in a configuration known as Aluminum Conductor, Steel Reinforced (ACSR). Other classes of aluminum conductors that are currently employed in transmission lines are, AAC – All Aluminum Conductors, AAAC – All Aluminum Alloy Conductor and ACAR – Aluminum Conductor, Alloy Reinforced. Figure 3.4 displays the conventional conductor configurations in industry today.

ACSR is significantly stronger than AAC, AAAC and copper conductors with the same dc resistance with a minor penalty of increased external diameter and increased weight per unit length [64]. Aluminum is chosen for its excellent conductivity, low weight and low cost. The center strands of steel provide additional strength in supporting the weight of the conductor. Steel also has lower elastic and inelastic deformation (permanent elongation) due to mechanical loading (e.g. wind and ice) as well as a lower coefficient of thermal expansion under current loading. These properties allow ACSR to sag significantly less than all-aluminum conductors [65].

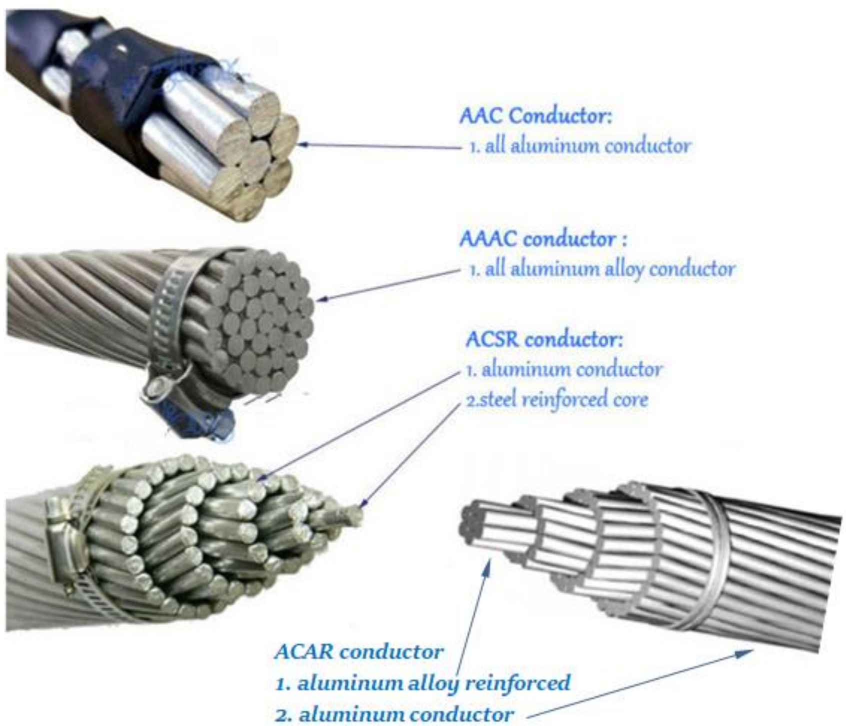


**Figure 3.4**: Overhead AAC, AAAC, ACSR and ACAR configurations [66]

This research adopts an ACSR configured overhead conductor for modeling and simulations. The numerical data provided in [3] is for a 795 kcmil 26/7 Drake ACSR conductor. The structure of an ACSR cable is provided in Figure 3.5.


**Figure 3.5**: ACSR configuration with 26 outer strands of aluminum and 7 core strands of steel [66]

### 3.2 Modeling of Overhead Transmission Lines

Transmission lines are subjected to various dynamic physical processes in the field. Some of which that cause a noticeable impact are, current flow in the line, heating effects due to line resistance, effects of weather on the line such as line cooling due to wind flow or line heating due to solar radiation.

The amount of line current (ampacity) results in a desired limiting line temperature. Line temperature on the other hand is influenced by various environmental factors. These two variables are dependent on each other and are very critical in deciding the amount of power that can be safely transmitted through a transmission line. The dynamic interactions between them are characterized by different speeds of response, which results in a slow-fast/time scale behavior. The dynamics of line current and line temperature have to be captured in transmission line models to understand their slow-fast behavior. This characteristic could be utilized to calculate real-time ampacity and limiting temperatures necessary for dynamically rating transmission lines.

### 3.2.1 Literature Review of Transmission Line Models

An extensive survey was conducted in the IEEE Xplore Digital Library for time domain models that describe the complete transmission line dynamics, or time scale nature of transmission lines. The results of the survey indicated that state space models have been studied that describe either line current dynamics or line temperature dynamics, but not both.

Authors in [67, 68, 69] present state space models of transmission lines that describe the electrical dynamics involving line currents and line voltages. These models do not include the line temperature dynamics, and hence do not offer a complete model for this research. Line temperature dynamics on the other hand, is addressed in the IEEE Standard 738 [3], which offers guidelines for calculating the current-temperature relationship of bare overhead line conductors. A single order differential equation of line temperature describes the heat exchange between the conductor and the environment, in which line current contributes towards heat gain in the conductor. In this equation, line current is a static variable and hence its dynamics is unaacounted for. The dynamic interactions between the variables or the slow-fast behavior of transmission lines are not addressed in the standard.

A literature search was also conducted on the topic of time scales in transmission lines. The results presented references that considered time scales in a general power system or in power system components. Authors in [70] addressed time scales in a single-machine infinite bus system, which is an approximation of real power systems. Power systems consist of single or multiple generators connected through transmission lines to a very large power network which is approximated by an infinite bus. The fast dynamics were identified as the flux linkages of rotor windings along direct and quadrature axes, and the slow dynamics were identified as emf, generator rotor angle and rotor speed variables. The transmission line component was not specifically accounted for in this publication.

The publication in [71] presented a three machine interconnected power system which was modeled with flux linkage and voltage regulator dynamics, and the time scales were analyzed for the whole power system. The work in [39] presented time scales on a single power system component, a transformer. Here, the slow variable had dimensions of a flux linkage and the fast variable had dimensions of a voltage.There was minimal literature on the time scale behaviour of a transmission line component.

### 3.2.2 Overhead Transmission Line Model

The lack of suitable transmission line models (electrical + thermal dynamics) in existing literature encouraged the formulation of a transmission line model from basic principles. Since the temperature dynamics was already established in the IEEE Std. 738, the electrical dynamics had to be developed. The equations for electrical dynamics were formulated through the application of Kirchhoff's laws on equivalent circuits of transmission lines. The temperature dynamics is then combined with the line current dynamics to form the suitable transmission line model for this study.

**Equivalent Circuit of a Transmission Line**

The electrical performance of overhead transmission lines are characterized by four parameters, namely resistance $R$, inductance $L$, capacitance $C$ and conductance $G$.

Parameters $R$ and $L$ constitute the series impedance, $Z$, and $C$ and $G$ constitute the shunt admittance, $Y$. These parameters are distributed along the entire line and are used to model the behavior of the voltage $V$ and current $I$ signals as they travel throughout the line, as represented in Figure 3.6 [72]. The subscripts '$S$' and '$R$' stand for the sending and receiving side respectively. The conductance, $G$ accounts for the leakage current in the insulation and active power losses due to corona effect. For a bare overhead conductor, leakage currents flow to the ground through the surface of an insulator. As leakage currents are considerably small when compared to nominal currents, the parameter $G$ is not considered in the transmission line model [64].

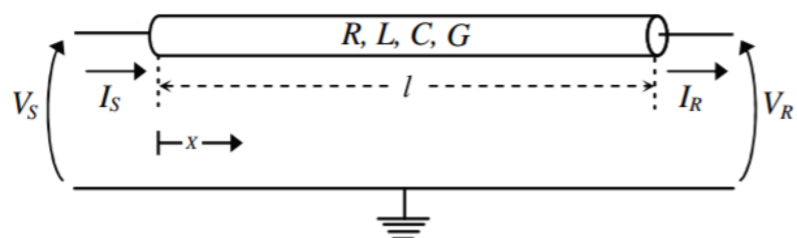


**Figure 3.6**: General representation of a transmission line [72]

Transmission line models are classified based on the length of the lines.

- Short line: 0 < length < 80 km (0 < 50 miles)
- Medium line: 80 km < length < 250 km ( 50miles < length < 155 miles)
- Long lines: length > 250 km (length > 155 miles)

Depending on the length of the transmission line, various factors come into play that limits the amount of power through a line. In short lines, resistive heating limits the amount of power that the transmission line can supply. The thermal limits are intended to to limit the conductor temperature and the resulting sag and loss of tensile strength. In longer lines, electrical phase shifts and voltage drops across the line are usually the limiting factors. DLR technology is considered primarily for short length lines where conductor temperature is the limiting factor for line ampacity.

Accurate representations of transmission lines require uniformly *distributed* parameters (series resistance, series inductance, and shunt capacitance). However, short lines and medium lines could be represented using *lumped* parameters without any appreciable loss of accuracy as well as equivalent circuits with lumped parameters [64]. In this research, a short transmission line is chosen for analysis. The equivalent circuit is drawn using a lumped parameter model consisting of only series resistance and series inductance, as the shunt capacitance at 50 or 60 Hz is very negligible.

## 3.3 State Space Modeling of Transmission Lines

A non-linear, time domain model of a short length transmission line is presented in this section. The equivalent circuit for a short line is provided in Figure 3.7.

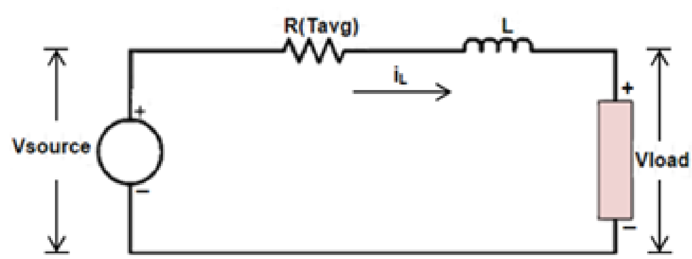


**Figure 3.7**: Equivalent circuit of a short line

In the above figure, $v_{source}$ is the source voltage representing a generator and $i_L$ is the current flowing through the line. The resistance of the transmission line, $R$ is a function of conductor temperature, $T_{avg}$ which determines the amount of current flowing through the line. The commonly used ACSR cable consists of a solid or stranded steel core surrounded by one or more layers of strands of aluminum. $T_{avg}$ denotes the average temperature of aluminum strand layers, which has excellent electrical conductivity. The line inductance, $L$ is assumed to be independent of line temperature, as observed from the datasheet values of an ACSR cable (Appendix A - Table A.3). $V_{load}$ is the voltage drop due to a resistive load $R_{load}$ at the receiving end of the line.

### 3.3.1 Line Current Dynamics

Applying Kirchhoff's voltage and current laws to the equivalent circuit, the dynamics of line current is described as,

$$\frac{di_L(t)}{dt} = -i_L(t)\frac{R(T_{avg})}{L} - i_L(t)\frac{R_{load}}{L} + \frac{v_{source}}{L}. \tag{3.1}$$

### 3.3.2 Line Temperature Dynamics

Figure 3.8 [8] illustrates the physical processes involved in the heat balance of an overhead transmission line. Joule effect and solar heating contributes to heat gain in the conductor, while convection (wind cooling) and radiation results in heat loss in the conductor.

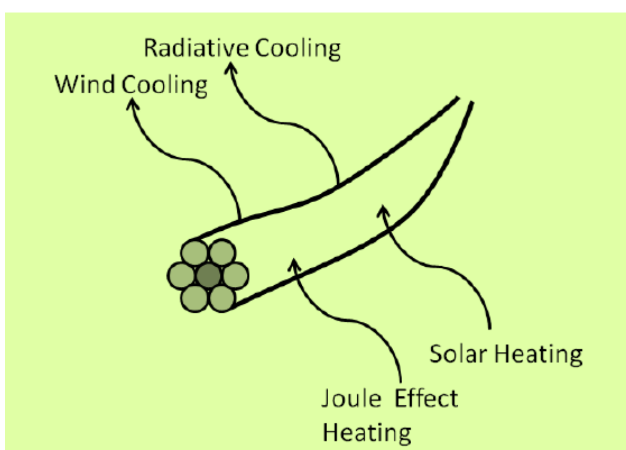


**Figure 3.8**: Heat balance within a conductor [8]

The temperature dynamics of the line is described using the non-steady state heat balance equation [3],

$$\frac{dT_{avg}(t)}{dt} = \frac{1}{mC_p}\left[ R(T_{avg}(t)) i_L^2(t) + q_s - q_c - q_r \right], \tag{3.2}$$

where $m$ is mass per unit length of the conductor and $C_p$ is the specific heat of the conductor material. Since the conductor consists of more than one material (i.e. ACSR), the conductor heat capacity is equal to the sum of the heat capacities of the core and the outer strands, each defined in this way, i.e.,

$$mC_p = \sum m_i \cdot C_{p\,i}. \tag{3.3}$$

For an ACSR conductor, the conductor heat capacity is defined as,

$$mC_p = m_{Al} \cdot C_{p\,Al} + m_{St} \cdot C_{p\,St}, \tag{3.4}$$

where $m_{Al}$ and $m_{St}$ are the mass per unit length of the outer aluminum and steel core respectively, and $C_{p\,Al}$ and $C_{p\,St}$ are the specific heats of aluminum and steel respectively.

$T_{avg}(t)$ is the average temperature of the line conductor which is a function of line current $i_L$, solar heat gain $(q_s)$, convection heat loss $(q_c)$ and radiation heat loss $(q_r)$. The physical processes involved in the heat balance of the transmission line are described in detail below.

### Joule Heating, $i_L^2 \cdot R(T_{avg})$

Joule heating or resistive/ohmic heating, is the process where the energy of an electric current is converted into heat as it flows through a resistance. The resistivity of a conductor material generally increases nonlinearly with temperature. However, for the usual operating conditions at temperatures ranging from -40°C to 75°C, the variation in resistance can be considered linear without any appreciable error [64]. The electrical resistance, $R(T_{avg})$ is assumed to be a linear function of line temperature, and is defined as [3],

$$R(T_{avg}) = \left[\frac{R_{T_{high}} - R_{T_{low}}}{T_{high} - T_{low}}\right] . \left(T_{avg}(t) - T_{low}\right) + R_{T_{low}}, \tag{3.5}$$

where $T_{low}$ and $T_{high}$ are the low and high average conductor temperatures, respectively, for which ac resistance is specified. $R_{T_{low}}$ and $R_{T_{high}}$ are the resistance values corresponding to $T_{low}$ and $T_{high}$ respectively.

### Solar Heat Gain, $q_s$

The solar heat gain, $q_s$ is defined as [3],

$$q_s = \alpha \cdot Q_{se} \cdot \sin(\theta) \cdot A', \tag{3.6}$$

where $\alpha$, $Q_{se}$, $\theta$ and $A'$ are the solar absorptivity of the conductor, total solar and sky radiated heat flux with corrected solar heat intensity, effective angle of incidence of the sun, and projected area of conductor per unit length. This $q_s$ factor along with Joule heating, $i_L^2(t) \cdot R(T_{avg})$, contributes to the increase in conductor temperature.

The angle incidence, $\theta$ is calculated using the formula,

$$\theta = \arccos\left[\cos\left(H_c\right) \cdot \cos\left(Z_c - Z_l\right)\right], \tag{3.7}$$

where $H_c$ is the solar altitude of the sun in degrees, $Z_c$ is the solar azimuth angle in degrees, and $Z_l$ is 90°, the azimuth of the transmission line in the east – west direction.

Solar altitude, $H_c$ is given by,

$$H_c = \arcsin\left[\cos(Lat)\cdot\cos(\delta)\cdot\cos(\omega)\cdot\sin(Lat)\cdot\sin(\delta)\right], \tag{3.8}$$

where *Lat* is the conductor latitude in degrees, $\delta$ is the solar declination in degrees given by,

$$\delta = 23.46\cdot\sin\left[\frac{284+N}{365}\cdot 360\right], \tag{3.9}$$

$\omega$ is the hour angle which is the number of hours from noon times 15°, and *N* is the day of the year. Solar azimuth, $Z_c$ is calculated using the equation,

$$Z_c = C + \arctan(\chi), \tag{3.10}$$

where $\chi$, the solar azimuth variable is,

$$\chi = \frac{\sin(\omega)}{\sin(Lat)\cdot\cos(\omega) - \cos(Lat)\cdot\cos(\delta)}. \tag{3.11}$$

*C* is the solar azimuth constant in degrees, a function of hour angle, $\omega$ and $\chi$ as shown in Table 3.1.

**Table 3.1:** Solar azimuth constant C – Lookup table

| **Hour Angle,** $\omega$, degrees | **C** if $\chi \geq 0$ degrees | **C** if $\chi < 0$ degrees |
|---|---|---|
| $-180 \leq \omega < 0$ | 0 | 180 |
| $0 \leq \omega < 180$ | 180 | 360 |

**Convective Heat Loss,** $q_c$

The convection heat loss $q_c$ is defined in terms of forced convection and natural convection processes.

- Forced convection heat loss equations are defined at low wind speeds ( $q_{c1}$ ) and high wind speeds ( $q_{c2}$ ), and the larger of the two is used for calculating forced convective heat loss. The equations for $q_{c1}$ and $q_{c2}$ are [3],

$$
\begin{aligned}
q_{c1} &= K_{angle} \cdot \left[1.01 + 1.35 \cdot N_{\mathrm{Re}}{}^{0.52}\right] \cdot k_f \cdot \left(T_{avg} - T_a\right), \\
q_{c2} &= K_{angle} \cdot 0.754 \cdot N_{\mathrm{Re}}{}^{0.6} \cdot k_f \cdot \left(T_{avg} - T_a\right),
\end{aligned}
\tag{3.12}
$$

where $K_{angle}$, $k_f$, $N_{\mathrm{Re}}$, and $T_a$ are the wind direction factor, thermal conductivity of air, Reynolds number and ambient air temperature, respectively. Wind direction factor, $K_{angle}$ is defined as,

$$
K_{angle} = 1.194 - \cos(\phi) + 0.194\cos(2\phi) + 0.368\sin(2\phi), \tag{3.13}
$$

where $\phi$ is the angle between the wind direction and conductor axis. Thermal conductivity of air, $k_f$ is calculated using the equation,

$$
k_f = 2.42 \cdot 10^{-2} + 7.477 \cdot 10^{-5}\left(\frac{T_{avg} + T_a}{2}\right) - 4.407 \cdot 10^{-9}\left(\frac{T_{avg} + T_a}{2}\right)^2 \tag{3.14}
$$

The Reynolds number $N_{\mathrm{Re}}$, is a dimensionless quantity which describes convective heat loss, and is defined as,

$$
N_{\mathrm{Re}} = \frac{D_0 \cdot \rho_f \cdot V_w}{\mu_f}, \tag{3.15}
$$

where $D_0$ is the outside diameter of the conductor and $V_w$ is the wind velocity. Air density, $\rho_f$ and dynamic viscosity of air, $\mu_f$ are determined using equations,

$$
\rho_f = \frac{1.293 - 1.525 \cdot 10^{-4} H_e + 6.379 \cdot 10^{-9} H_e{}^2}{1 + 0.00367\left(\dfrac{T_{avg} + T_a}{2}\right)}, \tag{3.16}
$$

$$\mu_f = \frac{1.458 \cdot 10^{-6} \left( \left( \frac{T_{avg} + T_a}{2} \right) + 273 \right)^{1.5}}{\left( \frac{T_{avg} + T_a}{2} \right) + 383.4}, \tag{3.17}$$

where $H_e$ is the elevation of conductor above sea level.

- Natural convective heat loss ( $q_{cn}$ ) dominates at zero wind speeds and is defined as,

$$q_{cn} = 3.645 \cdot \rho_f^{\ 0.5} \cdot D_0^{\ 0.75} \cdot (T_{avg} - T_a)^{1.25}, \tag{3.18}$$

where $\rho_f$ is the air density and $D_0$ is the outside diameter of the conductor. As recommended in [3], the larger of the forced and natural convection heat loss is used at low wind speeds, for calculating the convection heat loss, $q_c$.

**Radiative Heat Loss, $q_r$**

Heat loss due to radiation becomes significant when the conductor is heated above the ambient temperature. Radiative heat loss, $q_r$ is defined as,

$$q_r = 17.8 \cdot D_0 \cdot \varepsilon_0 \cdot \left[ \left( \frac{T_{avg} + 273}{100} \right)^4 - \left( \frac{T_a + 273}{100} \right)^4 \right] \tag{3.19}$$

where $\varepsilon_0$ is the conductor emissivity.

### 3.3.3 Nonlinear State Space Model

Combining equations (3.1) – (3.19), the nonlinear state space equations for a short length transmission line are,

$$\frac{di_L(t)}{dt} = -i_L(t)\frac{R(T_{avg})}{L} - i_L(t)\frac{R_{load}}{L} + \frac{v_{source}}{L},$$
$$\frac{dT_{avg}(t)}{dt} = \frac{1}{mC_p}\left[i_L^2(t)\cdot R(T_{avg}(t)) + q_s - q_c - q_r\right]; \tag{3.20}$$

Comparing the state-space model (3.20) to the standard representation of a nonlinear system, $\dot{\boldsymbol{x}} = f(\boldsymbol{x}, \boldsymbol{u}),$ the state vector $\boldsymbol{x}$ and input vector $\boldsymbol{u}$ are defined as,

$$\boldsymbol{x} = \begin{bmatrix} i_L(t) \\ T_{avg}(t) \end{bmatrix} \tag{3.21}$$

$$\boldsymbol{u} = \left[v_{source}\right] \tag{3.22}$$

where $i_L$ is the current flowing through the line, $T_{avg}$ is the average conductor temperature and $v_{source}$ is the source voltage. The model data for all the transmission line parameters are taken from the 795 kcmil 26/7 Drake ACSR conductor which were obtained through reference [3]. The model data are provided in Appendix A.

## 3.4 System Analysis of Short Transmission Line Model

The nonlinear equations of the short transmission line were simulated in MATLAB® to understand its dynamic behavior. The system was perturbed by a step change in source voltage at the origin, and the state responses were observed. The parameter values for simulating the system are listed in Table 3.2. A sample line length of 60 km was chosen for this simulation, as lengths of short transmission lines range from 0 to 80 km.

**Table 3.2**: Initial conditions for the short line model

| Parameter | Numerical Value |
|---|---|
| $v_{source}(t)$ | $v_{source}(0) = 80$ kV |
| $i_L(t)$ | $i_L(0) = 0$ A |

| Parameter | Numerical Value |
|---|---|
| $T_{avg}(t)$ | $T_{avg}(0) = 0°C$ |
| Line conductor parameters | Appendix A |
| Environmental Parameters | Appendix A |

### 3.4.1 State Response Plots

The plots of states with respect to time are displayed in Figure 3.9 and Figure 3.10. It was observed that the line current's step response was much faster than that of the line temperature, corresponding to the physical nature of electrical and thermal responses. Observing the rise time of current (near the origin), revealed it to be in the order of milliseconds, while that of temperature was in the order of minutes. This difference in the speed of variables indicates the presence of two time scales in the system, one slow and one fast. The slow variable corresponds to the thermal dynamics or line temperature and the fast dynamics corresponds to the electrical dynamics or line current.

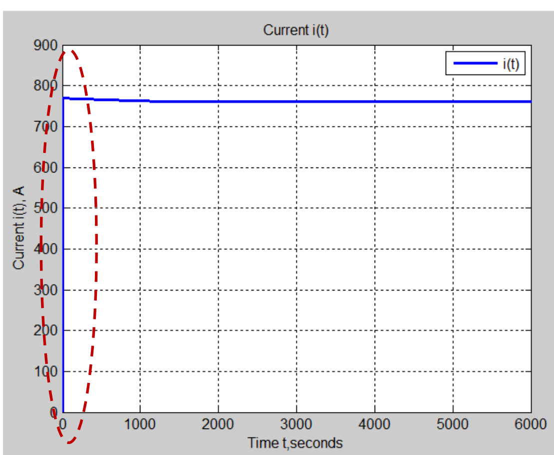


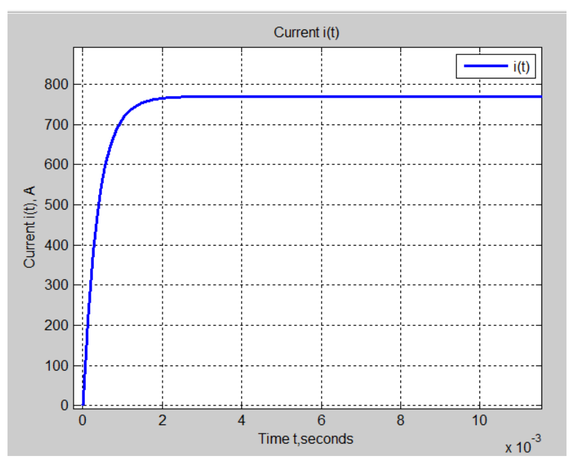


**Figure 3.9**: Plot of line current $i_L$ with respect to time (left); Detailed view of state near the origin (right)

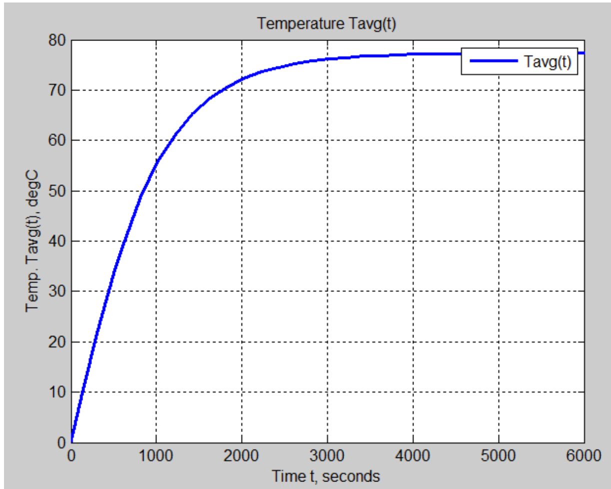


**Figure 3.10**: (a) Plot of line temperature $T_{avg}$ with respect to time

### 3.4.2 Verification with the IEEE Std. 738 Results

The non-steady state heat balance equation (3.2) is numerically implemented in the IEEE Std. 738 for a sample set of conductor and environmental parameters. A plot of the transient temperature response to a step increase in line current is provided in the standard and is shown in Figure 3.11. Line current, a static variable in the standard, is stepped from a pre-load current of 800 A to 1200 A. The initial line temperature is set at 80°C as mentioned in the standard. A simulation of the proposed dynamic model (3.20) is run in MATLAB® with the same initial conditions to compare its step responses with the IEEE standard. The results are provided in Figure 3.12. It is observed that the conductor temperature varies exponentially with time after the step change in line current, as seen in the IEEE plot. It reaches a steady state value of 127.97°C at time $t$ = 3600s and is very comparable to the value of 128°C provided in the standard. Thermal time constant of the conductor was also evaluated in the standard using a couple of methods; one was through a linear approximation of the heat balance equation (3.2) which yielded a theoretical value of 14 minutes, and the other method determined the time constant graphically from the step response plot, which yielded a value of 13 minutes. The time constant of the proposed model is observed to be 14.12 minutes which is in accordance with the theoretical calculations in the standard.

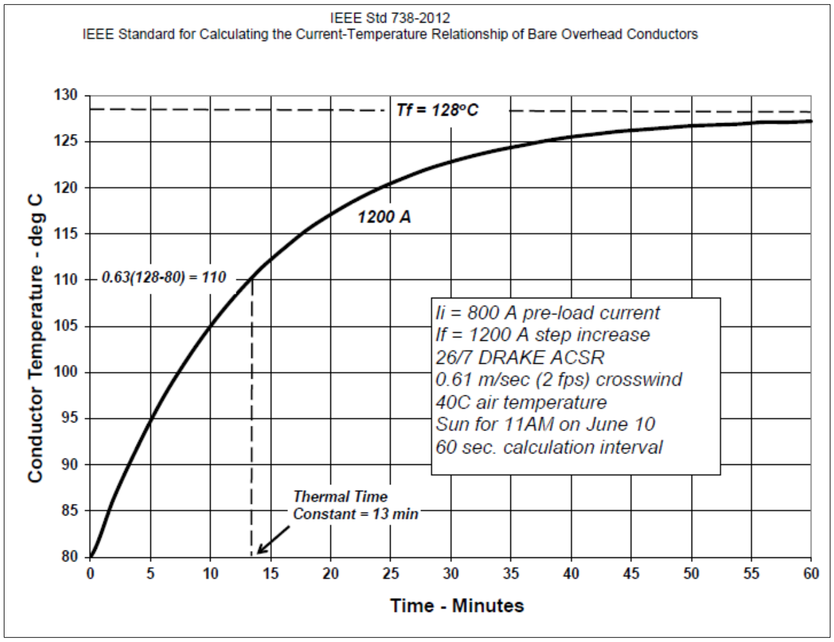


**Figure 3.11**: Transient temperature response to a step increase in line current [3]

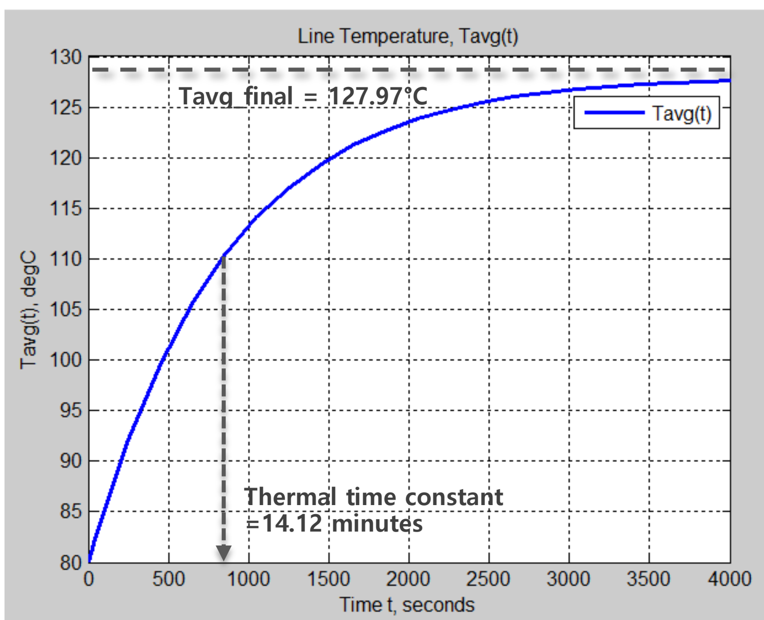


**Figure 3.12**: Conductor temperature response of the proposed model (3.20)

The simulation is also carried out for a different initial line temperature of 40°C, a value closer to that of ambient temperature. The results are observed (Figure 3.13) and the final temperature was observed to be 126.8°C at $t$ = 3600s.

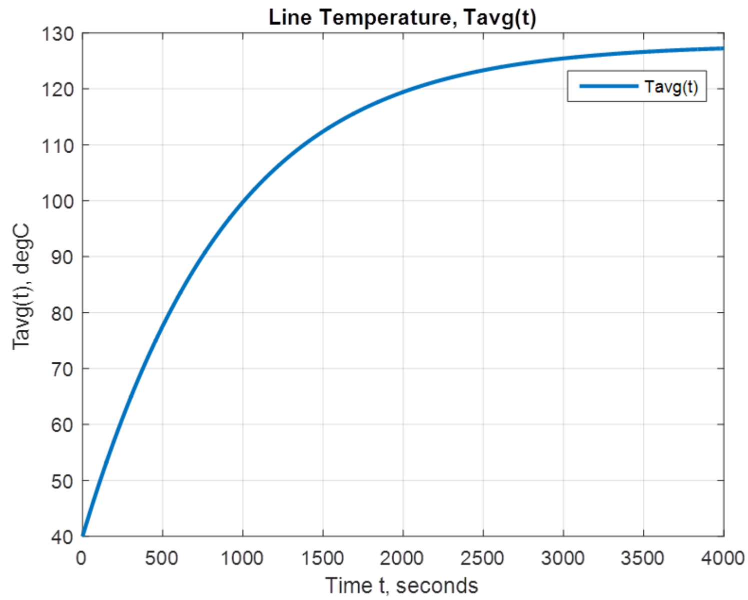


**Figure 3.13**: Temperature response of the proposed model (3.20) at $T_{avg}(0) = 40°C$

### 3.4.3 Linearization of Nonlinear Model

To further investigate on the time scale nature of the transmission line, the nonlinear model was linearized about various time instants and the eigenvalues were evaluated. The results are tabulated in Table 3.3.

**Table 3.3:** Linearization of transmission line model at various time instants

| **Time instant** | **Eigenvalues** |
|---|---|
| t = 0s | -2.6561*10^3;  -2.6102*10^-4 |
| t = 1000s | -2.6682*10^3;  -1.4177*10^-3 |
| t = 2000s | -2.6712*10^3;  -1.4478*10^-3 |

| Time instant | Eigenvalues |
|---|---|
| t = 3000s | -2.6719*10^3;  -1.4551*10^-3 |
| t = 3500s | -2.6795*10^3;  -1.4015*10^-3 |
| t = 6000s | -2.6866*10^3;  -1.4901*10^-3 |
| t = 8000s | -2.6868*10^3;  -1.4923*10^-3 |
| t = 10000s | -2.6868*10^3;  -1.4923*10^-3 |

From the table, it can be seen that the eigenvalues are different from each other by orders of magnitude. Systems characterized by such widely separated groups of eigenvalues are examples of systems with slow and fast dynamics [34]. The clearly distinct eigenvalues at any time instant signifies that the transmission line model exhibits time scales. The larger absolute eigenvalue corresponds to the faster time scale which is the line current dynamics (electrical dynamics) and the smaller absolute eigenvalue corresponds to the slower time scale which is the line temperature dynamics (thermal dynamics). Since the transmission line has variables which change at different speeds and interact with one another, it is an ideal candidate for Time Scale Analysis. The reduced order approximations obtained from this procedure are key in designing software controllers that can be implemented real-time, especially for power management and control purposes in DLR/smart grids.

### 3.5 Time Scale Analysis of Transmission Lines

The transmission line model is subjected to time scale analysis described previously in Section 2.3, where it is decoupled into lower order, slow and fast subsystems. Once separated, optimal control laws (LQR) are designed for each of the subsystems, with the objective of minimizing any perturbations in the transmission line.

### 3.5.1 Decomposition of Transmission Line Dynamics

The nonlinear model in (3.20) was linearized about a nominal operating point and the resulting linear system was of the form $\dot{x}(t) = Ax(t) + Bu(t)$, where the system and control matrices, *A* and *B* were obtained as,

$$A = \begin{bmatrix} -2687 & -485.3 \\ 0.0001684 & -0.001462 \end{bmatrix}; \qquad B = \begin{bmatrix} 25.39 \\ 0 \end{bmatrix};$$

Comparing the above linear system to the standard time scale system in (2.7) (recalled here for convenience),

$$\text{Standard Time Scale Model (2.7)} \qquad \begin{aligned} \dot{x} &= A_1 x + A_2 z + B_1 u, \\ \dot{z} &= A_3 x + A_4 z + B_2 u. \end{aligned}$$

the elements of *A* and *B* are assigned as,

$$\begin{aligned} A_1 &= [-2687], & A_2 &= [-485.3], & B_1 &= [25.39], \\ A_3 &= [0.0001684], & A_4 &= [-0.001462], & B_2 &= [0]. \end{aligned} \tag{3.23}$$

*L* and *M* were calculated iteratively using Newton's Algorithm [54]. Applying the two-stage transformation in Section 2.3.2 results in 1$^{st}$ order decoupled matrices,

$$\begin{aligned} A_s &= [\text{-}2687], & A_f &= [\text{-}0.0010289], \\ B_s &= [25.39], & B_f &= [\text{-}2.2658\text{e-}05], \end{aligned}$$

and the decoupled transmission line is of the form (2.10).

To ensure that the decoupled systems $x_s(t)$ and $x_f(t)$ retain the slow and fast dynamics, the eigenvalues of the full order and reduced order systems were compared. The results are provided in Table 3.4. The results confirm that the time scale method decouples the system dynamics almost perfectly. The accuracy parameter of Newton's algorithm could be adjusted to get the exact same eigenvalues for both the systems.

**Table 3.4:** Comparison of full order and reduced order eigenvalues

| **Full Order** | **Eigenvalues** |
|---|---|
| $A$ | eig ($A$) = -2687;<br>-0.0014924 |
| **Reduced Order** | **Eigenvalues** |
| $A_s$ - slow subsystem | eig ( $A_s$ ) = -2687 |
| $A_f$ - fast subsystem | eig ( $A_f$ ) = -0.0010289 |

With the decoupled subsystems, control laws like optimal control, Proportional-Integral-Derivative (PID) control, state feedback control, etc. can be implemented to achieve the desired system performance. In the following sections, time scale synthesis of an optimal control law is presented for minimizing perturbations in a transmission line.

### 3.6 Optimal Control Design of Transmission Lines

Transmission lines are subjected to various perturbations in the field. These could be due to the sudden loading effects by a set of electric motors, or lightning strikes, or abrupt changes in the source voltage. In such events, control strategies have to be in place that returns the system to its nominal state of operation. The control law that is implemented here is the optimal LQR control, with the objective of minimizing the perturbations to zero.

Time scale synthesis of LQR involves design of separate LQR control laws for the slow and fast subsystems. These separate controllers work in parallel and independently, towards bringing the system perturbations to zero. This *reduced order* design is compared to the conventional LQR design of a *full order* transmission line.

### 3.6.1 LQR Control of Full Order Transmission Line

The linear transmission line model is of the form,

$$\dot{\boldsymbol{x}} = A\boldsymbol{x}(t) + Bu(t), \tag{3.24}$$

where $\boldsymbol{x}^T = \begin{bmatrix} i_L(t) & T_{avg}(t) \end{bmatrix}^T$ and $u = \begin{bmatrix} v_{source} \end{bmatrix}$. The quadratic performance index, $J$ is defined as,

$$J = \frac{1}{2}\int_{t_0}^{\infty}\left[ \boldsymbol{x}^T(t)Q\boldsymbol{x}(t) + u^T(t)Ru(t) \right] dt, \tag{3.25}$$

with boundary conditions, $\boldsymbol{x}^T(t_0) = \begin{bmatrix} i_L(0) & T_{avg}(0) \end{bmatrix}^T$ and $\boldsymbol{x}^T(\infty) = \begin{bmatrix} 0 & 0 \end{bmatrix}^T$. The optimal state, $\boldsymbol{x}^*(t)$ and the optimal control signal, $u^*(t)$ are defined as [59],

$$\dot{\boldsymbol{x}}^*(t) = \left[ A - BR^{-1}B^T P \right] \boldsymbol{x}(t), \tag{3.26}$$

$$u^*(t) = -R^{-1}B^T P\boldsymbol{x}^*(t) = -K\ \boldsymbol{x}^*(t), \tag{3.27}$$

All the variables in the above equations are defined in Section 2.4.2. The optimal LQR control of a full order, linear transmission line is illustrated in Figure 3.14.

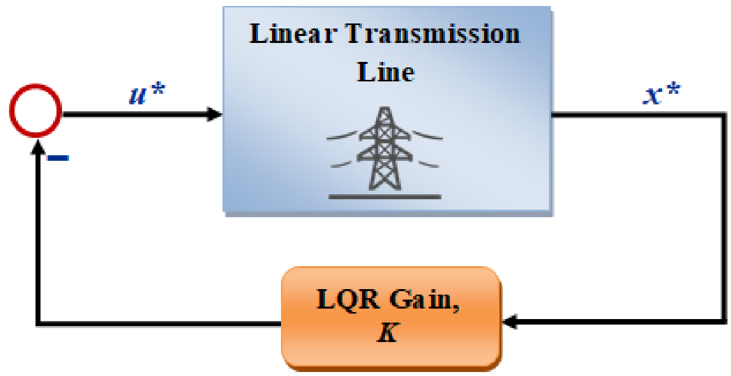


**Figure 3.14**: LQR control block diagram for the *full order* transmission line

### 3.6.2 Time Scale Synthesis of LQR Control

The optimal control law $u_s^*(t)$ for the slow subsystem is defined as,

$$u_s^*(t) = -K_s x_s(t) = -R_s^{-1} B_s^T P_s x_s(t), \tag{3.28}$$

and for the fast subsystem,

$$u_f^*(t) = -K_f x_f(t) = -R_f^{-1} B_f^T P_f x_f(t), \tag{3.29}$$

where $K_s$ and $K_f$ are the regulator gains of the slow and fast subsystems respectively. The derivation of control laws for the time scale LQR design is provided in Section 2.4.2. A block diagram describing the proposed design for the reduced order transmission line model is presented in Figure 3.15. The line current and line temperature states are separated from each other and fed to their respective controller gains, where the control signals are processed independently, and fed back to the system as a composite control signal.

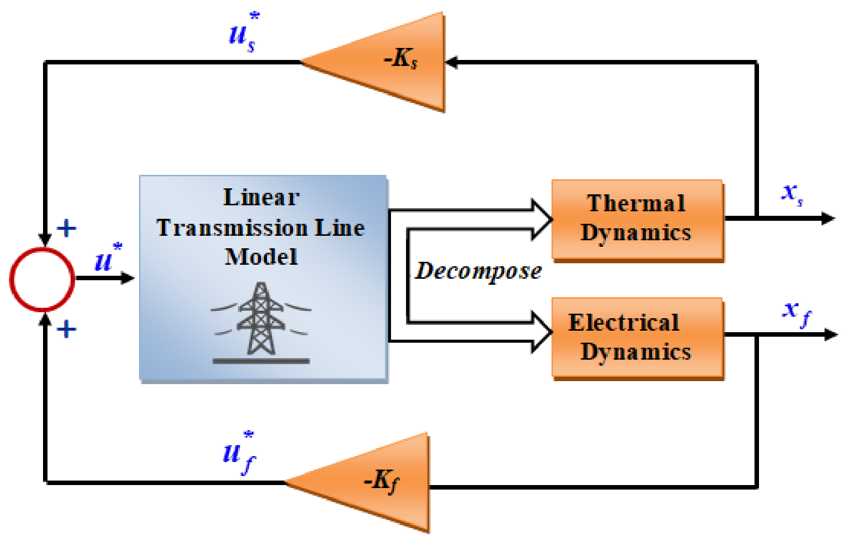


**Figure 3.15**: LQR control design for *reduced order* transmission line model

### 3.6.3 Simulation Results

All the controllers were designed in MATLAB® and implemented in Simulink®. Model data for simulations were taken from [3] for a 795 kcmil 26/7 Drake ACSR conductor. Matrices $A$, $B$, $A_s$, $B_s$, $A_f$ and $B_f$ for LQR control design were provided in Section 3.5.1. The weighting matrices $Q$, $R$, $Q_s$, $R_s$, $Q_f$ and $R_f$ were chosen such that they minimize the time taken by the states to get to zero. These matrices were chosen from multiple iterations. The controllability conditions for both the cases were tested before designing the control law.

#### Full Order LQR Control – Results

The controllability condition of the linear transmission line model system was verified using MATLAB®'s '`ctrb(A,B)`' command. The controllability matrix was found to have a full rank of 2 and the full order system was therefore controllable. The weighting matrices were chosen as,

$$Q = \begin{bmatrix} 1000 & 0 \\ 0 & 1 \end{bmatrix}; \quad R = [0.5] \tag{3.30}$$

which lead to a LQR gain,

$$K = \begin{bmatrix} 9.0613 & -1.4792 \end{bmatrix}. \tag{3.31}$$

The linear transmission line model is defined using the state-space block in the Simulink® library (Figure 3.16). The two states of the system are directed to the scope viewers using a multiplexer block '*mux*'. The state and control vectors were saved as variables in MATLAB®'s workspace using the '*simout*' blocks. The optimal control vector is obtained by applying the LQR gain, $K$ to both the states by using a de-multiplexer/'*demux*' block. The gain block holds a value of $-K$.

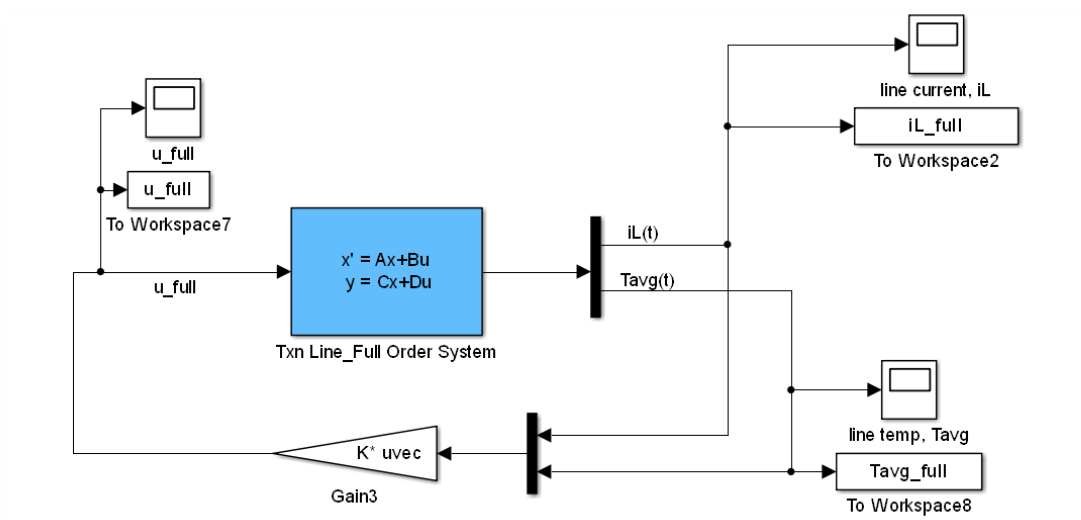


**Figure 3.16**: Simulink® model for the full order transmission line model

The plots of the states and control signal are provided in Figure 3.17. From the simulation results, it is seen that when the state variables are perturbed by some disturbances, the full order LQR control $u(t)$ brings all the states to zero.

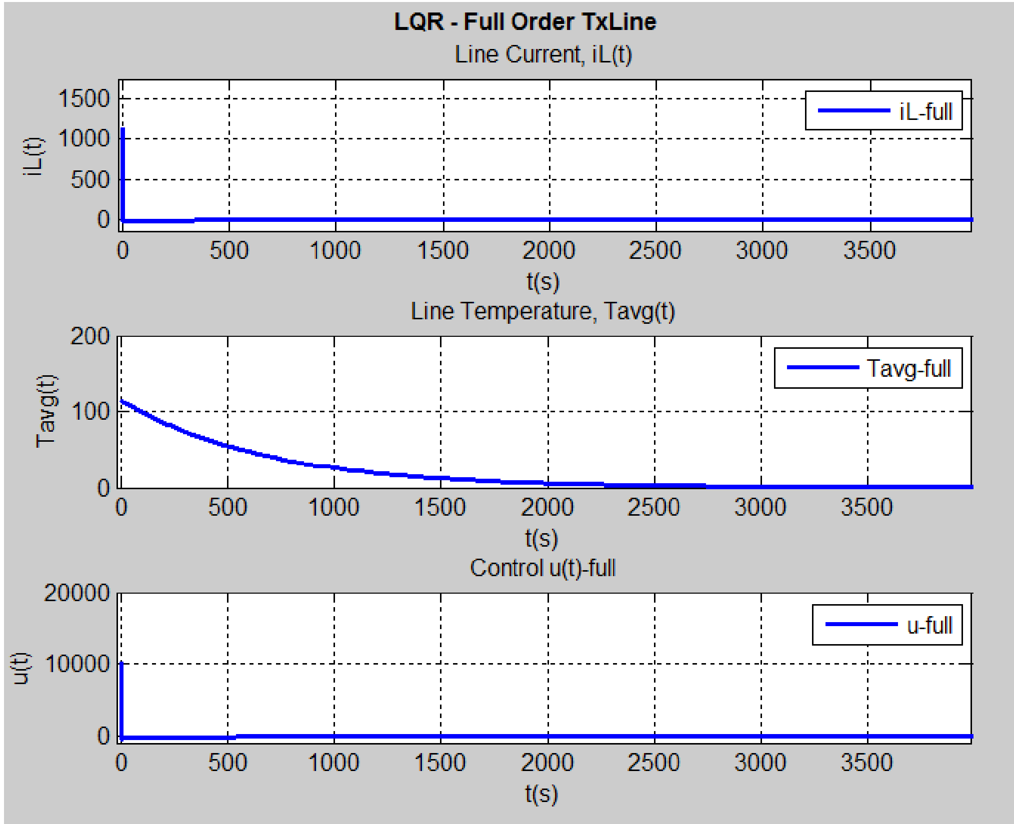


**Figure 3.17**: State and control responses of the *full order* transmission line

**Reduced Order LQR Control – Results**

The controllability matrices for each of the slow and fast subsystems were verified. A full rank of 1 was obtained for the controllability matrices for both the subsystems, and the reduced orders systems were therefore controllable. By choosing the weighting matrices as,

$$\begin{aligned} Q_s &= [10], \quad R_s = [0.25], \\ Q_f &= [1], \quad R_f = [1], \end{aligned} \tag{3.32}$$

the slow and fast gains were calculated to be,

$$K_s = [\ 0.18882]; \quad K_f = [-0.017092], \tag{3.33}$$

respectively. The Simulink® model was built for the reduced order transmission line as shown in Figure 3.18. The slow optimal gain, $K_s$ was applied to $T_{avg}(t)$ (line temperature) and $K_f$ was applied to $i_L(t)$ (line current). The plots of the states and control signal are provided in Figure 3.19 . The perturbed states of the reduced order system tend to zero as time tends to infinity.

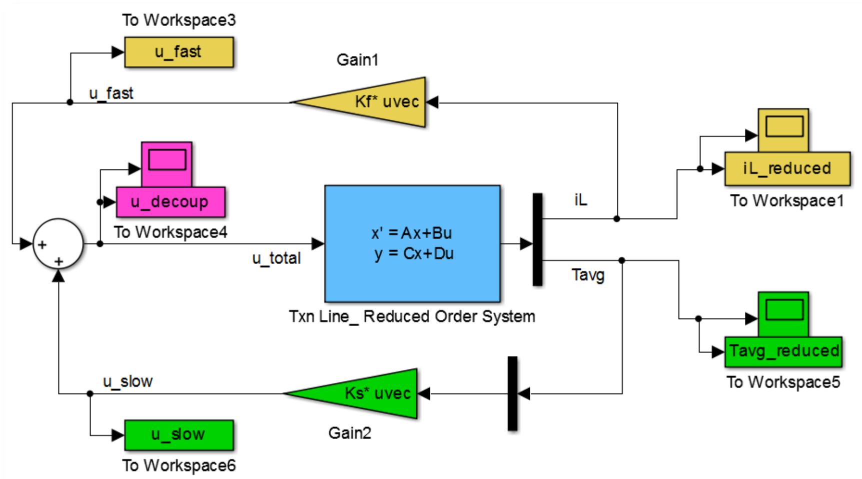


**Figure 3.18**: Simulink® model for the reduced order transmission line

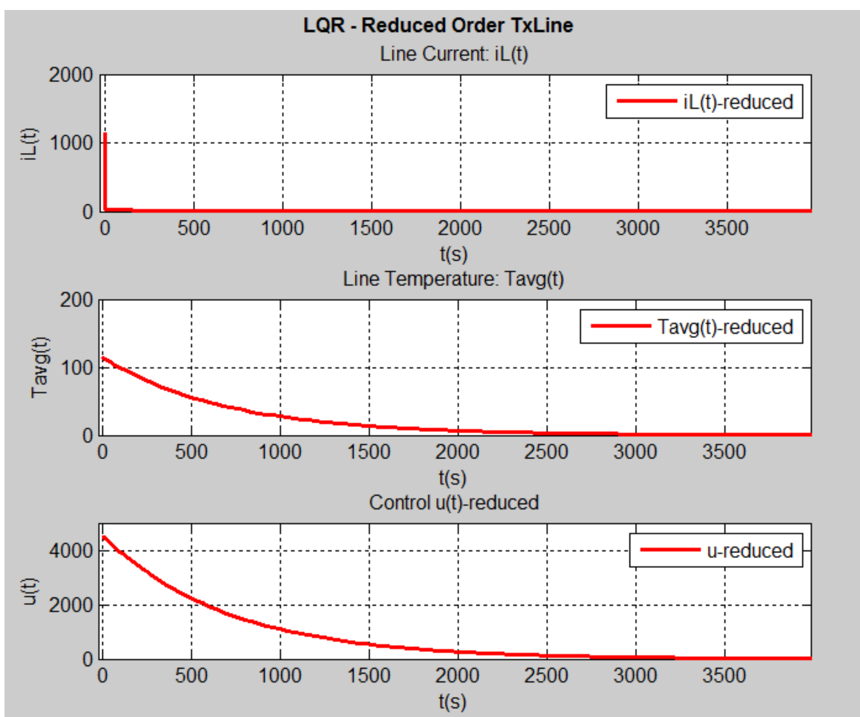


**Figure 3.19**: State responses and control signal of the *reduced order* transmission line

### Comparison of Full Order and Reduced Order LQR Design

A comparison between the full order and reduced order LQR design was performed and the results are provided in Figure 3.20. It was observed that the controller regulates the perturbed states to zero, for both full order and reduced order cases. A very close matching between the full order and reduced order states was observed, which manifests the effectiveness of the time scale method that almost the same performance was obtained with lower order controllers. The lower order controllers demand lesser computational efforts and could be implemented online for DLR technology that necessitates real-time monitoring and control.

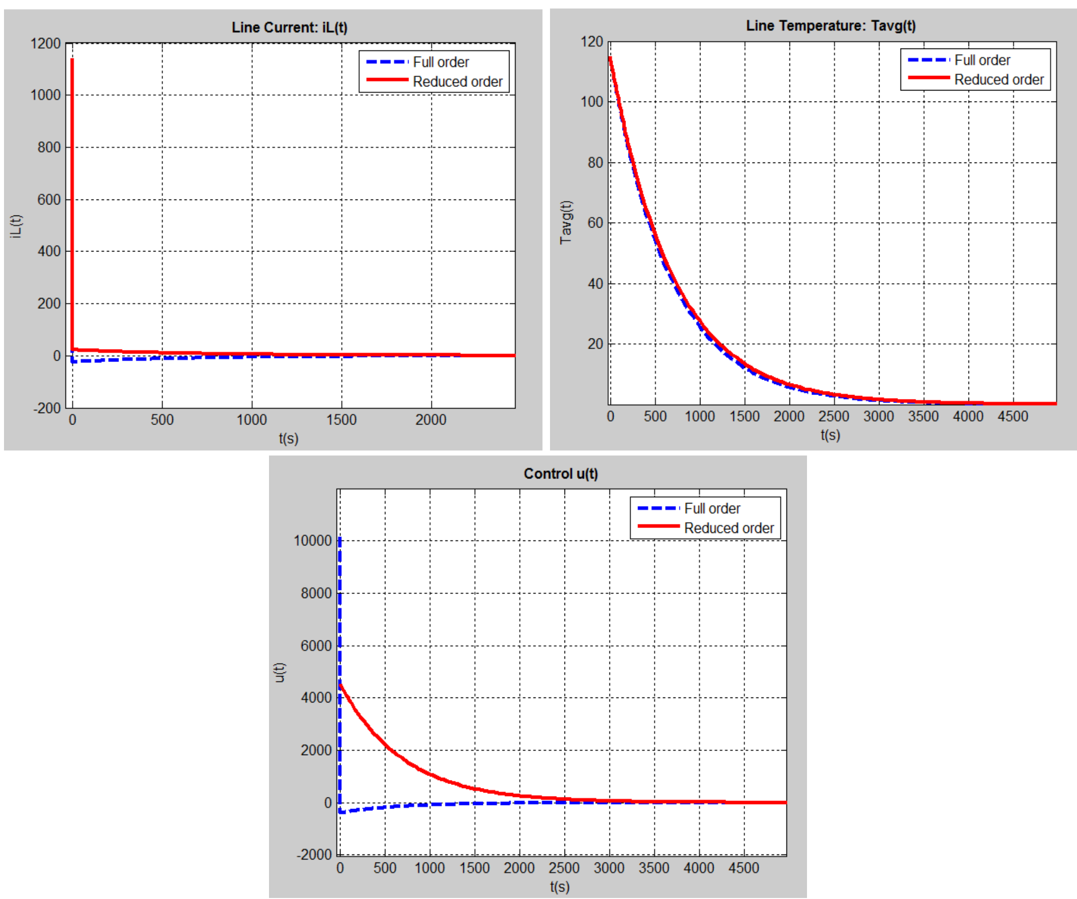


**Figure 3.20**: Comparison of full order and reduced order LQR control

When realistic models of power systems are considered, for example, a simple *1-machine* *infinite bus* system presented in [70] or a *3 machine, 9 bus* system in [71], the model dimensions were found to be 6 and 20 respectively (Figure 3.21).

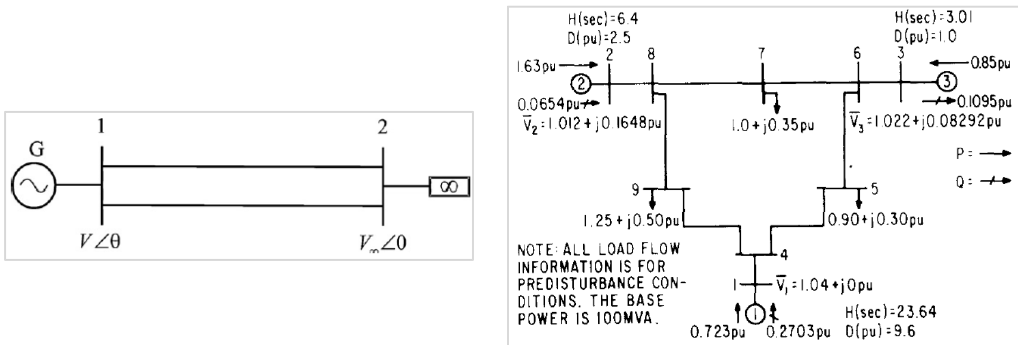


**Figure 3.21**: *1-machine, infinite bus* model [70] and *3 machine, 9 bus* model [71]

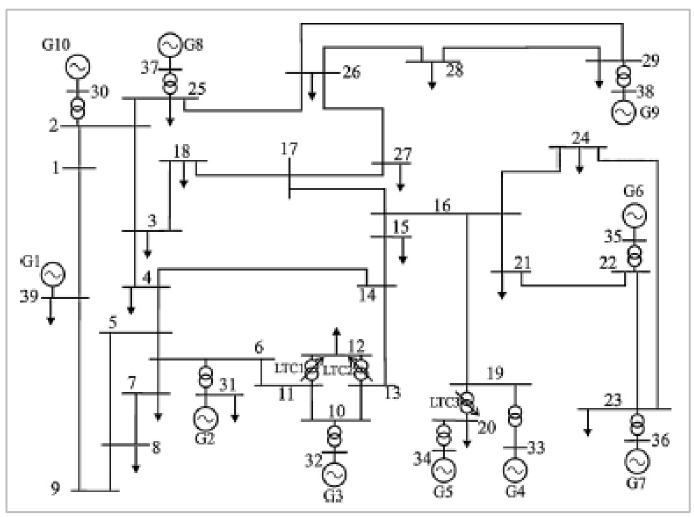


**Figure 3.22**:*10-Machine, 39-bus* New England power system model [70]

Designing any control law for a simple $6^{th}$ order model becomes very cumbersome, and for higher order models it may become unfeasible. A practical power system model such as the *10-Machine, 39-bus* model shown in Figure 3.22 would have to rely on powerful model order reduction techniques. Quasi-steady state approximations were used for analyzing the New England system in [70], i.e. the fast dynamics were neglected for model reduction. Time scale synthesis presented in this research achieves model order reduction without losing any system dynamics.

## 3.7 Resiliency of Time Scale Control

Resilience of controller operations is of paramount concern in today's highly interconnected and networked society. With smart grid technology, software control and decision making becomes deeply integrated into the electric power system. However, the increased dependence on cyber infrastructure makes it highly vulnerable to malicious cyber-attacks. Hence, to improve the security of the smart grid, control strategies have to be devised that are resilient to faults and malicious attacks.

In the event of a cyber-attack or failure of a controller, especially for critical and sensitive applications, implementing a *decentralized* control scheme will be highly beneficial. This would guarantee some control action to be still in place which would avoid critical failure of the entire system. In the event of controller outages, it could be possible to control the plant/system using any one of the multiple controllers designed using Time Scale Methods. Such a control system designed to tolerate failures of controllers, while retaining desired control system properties, is a "*reliable*" control system.

The decoupling of slow and fast dynamics in a transmission line facilitates implementation of a decentralized control scheme. Here, it is shown how a single controller (either slow or fast) by itself gives nearly original performance, thereby making the system more reliable or '*resilient*' in case of either controller malfunction.

The linear transmission line with the LQR feedback control was tested for two additional control scenarios, as listed below:

- Control signal = slow control + fast control (composite control) – Section 3.6.2

- Control signal = only fast control
- Control signal = only slow control

### 3.7.1 Simulation Results of Resiliency Test

A Simulink® model was built to test the three cases mentioned above, and is shown in Figure 3.23. In the case with only slow control, the fast control gain is made zero and vice versa.

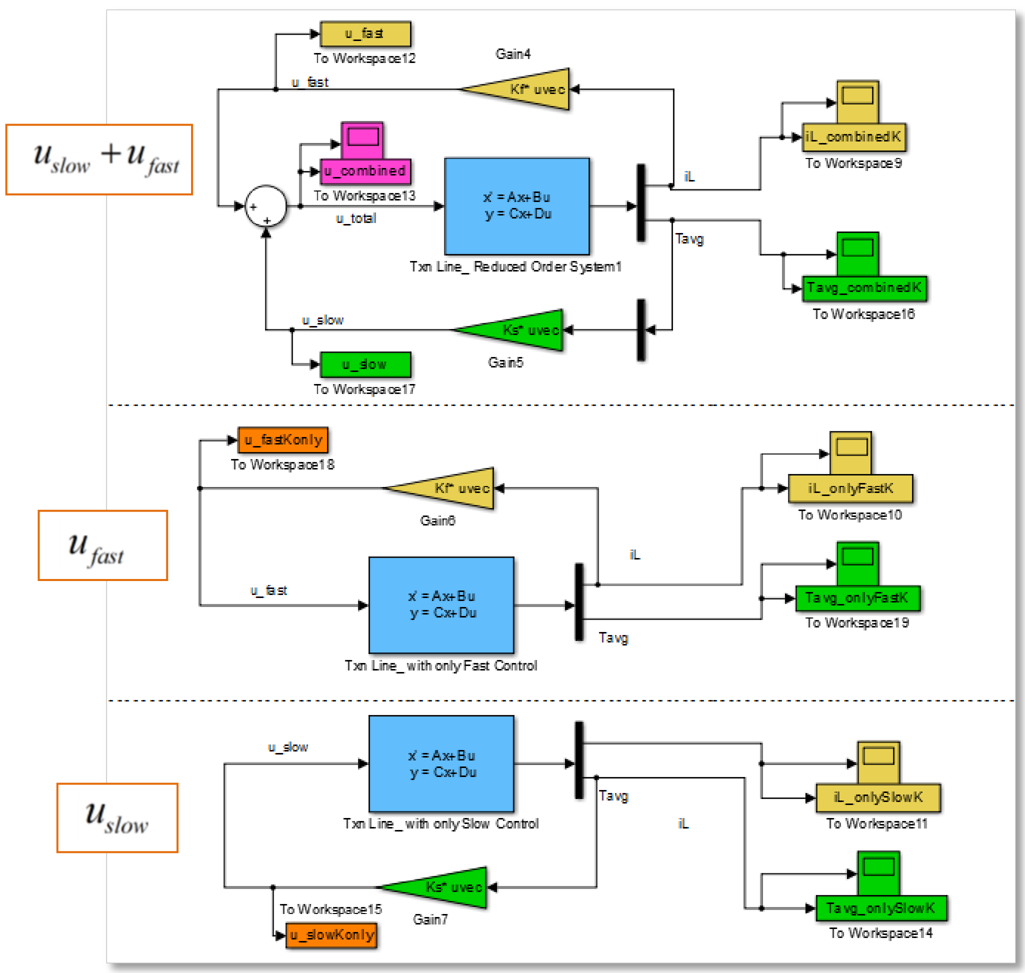


**Figure 3.23**: Simulink® model to test reliability of the reduced order LQR

The results of simulation for the three cases of control are given in Figure 3.24. The last plot displays the three cases of control inputs. The first two plots display the responses of line current and temperature to the three control inputs. It is observed that the states' response to the single control input (either slow or fast) is close to that of the composite control input. The case with only the slow control is very comparable to the case with the combined control. This shows that even in the absence/failure of one of the controllers, the remaining control effort does provide comparable control to the whole system. This reiterates the strength of the time-scale control design approach (multiple controllers), which provides resiliency to the systems as compared to a centralized control design.

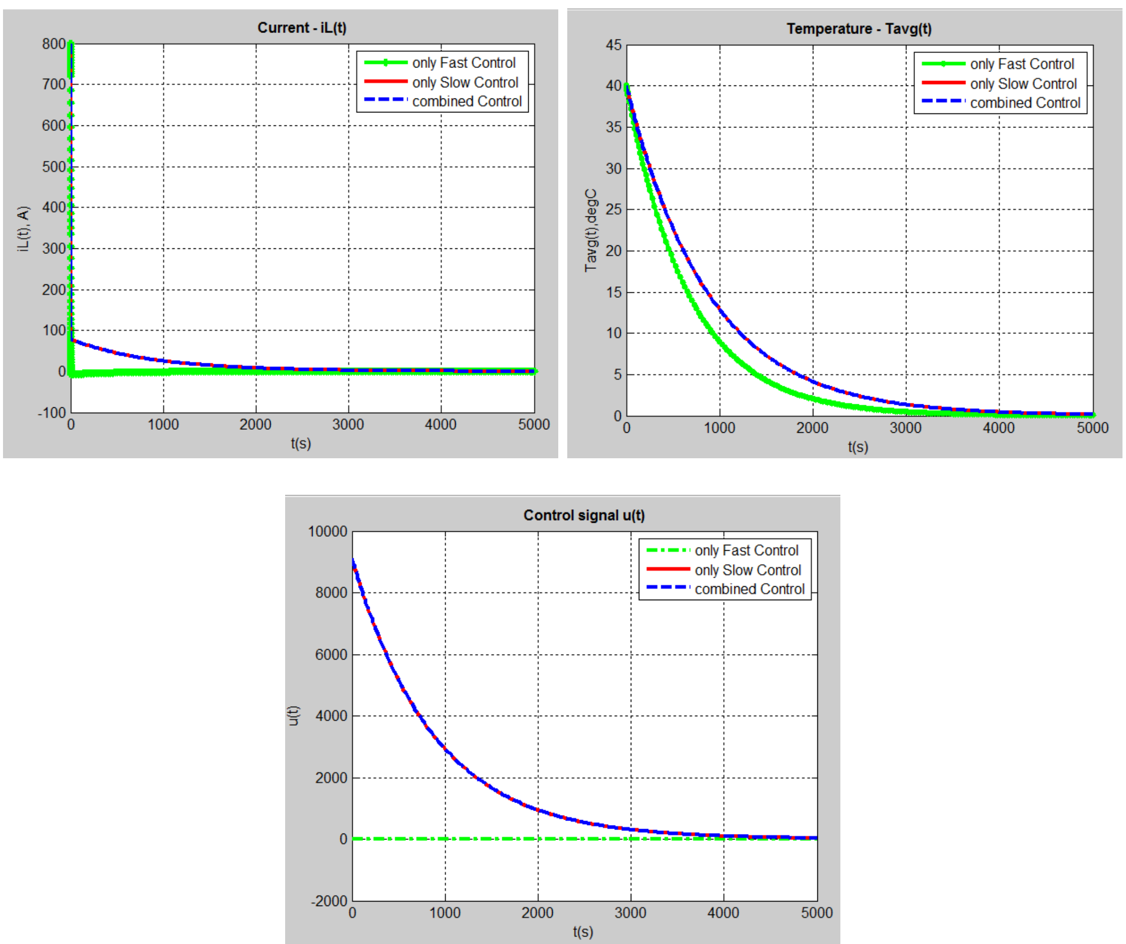


**Figure 3.24**: Results of the reliability test of time scale control design

### 3.8 Transmission Line Modeling and Potential DLR Applications

Researchers at the Idaho National Laboratory (INL) are working towards developing a Java-based software package called General Line Ampacity State Solver (GLASS), which calculates real-time ampacity and thermal conductor limits [73]. A schematic representation of GLASS is provided in Figure 3.25. The real-time ampacity and conductor thermal limits are calculated based on current weather conditions at sparsely located weather stations. This is done by combining Geographic Information System (GIS) data with historic weather information and pre-computed Computational Fluid Dynamics (CFD) models. INL collaborates with WindSim, a wind energy simulation software company, for CFD modeling and verification. INL also partners with regional utilities including Idaho Power for performing transmission line data verification [73].

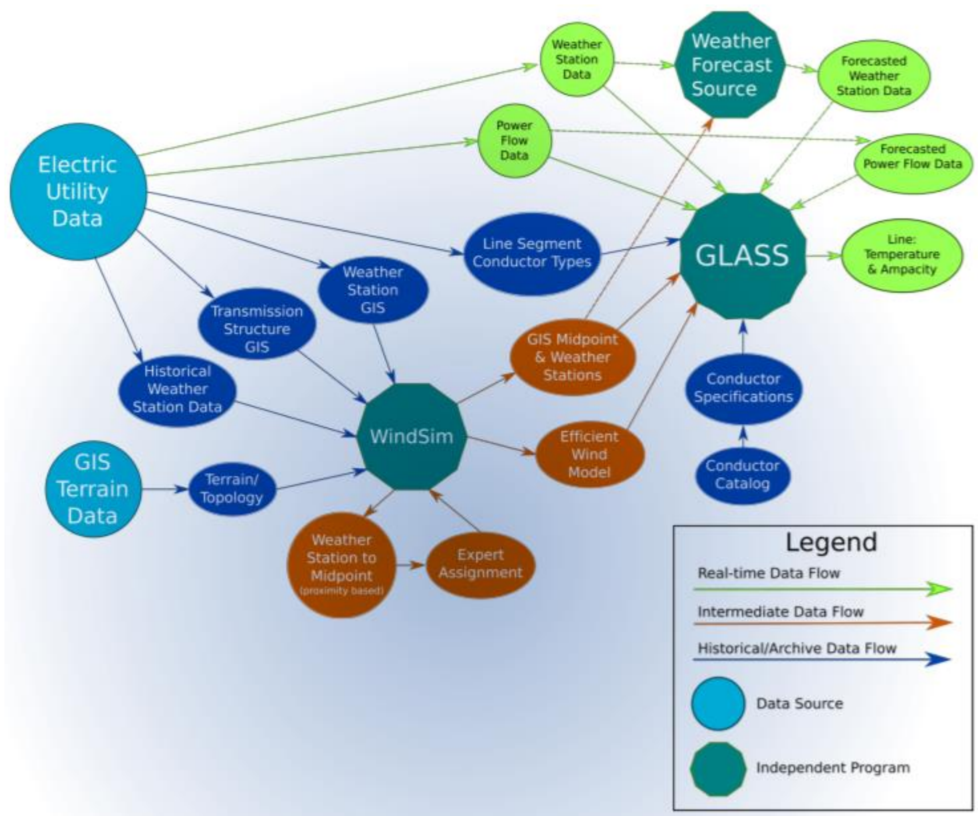


**Figure 3.25**: Real-time data flow and forecast calculations of the GLASS software [73]

The processed real-time weather information is fed to the GLASS software which uses algorithms from the IEEE 738 Standard [3] to yield real-time ampacity and thermal conductor limits. However, the calculations are based on steady-state equations which do not account for the dynamic behavior of the transmission line [8].

The nonlinear model presented in this research accounts for both the electrical and thermal dynamics in transmission lines, thus depicting more realistic behaviors for dynamic line ratings. This implies that in the event of a step change in current due to a perturbation, the temperature response to this step change will be observed from the simulations. This will help the operator/utility determine the duration for which the new current levels can be safely allowed through the transmission line, before the instantaneous temperature attain unsafe limits [8]. The availability of such valuable information would assist the operator or a decision making controller in an Energy Management System (EMS) or Supervisory Control And Data Acquisition (SCADA) systems, and would help establish safe line ampacity levels based on real-time conductor temperature.

Furthermore, the lower order, slow and fast optimal controllers designed for mitigating perturbations in a transmission line, facilitate on-line/ real-time control implementations, and could be embedded in the utility’s Energy Management System (EMS).

### 3.9 SPaTS Methods in Renewable Energy

Innovation and technological developments in the renewable energy sector are forging pathways which will establish them as a major stakeholder in electricity generation. Wind energy has grown significantly over the last few decades and continues to lead in electricity generation among the other renewable sources. Data released in March, 2017 [74] revealed that for the first time in the U. S., wind and solar energy accounted for 10 percent of all electricity generation, with wind contributing 8 percent and solar at 2 percent (Figure 3.26).

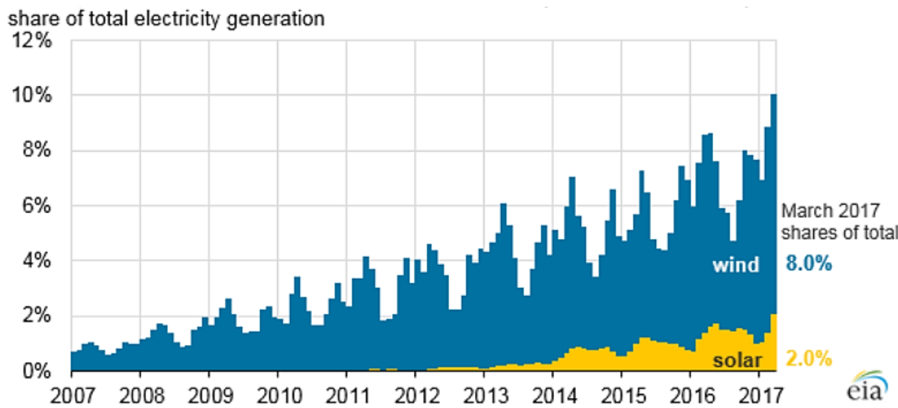


**Figure 3.26**: Monthly net electricity generation from selected fuels (*Source:* EIA) [74]

Great advances in control strategies have been significant in harnessing the maximum power of the wind, a highly intermittent energy source, at safe operating conditions. Due to its erratic nature, mechanical systems of the wind turbine are subjected to fatigues and perturbations from the wind, for example, a gust of wind. Optimal control techniques have been researched greatly that maximizes the power harnessed from the wind while minimizing the perturbations in the system. Such optimal control strategies are often associated with high model dimensions and might become unfeasible for real-time implementations due to the complexity of numerical calculations involved.

SPaTS methods are well equipped to address such problems. The applications of SPaTS methods in Wind Energy Conversion Systems (WECS) were investigated in [38, 55, 75].

A brief overview of these methods in WECS is provided in the following sections as an illustration of the extent and flexibility of these unique methods in renewable wind energy systems. In particular, a singular perturbation method developed by A. B. Vasileva [76, 52] is applied towards solving WECS as a nonlinear initial value problem (IVP), and synthesis of time scale, optimal control laws for deterministic and stochastic WECS models.

### 3.9.1 WECS - Dynamic Modeling and Time Scales

WECS could be summarized as a structure that transforms the kinetic energy of the wind into electrical energy. A wind turbine rotor serves as the transducer that harvests the wind energy, and it drives the generator, which outputs electric power. The research involves the study of a Horizontal Axis Wind Turbine (HAWT). Its dynamic model accounts for the turbine rotor dynamics and the drive train and generator shaft dynamics (Figure 3.27).

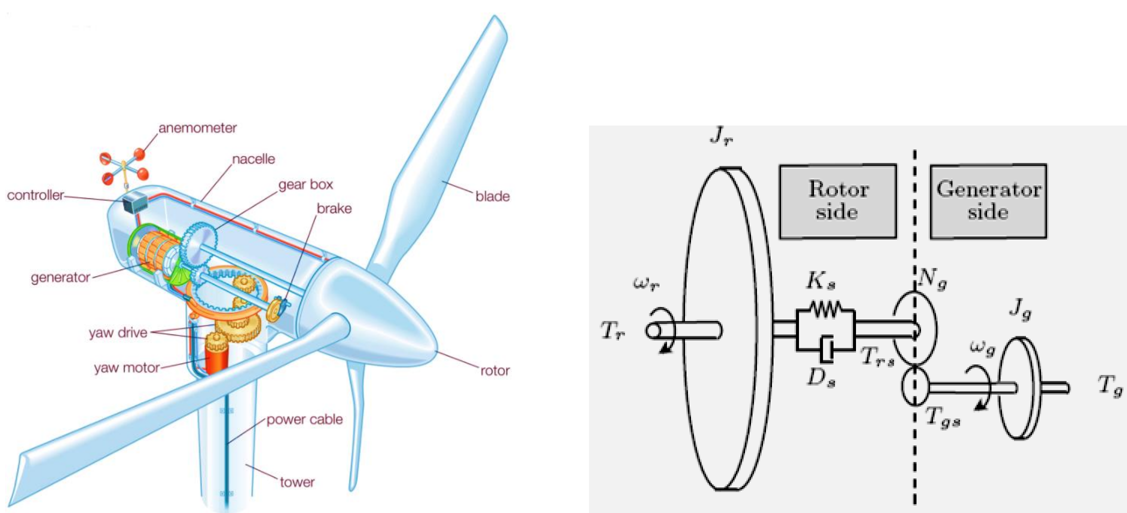


**Figure 3.27**: Structure of HAWT (left); Schematic of wind turbine rotor and drive train dynamics (right)

A third order, nonlinear state-space model is used to describe the dynamics of the WECS.

The eigenvalues of the linearized model are analyzed, and the clearly separated groups of eigenvalues indicate the slow - fast behavior of the wind energy system. A scaling operation and a 'change of time scale' procedures identified the singular perturbation (SP) parameter '$\varepsilon$' in the WECS to be a ratio of the mechanical time constants of the generator and turbine rotor (Figure 3.28). Generally, if one infers time scale nature in a wind energy system, the '*slow*' mode would be by virtue of the mechanical systems and a '*fast*' mode by virtue of electrical systems. But this research highlights the fact that time scales arise within mechanical systems, due to the large differences in inertia of the turbine and generator. The time scale behavior is due to the slow turbine rotor dynamics and the fast drive train-generator dynamics.

$$\frac{dx}{dt_r} = \frac{1}{2}\left( (8.054e-5)\frac{P_r(x(t_r), v(t_r))}{x} - 100\pi K_{s,pu} z_1 - D_{s,pu}(x - \frac{z_2}{N_g}) \right),$$

$$\varepsilon \frac{dz_1}{dt_r} = 0.4874\left( x - \frac{z_2}{N_g} \right),$$

$$\varepsilon \frac{dz_2}{dt_r} = (2.827e3)\frac{K_{s,pu} z_1}{N_g} + 9\frac{D_{s,pu}}{N_g}(x - \frac{z_2}{N_g}) - (7.2485e-4)u,$$

$$\text{where } \varepsilon = \frac{2H_g}{H_r} = 0.1344,$$

$$\text{and } \begin{bmatrix} x & z_1 & z_2 & u \end{bmatrix}^T = \begin{bmatrix} w_r & \theta_{diff} & w_g & T_g \end{bmatrix}^T.$$

| **Inputs** $T_g = 2132$N-m | **Eigenvalues** |
|---|---|
| $v$ =14 m/s | -7.0597 +36.8919i<br>-7.0597 -36.8919i<br>-0.1619 |
| $v$ =16 m/s | -7.0604 +36.8918i<br>-7.0604 -36.8918i<br>-0.1832 |
| $v$ =18 m/s | -7.0609 +36.8917i<br>-7.0609 -36.8917i<br>-0.1983 |
| $v$ =20 m/s | -7.0613 +36.8916i<br>-7.0613 -36.8916i<br>-0.2106 |
| $v$ =22 m/s | -7.0617 +36.8915i<br>-7.0617 -36.8915i<br>-0.2218 |

**Figure 3.28**: WECS - Dynamic model in SP form (left) and eigenvalues (right)

### 3.9.2 Initial Value Problem (IVP) of WECS

The nonlinear model of WECS is solved as an IVP using Vasileva's singular perturbation method, which involves a combination of asymptotic expansions, power series and Taylor series [76]. The total series solution of the system of nonlinear ODEs in the WECS model is given as, *Total Solution = Outer series + Inner Series – Intermediate Series,*

up to a 1st order approximation (Figure 3.29). The approximate total series solution provides in most cases, *analytical* solutions of nonlinear IVPs up to a zeroth order or first order approximation. From these analytical expressions, the behavior of the system can be well understood and suitable predictions of the system can be deduced. Also, these approximations accurately capture the dynamics of the system without sacrificing any of the system's original boundary conditions. This is brought forth by incorporating '$\varepsilon$' in the series solutions of the WECS model, and is not neglected as observed in the conventional approach to singularly perturbed systems. The response of one of the states of the WECS model, turbine rotor speed, is illustrated in Figure 3.29, where the zeroth order approximation alone fails to capture the dynamics in the boundary layer ($t <$ 0.012s), but when combined with its 1st order approximation, provides a very good approximation of the actual solution.

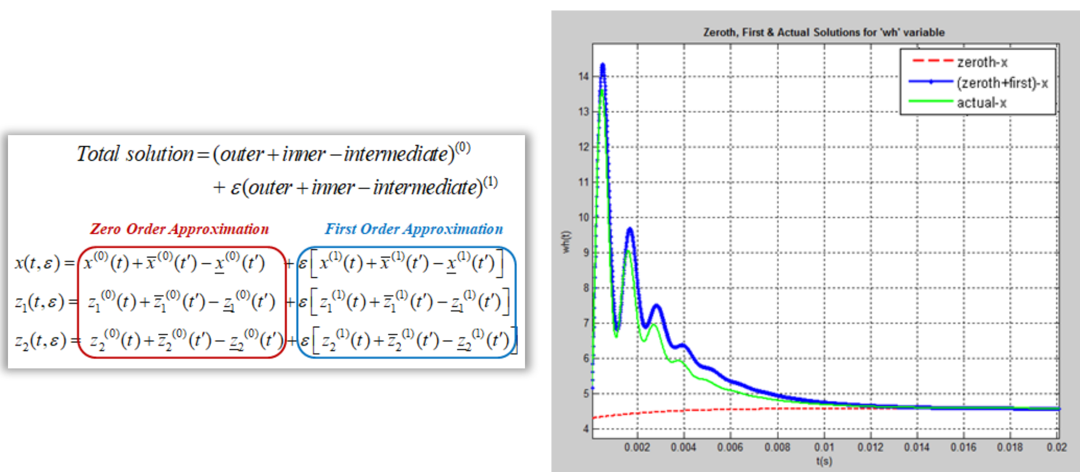


**Figure 3.29**: IVP of WECS using Vasileva's singular perturbation method

### 3.9.3 Deterministic and Stochastic Time Scale Optimal Control

Time scale synthesis of optimal controllers is performed for both deterministic and stochastic WECS models, with the objective of minimizing perturbations in a wind energy system. For the deterministic WECS model, system perturbations are regulated through a composite control of the slow and fast LQR controllers.

For the stochastic WECS model (which accommodates practical scenarios such as unavailability of states for measurement, and corruption of available states with noise), the time scale LQG design involves a non-singular transformation [53] that decomposes the Kalman filter into *slow* and *fast* Kalman filters and the LQR gain into *slow* and *fast* gains. The slow and fast Kalman state estimates are fed to the respective LQR gains for achieving the desired state regulation. Time scale synthesis and simulation results of LQR and LQG optimal control are provided in Figure 3.30 and Figure 3.31, respectively.

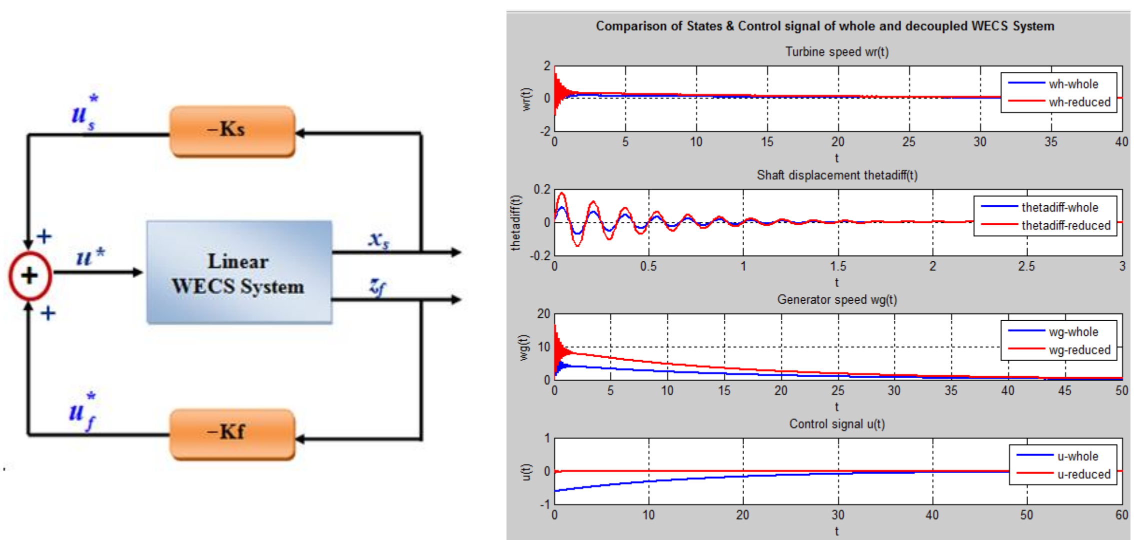


**Figure 3.30:** Time scale synthesis of LQR for WECS (left); Simulation results (right)

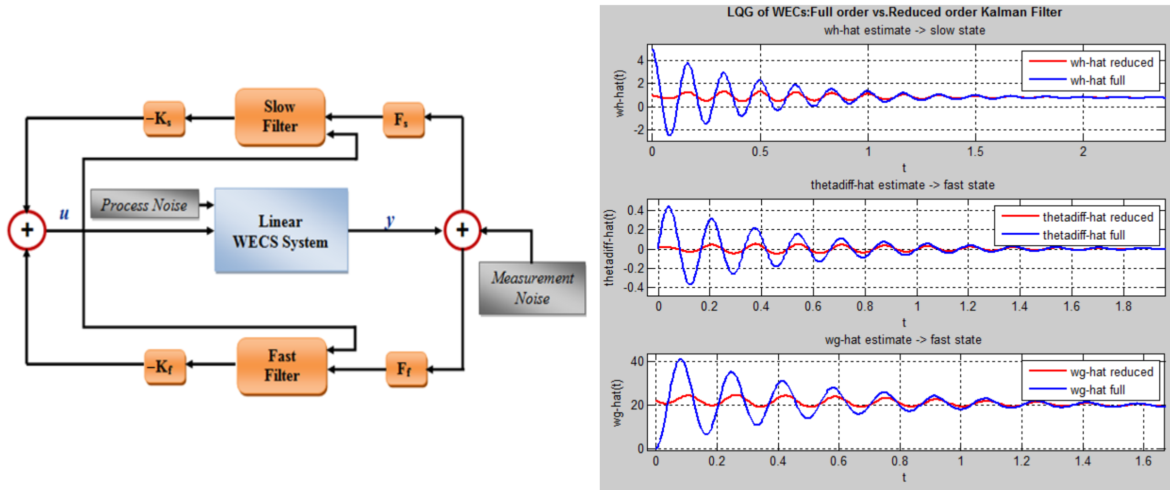


**Figure 3.31:** Time scale synthesis of LQG control for WECS (left); Simulation results (right)

The simulation results indicate that the performance of the reduced-order model matches the performance of the full order model very closely. Also, a careful observation of the LQG results reveals that the amplitudes of oscillation of the state responses have been reduced in the time scale design. These results hold far reaching implications in that, SPaTS methods could assist with control strategies for WECS that are computationally efficient and suitable for real time applications.

## 3.10 Conclusion

The applications of SPaTS methods for the design of control strategies in Electrical Engineering, namely Overhead Power Transmission Lines and Wind Energy Conversion Systems were investigated. The major focus of the chapter was on Overhead Power Transmission Lines where time scale analysis and synthesis were performed. A second order, nonlinear time domain model was developed that captures the electrical and thermal dynamics of transmission lines. This model renders instantaneous values of line current and line temperature, which are very useful information for Dynamic Line Rating of transmission lines. The availability of this information to an operator or a decision making controller in Energy Management System (EMS) or SCADA systems, would help establish the safe line ampacity levels based on real-time conductor temperature.

Time scale techniques were presented which enabled computationally efficient control designs. The simulation results confirm that comparable control action can be achieved with independent, lower-order, slow and fast controllers. In detailed power system models, such as the one in [70], where various components of a power chain are modeled (typically comprising of generators, transmission lines and power electronic interfaces), the combined model order could be very high, and evaluating control designs or their online implementations, may become unfeasible. With the time scale approach, standard control laws like optimal control, state feedback control, model predictive control and robust control can still be realized for higher order systems.

Finally, it was demonstrated that the presence of multiple controllers in place of one central controller guarantees comparable control action during failure of one of the controllers in the system, thereby ensuring reliability of the transmission line system. Research work on WECS reinstated that SPaTS methods were effective in gaining better insights into the system behaviour by solving WECS as a singularly perturbed IVP, and for simplifying optimal control designs. Realistic models of WECS (accounting for aerodynamics, drive train dynamics, electrical generator dynamics, power interface dynamics, and load dynamics) would be able to benefit from SPaTS methods in achieving feasible real-time control solutions.

Future work would investigate modeling transmission lines with distributed parameter models (medium and long length) for any unaccounted line current dynamics and enhance the computational accuracy of line ampacity levels.

# Chapter 4

# Time Scale Analysis and Synthesis in Life Sciences

This chapter introduces the biological aspects of a Human Immunodeficiency Virus (HIV) infection, followed by mathematical modeling of the viral dynamics. A third order, nonlinear, state space model is adopted from literature to analyze and study the nature of an HIV infection. The inherent time scale characteristics of the HIV dynamics are investigated and identified through linearization and non-dimensionalization procedures. An optimal treatment strategy for the HIV infection is developed using time scale separation methods, where a full order linear HIV model is decoupled into independent, lower order, slow and fast subsystems. The efficacy of this control approach is compared to that of a general, full order optimal control design. A preliminary study of measles, another serious infectious disease that primarily affects children, was conducted during the initial research period and findings of this brief study are presented at the end of the chapter.

## 4.1 The Biology of HIV Infection

The biological aspects of an HIV infection are imperative in the mathematical modeling and control of the disease. The immune system response and its interactions with HIV form the basis of the dynamic model. Biological events that mark the HIV’s life cycle are important in identifying and pursuing potential control strategies. Hence, an overview of the high level processes in a typical immune system response and the basics of an HIV infection are provided in the following sections.

### 4.1.1 Human Immune System

The immune system is a remarkable, complex network of cells, tissues and organs that work together to defend the body against foreign particles (bacteria, viruses and fungi) that can cause infections. When an antigen or a foreign particle is introduced into the human body, the immune system responds immediately in an attempt to discard the object from the body. This immune response is characterized by a cellular immune response and a humoral immune response [77].

Macrophages, the cells that scavenge, ingest, and process foreign particles, encounter the antigen first and present the antigen information to the $CD4^+$ T cells. The $CD4^+$ T cells are commonly referred to as 'helper T cells' and serve as the command center for the immune system. '*CD4*' denotes a protein on the surface of the T cell, and 'T' refers to thymus, the organ in which these cells mature after migration from the bone marrow where they are created. On an average, there are 1000 $CD4^+$ cells per $mm^3$ of blood. In the event of an attack, macrophages, through chemical alarm signals, activate the helper T cells, which in turn proliferate to elicit both cellular and humoral responses. In the *cellular immune response*, the helper T cells activate a second type of T cells, called the $CD8^+$ T cells. These cells are referred to as killer T cells that seek and destroy cells infected by pathogens. In the *humoral immune response*, commonly known as the antibody response, the helper T cells signal a third set of cells, called B cells. B cells produce chemical weapons called antibodies that are specifically designed to attack and destroy antigens in the body [77]. Figure 4.1 shows the schematic of an immune response process.

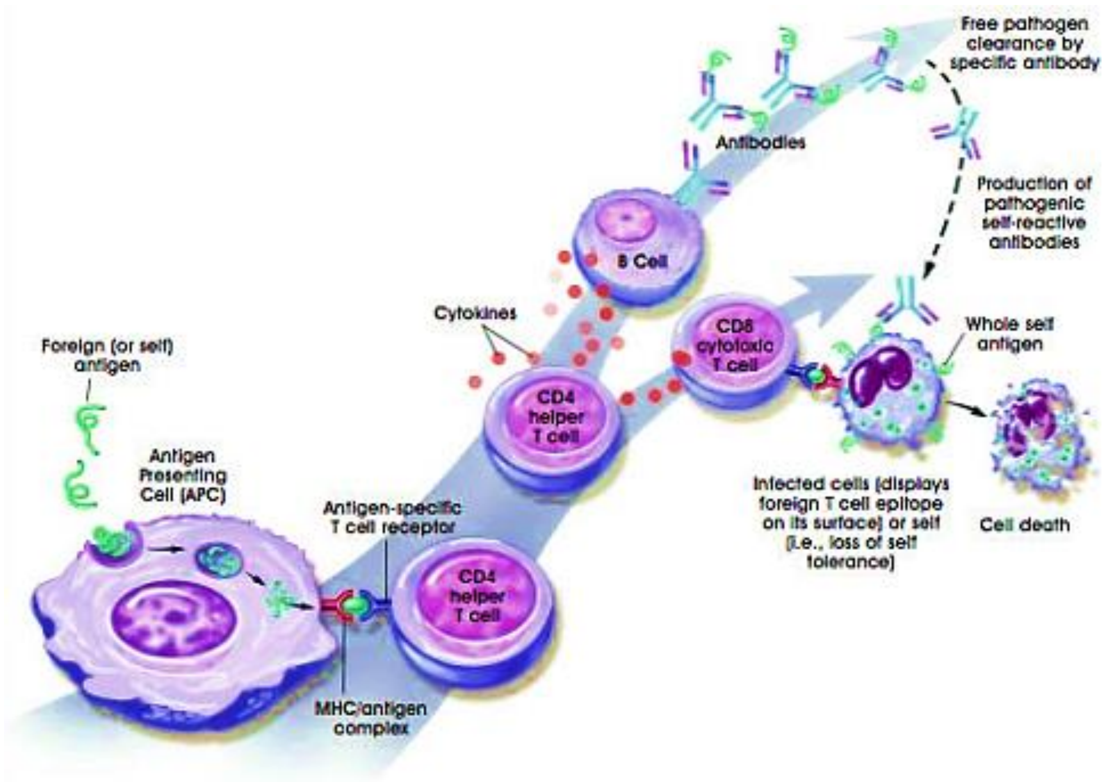


**Figure 4.1**: Stages of a typical human immune response [78]

Once the immune response is successful, certain cells of each type retain knowledge of the attack. These cells are referred to as memory cells. If the same or a similar pathogen is introduced into the body again, a much quicker and more aggressive response is enforced, and the antigen is eradicated more accurately and at a much faster rate. If the individual becomes infected with a more aggressive relative, then the response is instantaneous and potent, and the pathogen does not take hold [77].

### 4.1.2 HIV Infection and Timeline

HIV is a retrovirus, belonging to the family *Retroviridae*, which carries its genetic information in Ribonucleic Acid or RNA, unlike most organisms which carry their genetic material in Deoxyribonucleic Acids (DNA). Like most viruses, HIV does not have the ability to reproduce independently, and therefore relies on a host to aid reproduction. Figure 4.2 depicts the structure of an HIV particle.

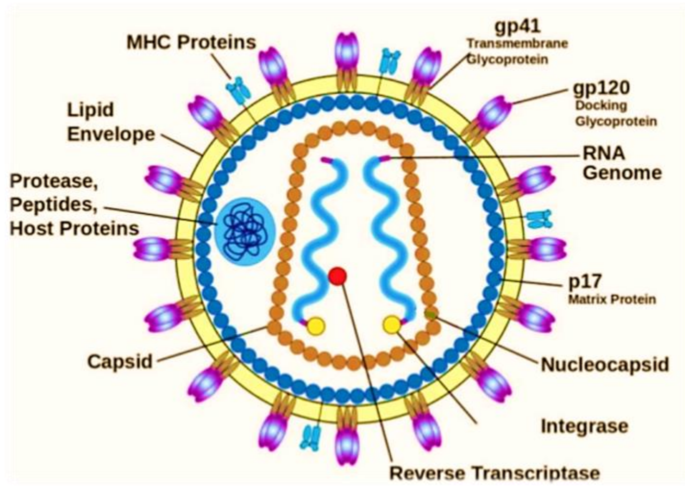


**Figure 4.2**: Structure of a Human Immunodeficiency Virus [79]

There are two major types of the human immunodeficiency virus, *HIV-1* and *HIV-2*. HIV-1, which was discovered first, is the most widespread type worldwide. HIV-2 is relatively uncommon and mostly concentrated in West Africa. It is 55% genetically different from HIV-1 [80]. Both types can lead to AIDS, but the HIV-2 takes a slower course in progressing to AIDS than HIV-1. In this work, mention of HIV refers to HIV-1.

When HIV infects the body, it targets the $CD4^+$ T cells, the main regulators of the immune system – the primary cause of HIV's devastating impact. A protein (GP120) on the surface of the virus binds to the *CD4* protein on the T cell surface and the contents of the HIV is injected into the host T cell. HIV being a retrovirus first transcribes its genetic RNA into viral DNA using its enzyme, *reverse transcriptase*. The viral DNA is then integrated into the host cell DNA using enzyme *integrase*. The host's normal transcription process transcribes viral DNA into multiple copies of new HIV RNA. Some of this RNA becomes the genome of a new virus, while the host cell uses other copies of the RNA to make new HIV proteins. The newly formed viral RNA and HIV proteins move to the surface of the cell, where a new, immature (noninfectious) HIV is formed. Finally, the immature virus pushes itself out of the host cell (budding), and releases an enzyme *protease* that reassembles the new HIV proteins to create a mature infectious virus. The budding can either take place slowly, sparing the host cell or rapidly, bursting and killing the host cell [77].

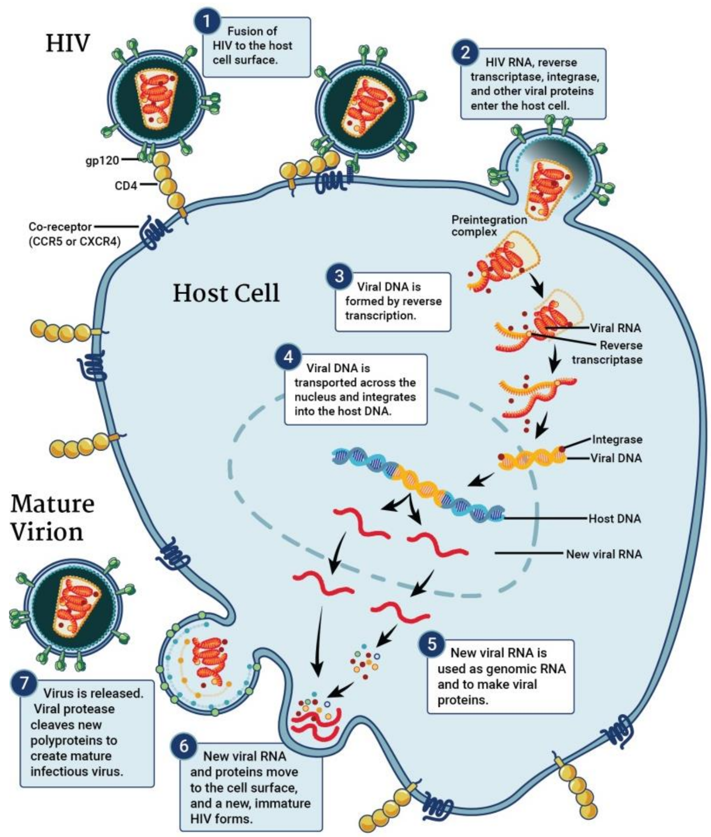


**Figure 4.3**: HIV replication cycle [81]

**Timeline of Disease Progression**

There are three main stages in the progression of an HIV infection [82]. *Acute HIV infection* is the earliest stage where HIV multiplies rapidly and spreads throughout the body. The virus attacks and destroys the infection-fighting *CD4* cells of the immune system. The second stage is the *chronic HIV infection*, or asymptomatic phase or clinical latency. During this phase, HIV continues to multiply in the body but at very low levels. The final and most severe stage of HIV infection is *AIDS* during which HIV has severely damaged the immune system and the body is vulnerable to opportunistic infections. People with HIV are diagnosed with AIDS if they have a *CD4* count less than 200 cells/mm$^3$ or if they have certain opportunistic infections. Without treatment, people with AIDS typically survive about 3 years [82]. The timeline of the HIV infection is provided in Figure 4.4.

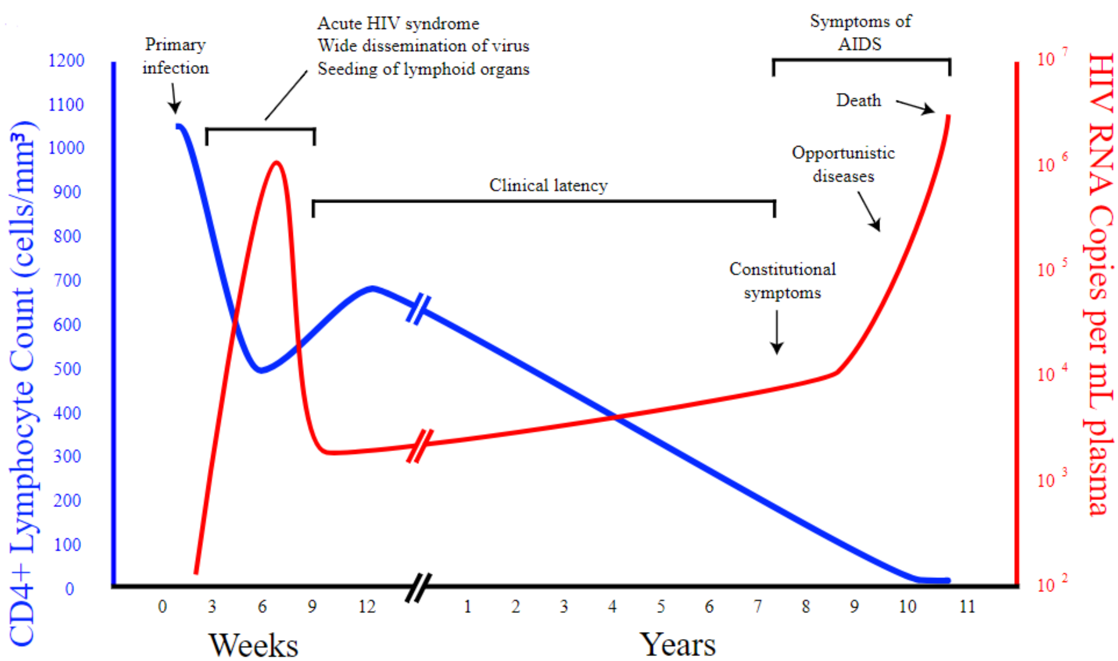


**Figure 4.4**: Time course of a typical HIV infection [83]

### 4.1.3 HIV Treatment

To date, ART cannot cure HIV, but HIV medicines help infected individuals live longer and healthier lives, and also reduce the risk of HIV transmission [49]. Currently, treatment of an HIV infection is through a combination of different class of antiretroviral drugs that are used to slow down the rate at which HIV multiplies in the body. An overview of currently adopted antiretroviral drugs and their points of inhibition in HIV are depicted in Figure 4.5.

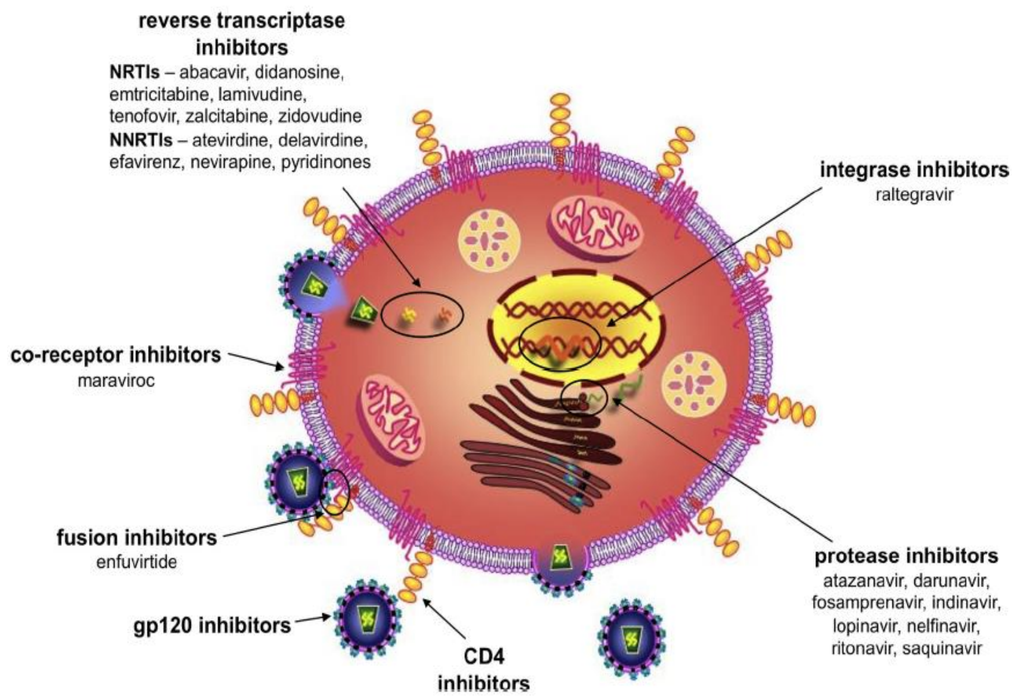


**Figure 4.5**: Inhibition of HIV-1 replication at different steps in the viral life cycle [84]

The combination of medicines is called an HIV regimen and a person's initial HIV regimen generally includes three HIV medicines from at least two different drug classes. Treatment with a single drug failed as the HIV replicated and mutated very rapidly and drug resistance was developed in the early days of drug intake. The six classes of antiretroviral drugs that are currently used in ART are [49],

- Nucleoside Reverse Transcriptase Inhibitors (NRTI)
  - block reverse transcriptase, an enzyme that facilitates transcription of viral RNA to viral DNA. E.g. *abacavir*, *zidovudine – azidothymidine or AZT* (1$^{st}$ drug to treat HIV in 1987)

- Non-Nucleoside Reverse Transcriptase Inhibitors (NNRTI)
  - bind to and alter reverse transcriptase; E.g. *efavirenz, etravirine*
- Fusion Inhibitors
  - block HIV-1 from entering the *CD4* cells of the immune system; E.g. *enfuvirtide*
- CCR5 Antagonists or Entry Inhibitors
  - block CCR5, a protein on the *CD4* cells that a certain type of HIV-1 needs to enter the cell; E.g. *maraviroc*
- Protease Inhibitors (PI)
  - block HIV-1 protease, an enzyme HIV-1 needs to process the HIV proteins to create a mature infectious virus; E.g. a*tazanavir, ritonavir*
- Integrase Strand Transfer Inhibitors (INSTI)
  - block HIV-1 integrase, an enzyme HIV-1 needs to integrate its DNA into the host cell DNA; E.g. *dolutegravir, elvitegravir*

New antiretroviral drug classes like entry inhibitors and integrase inhibitors that were recently approved for clinical use will increase the number of possible drug combinations and provide more options for effective treatment [84]. However, with each new combination, the prospect of adverse side effects that could affect adherence to the therapy remains an important concern.

## 4.2 Modeling an HIV Infection

Mathematical modeling combined with experimental and clinical data analysis has offered critical insights towards the understanding of viral and immune system dynamics, and ART. To date there are a multitude of dynamic models in literature that describe an

HIV infection. Different aspects of the disease are explained in each model, but none of the models exhibit all that is observed clinically. This is partly due to the fact that much about this disease's mechanics is still unknown [77].

The basic and simplest models of viral infection account for only the key players of an HIV infection, namely the uninfected $CD4^+$ T cells, infected $CD4^+$ T cells and free virions. These models come under the class of '*target-cell limited*' models meaning that the HIV-1 infection is limited by the availability of target T cells, and also lacks an explicit representation of the immune response. Despite this deficit, the model fits viral kinetic data obtained both during natural infection and while patients are on therapy [85]. Thus purely target cell limited models remain a popular form of HIV infection in literature and have been frequently used in the pharmacodynamic studies of ART [11, 25, 26, 77, 86, 87, 88]. Modification to this model was made by authors in [89], where they supplemented this basic model with dynamics of latently infected and actively infected T cells.

Another set of HIV models found in literature fall under the group of '*immune limited*' models, where the HIV infection is limited by specific anti-HIV cellular immune response i.e. the virus is a prey that is controlled by $CD8^+$ lymphocytes, an immune response predator. While many models have included $CD8^+$ responses [19, 90, 91] they tend to lack comparisons with experimental data leaving the field without good estimates for the parameters that govern the $CD8^+$ cells' effects [85].

In this research, a target-cell limited model, which captures the dynamics of uninfected $CD4^+$ T cells, infected $CD4^+$T cells and free virions, is used for analysis and design.

### 4.2.1 Nonlinear HIV Model

A third order, nonlinear, state space model of an HIV infection is presented. The control variables (denoting antiretroviral drugs used in the treatment) are not included in this model, and will be dealt in Section 4.4. The dynamic equations [25] are,

$$\begin{aligned}
\frac{dx_1(t)}{dt} &= s - Dx_1(t) - \beta x_1(t)x_3(t), \\
\frac{dx_2(t)}{dt} &= \beta x_1(t)x_3(t) - \mu_2 x_2(t), \\
\frac{dx_3(t)}{dt} &= kx_2(t) - \mu_1 x_3(t),
\end{aligned} \tag{4.1}$$

where $x_1(t)$ denotes the concentration of uninfected $CD4^+$ T-cells; $x_2(t)$ denotes the concentration of infected $CD4^+$ T-cells, and $x_3(t)$ represents free virus particles. It is assumed that the body produces healthy and uninfected $CD4^+$ T cells from the thymus at a constant rate *s*. The T cells are also assumed to have a finite life span and die with the rate *D* per cell. The term $\beta x_1(t)x_3(t)$ models the rate at which free virus infects healthy T cells. When a T cell becomes infected, it becomes an infected T cell, thus the term $\beta x_1(t)x_3(t)$ is subtracted from the 1st equation and added to the 2nd equation. Infected T cells ( $x_2(t)$ ) have a natural death rate, $\mu_2$ and can be expected to die sooner due to the additional stress put on the cell by the virus. The third equation models the population of free virus. It is assumed that when an infected $CD4^+$ T cell becomes stimulated through exposure to antigen, replication of virus is initiated, and viruses are produced with a rate *k* before the host cell dies. The term $\mu_1 x_3(t)$ records the loss of virions through death and/or immune clearance. The numerical values of the constant parameters in the model are listed in Table 4.1.

**Table 4.1:** HIV Model Parameters [25]

| Parameter | Description | Numerical Value |
|---|---|---|
| $s$ | Source of healthy T- cells | 10 per mm$^3$per day |
| $D$ | Death rate of healthy T- cells | 0.02 per day |
| $\mu_1$ | Death rate of viruses | 0.24 per day |
| $\mu_2$ | Death rate of infected T- cells | 2.4 per day |
| $\beta$ | Rate at which T-cells become infected by free viruses | $2.4\times10^{-5}$ per (mm$^3$ × day) |
| $k$ | Rate of virions produced per infected T-cell | 100 per cell |

## 4.3 Analysis of the Nonlinear HIV Model

### 4.3.1 Equilibrium Points

The equilibrium points of the HIV model are determined by setting the derivatives of (4.1) to zero and solving the algebraic equations in (4.2) as,

$$\begin{aligned} & s - Dx_1^*(t) - \beta x_1^*(t)x_3^*(t) = 0, \\ & \beta x_1^*(t)x_3^*(t) - \mu_2 x_2^*(t) = 0, \\ & kx_2^*(t) - \mu_1 x_3^*(t) = 0. \end{aligned} \tag{4.2}$$

The equilibrium points are calculated for an '*infection free*' and '*infection bound*' scenarios, and are found to be,

$$\begin{aligned} & \left(x_{1a}^*, x_{2a}^*, x_{3a}^*\right) = \left(\frac{s}{D}, 0, 0\right) = \left(500, 0, 0\right) \text{ and} \\ & \left(x_{1b}^*, x_{2b}^*, x_{3b}^*\right) = \left(\frac{\mu_1\mu_2}{k\beta}, \frac{s}{\mu_2} - \frac{D\mu_1}{\beta}, \frac{sk}{\mu_1\mu_2} - \frac{D}{\beta}\right) = \left(240, 2.167, 902.78\right), \end{aligned} \tag{4.3}$$

respectively. For an *infection free* equilibrium or the uninfected steady state, the virus is not present and the body maintains a steady count of healthy T cells at 500 per mm$^3$. In the case of an infection, the healthy T cell count stabilizes at 240 cells per mm$^3$, a value slightly lower than the threshold for AIDS, and a viral count of about 902 virions per mm$^3$ of blood. During this period, the body is in an *endemically infected state*, where both virus and infected T cells are present [92], but with a lower T cell count than that of the virus. Even though the body is constantly producing T cells, there seems to be a balance between the body's efforts and the rate of infection by the virus.

### 4.3.2 State Response Plots

To gain insights into its dynamic behavior, the nonlinear HIV model (4.1) is simulated with the numerical parameters in Table 4.1. The initial conditions for the state variables are set as in Table 4.2. The simulations were performed in MATLAB® and Simulink® software.

**Table 4.2:** Initial conditions for nonlinear HIV model simulation

| Parameter | Description | Numerical Value |
|---|---|---|
| $x_1(0)$ | Healthy T- cell population | 1000 per mm$^3$ |
| $x_2(0)$ | Infected T- cell population | 0 per mm$^3$ |
| $x_3(0)$ | Free HIV population | 1 per mm$^3$ |

The responses of the states to the initial conditions are provided in Figure 4.6. From the plots it is observed that by introducing just one virus particle per mm$^3$, as set in the initial conditions, $\boldsymbol{x}(0)$=[1000, 0, 1], the concentration of virus in the body proliferates to 12,000 virions per $mm^3$ in about 25 days. The infected T cell concentration also increases to 40 cells per $mm^3$ in the same amount of time. The uninfected/healthy T cell count falls to a drastically low value less than 100 cells $mm^3$ from its initial concentration but stabilizes to 240 cells per $mm^3$ in about 200 days. This slight increase in the healthy T cell count could be due to the immune system's response in fighting off the virus. The other two states also reach equilibrium in about 200 days after the initial infection.

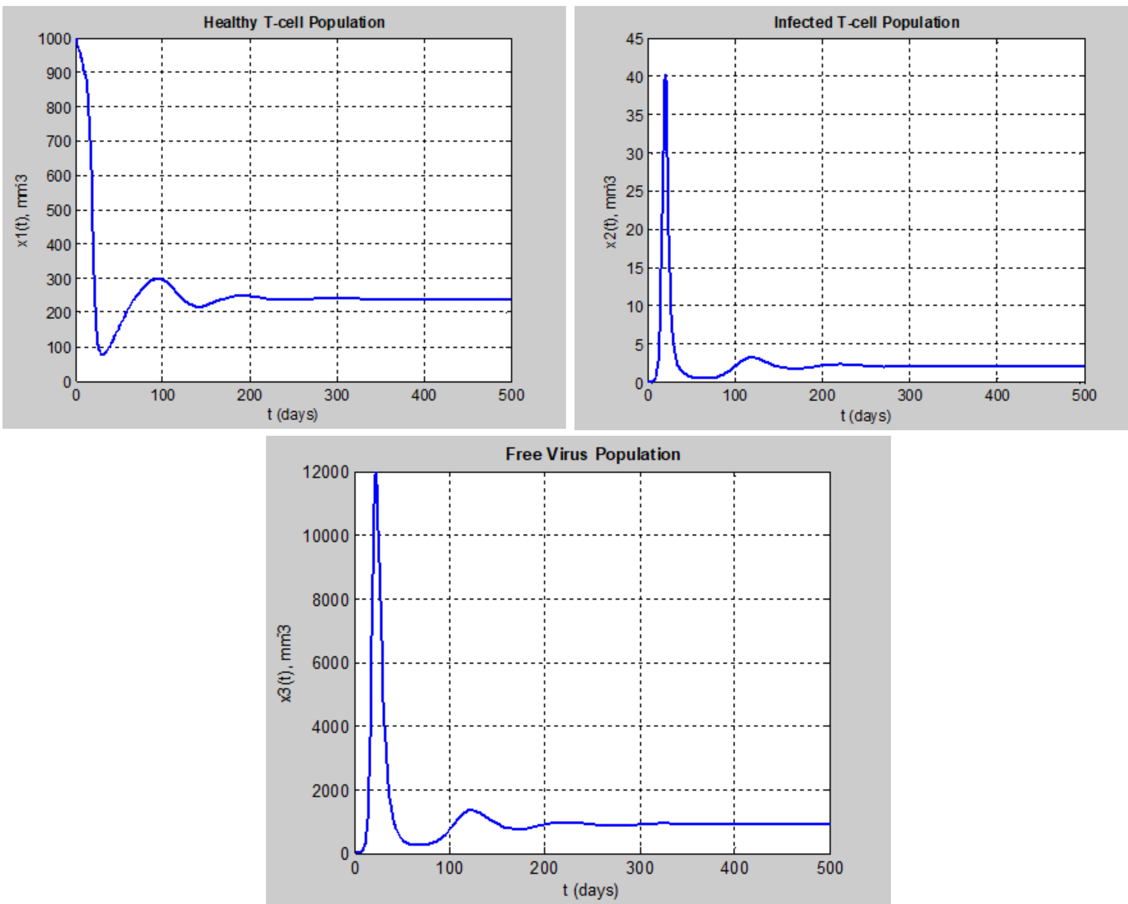


**Figure 4.6**: State response plots of the nonlinear HIV model

The behavior of the states as observed from the plots after 200 days is in agreement with the fact that the body enters an *endemically infected* state, and the final values of the states match the second equilibrium point. The period of 25 days since the initial infection was characterized by large dynamic changes, and constitutes the ‘acute infection’ phase.

Another observation made at this point was that there is not enough evidence to support the presence of time scales graphically. In the previous work with transmission lines, the slowly responding line temperature plot was easily distinguishable from the fast line current plot. In this case, eigenvalues have to be evaluated to mathematically establish the presence of time scales.

### 4.3.3 Linearization

The nonlinear HIV model was linearized at various instants of time and the corresponding eigenvalues were evaluated. Linearization was carried out in MATLAB® and Simulink®. The data provided in Table 4.1 were used for simulations.

**Table 4.3**: Linearization of HIV model at various time instants

| **Time instant (in days)** | **Eigenvalues** |
|---|---|
| t = 0 | -3.2085<br>-0.019993<br>0.56847 |
| t = 10 | -3.1461<br>-0.01866<br>0.50062 |
| t = 25 | -2.5397<br>-0.18407 + 0.15678*i*<br>-0.18407 – 0.15678*i* |
| t = 50 | -2.564<br>-0.052968 + 0.031887*i*<br>-0.052968 – 0.031887*i* |

| Time instant (in days) | Eigenvalues |
|---|---|
| t = 80 | -2.677<br>0.0052643 + 0.025293*i*<br>0.0052643 – 0.025293*i* |
| t = 100 | -2.6894<br>0.0057475 + 0.053418*i*<br>0.0057475 – 0.053418*i* |
| t = 150 | -2.6273<br>-0.027151 + 0.065469*i*<br>-0.027151 – 0.065469*i* |
| t = 200 | -2.6473<br>-0.017061 + 0.065242*i*<br>-0.017061 – 0.065242*i* |
| t = 400 | -2.6419<br>-0.01986 + 0.065713*i*<br>-0.01986 – 0.065713*i* |
| t = 500 | -2.6418<br>-0.019924 + 0.065777*i*<br>-0.019924 – 0.065777*i* |

The results indicate that the eigenvalues obtained for all time instants are clearly separated into groups, which differ by at least an order of magnitude from each other. This is clearly indicative of time scale behavior in the HIV model. The larger (absolute) eigenvalue corresponds to the faster time scale which is the viral dynamics and the smaller (absolute) eigenvalue corresponds to the slower time scale which is the uninfected T cell dynamics [11, 31, 32, 33]. These results are in accord with the findings of Perelson *et.al*. in [11], where the existence of slow and fast processes in the HIV dynamics were first confirmed through a combination of clinical data analysis and mathematical interpretation of this data. Since the HIV model has variables that change at different speeds, and interact with one another, it is well suited for Time Scale Analysis that facilitates design of optimal treatment strategies.

### 4.3.4 Non-Dimensionalization and Singular Perturbation Parameter

Having confirmed the existence of time scales through eigenvalues, the HIV model was further investigated for the explicit presence of a singular perturbation parameter, the causative agent for slow-fast behavior. This required a non-dimensionalization procedure on the model (4.1), which is recalled here for convenience.

$$\begin{aligned}\frac{dx_1(t)}{dt} &= s - Dx_1(t) - \beta x_1(t)x_3(t),\\ \frac{dx_2(t)}{dt} &= \beta x_1(t)x_3(t) - \mu_2 x_2(t),\\ \frac{dx_3(t)}{dt} &= kx_2(t) - \mu_1 x_3(t),\end{aligned} \tag{4.4}$$

The variables of the dimensionless HIV model were chosen as $T$, $X_1$, $X_2$ and $X_3$, corresponding to the original system variables $t$, $x_1$, $x_2$ and $x_3$ respectively, where,

$$\begin{aligned}T &= Dt\\ X_1 &= \left(\frac{D}{s}\right)x_1\\ X_2 &= \left(\frac{\mu_2}{s}\right)x_2\\ X_3 &= \left(\frac{\mu_1\mu_2}{s}\right)x_3\end{aligned} \tag{4.5}$$

Insights into the choice of reference variables for this analysis were obtained from reference [93]. The expected life times of healthy T cells, infected T cells and virus particles – $1/D$, $1/\mu_2$, and $1/\mu_1$ respectively, were possible choices for the dimensionless time variable, but since the ratio $1/D$ was the longest compared to others, it was chosen as the reference variable for time. The reference variable for healthy T cells was chosen with the reasoning that in the disease free equilibrium, $x_1 = s/D$, and for the infected cells, the reference quantity was chosen as $x_2 = s/\mu_2$. The reference quantity for the virus is chosen so that at equilibrium $X_2 = X_3$ [93].

Substituting $\frac{d}{dt} = D\frac{d}{dT}$ and $x_1$, $x_2$ and $x_3$ from (4.5), the dimensionless HIV model is obtained as,

$$\begin{aligned}
\frac{dX_1}{dT} &= 1 - X_1 - bX_1X_3, \\
\varepsilon\frac{dX_2}{dT} &= bX_1X_3 - X_2, \\
\theta\cdot\varepsilon\frac{dX_3}{dT} &= X_2 - X_3,
\end{aligned} \tag{4.6}$$

where, $b = \frac{\beta ks}{D\mu_1\mu_2}$, $\varepsilon = \frac{D}{\mu_2}$ and $\theta = \frac{\mu_2}{\mu_1}$. Substituting the numerical values of $\varepsilon$ and $\theta$, results in,

$$\begin{aligned}
\varepsilon = 0.0083,\ \theta = 10, \\
\theta\cdot\varepsilon = 0.0833
\end{aligned} \tag{4.7}$$

Rearranging $\theta$ as a factor (1/10) into the right hand side of $\dot{X}_3$ results in the standard singular perturbation form of the HIV model,

$$\begin{aligned}
\frac{dX_1}{dT} &= 1 - X_1 - bX_1X_3, \\
\varepsilon\frac{dX_2}{dT} &= bX_1X_3 - X_2, \\
\varepsilon\frac{dX_3}{dT} &= \frac{1}{10}\left(X_2 - X_3\right),
\end{aligned} \tag{4.8}$$

where $\varepsilon$ is a 'small parameter' or the 'singular perturbation parameter' responsible for imparting time scale characteristics to the HIV model. By definition, $\varepsilon$ is a ratio of reference times, *i.e*. ratio of the lifetime of an infected T cell to the lifetime of a healthy T cell. Comparing (4.8) to the standard singular perturbation form of equations,

$$\begin{aligned} \dot{x}(t) &= f(x, z, u, \varepsilon, t) \;\Rightarrow\; \textit{slow state} \\ \varepsilon \dot{z}(t) &= g(x, z, u, \varepsilon, t) \;\Rightarrow\; \textit{fast state} \end{aligned} \tag{4.9}$$

the slow state of the HIV model is identified to be the uninfected T cell, and the fast states are identified to be the infected T cell and free virus states.

Thus, the time scale nature of HIV model was identified through linearization and non-dimensionalization procedures. The presence of time scales in HIV dynamics provides an opportunity to investigate the effectiveness of the well-recognized SPaTS methods in designing treatment plans for HIV. The following section discusses the current optimal treatment plans for HIV, followed by the investigation of Time Scale Analysis and Synthesis in simplifying the existing treatment solutions.

## 4.4 Optimal Control Strategies for the Treatment of HIV Infection

Currently, the treatment of an HIV infection involves a combination of mechanisms inhibiting HIV enzymes, reverse *transcriptase* and *protease*. When *reverse transcriptase* is inhibited, HIV can enter a T cell but will not successfully infect it. When *protease* is inhibited, assembling of viral proteins fails to occur, and viral particles will be made that lack functional HIV enzymes, or new ‘noninfectious’ viral particles will be created [11].

Although an HIV infection is not yet curable, adherence to ART for long periods of time offer the best chance of effectively managing the disease. Since the antiretroviral drugs cannot get rid of the virus from the body, the treatment has to be continued for life. Patients on reverse transcriptase inhibitors (RTI) and protease inhibitors (PI) experience adverse side effects due to the potency of drugs [21] and this makes adherence to the therapy very difficult. Several optimal treatment strategies have been proposed in literature that achieves viral load suppression (or boosting of immune cells) while minimizing the cost of therapy. References [30] and [94] proposed a cost functional that minimize the virus population and cost of drug treatment, while authors in [22], [23] and [24] performed maximization of the T cells while minimizing the cost of drug treatment. LQR control methods have been also proposed in literature for designing long term treatments for HIV due to its simplicity and robustness properties [26], [87] and are of interest in this research.

### 4.4.1 Long Term Optimal Treatment Strategy

A treatment model incorporating combinations of RTI and PI classes of antiretroviral drugs is presented. A *long term, optimal treatment* strategy proposed by Radisavljevic-Gajic in [25] is adopted for this study, for investigating the efficacy of time scale design. The treatment strategy is such that the dosage of drugs is minimized while keeping the patient in a 'clinically stable steady state' for long periods of time. This is achieved with a two controllers – 1) a steady state control (nominal solution) that maintains the body at the desired steady state and 2) an optimal control (LQR) that minimizes any deviations from the desired steady state values in an optimal manner.

### 4.4.2 Nonlinear HIV Model with Control

The HIV model is equipped with two control variables, $u_1(t)$ and $u_2(t)$, corresponding to RTI and PI categories of antiretroviral drugs. The nonlinear state space model with control variables [25] is given as,

$$
\begin{aligned}
\frac{dx_1(t)}{dt} &= s - Dx_1(t) - (1-u_1(t))\beta x_1(t)x_3(t),\\
\frac{dx_2(t)}{dt} &= (1-u_1(t))\beta x_1(t)x_3(t) - \mu_2 x_2(t),\\
\frac{dx_3(t)}{dt} &= (1-u_2(t))kx_2(t) - \mu_1 x_3(t).
\end{aligned}
\tag{4.10}
$$

The descriptions of all model parameters are provided in Table 4.1. Control of viral load in the body is achieved by reducing the parameter $\beta$ (virus infectivity rate) and/or parameter $k$ (infected T-cell productivity of free virus particles). In the ART, this is achieved by RTI ($u_1$) acting on $\beta$ and PI ($u_2$) acting on $k$. The control variables are normalized to the range $0 \le u_j \le 1,\ j = 1,\ 2,$ with 1 corresponding to the maximal dosage and 0 corresponding to the situation where the drug is not administered.

Comparing the state-space model (4.10) to the representation of a standard nonlinear system, $\dot{\boldsymbol{x}} = f(\boldsymbol{x}, \boldsymbol{u}),$ the state vector, $\boldsymbol{x}$ and input vector, $\boldsymbol{u}$ are defined as,

$$
\begin{aligned}
\boldsymbol{x} &= \begin{bmatrix} x_1 \\ x_2 \\ x_3 \end{bmatrix} \Rightarrow \begin{bmatrix} Uninfected\ CD4^{+}Tcell \\ Infected\ CD4^{+}Tcell \\ Free\ virus \end{bmatrix},\\
\boldsymbol{u} &= \begin{bmatrix} u_1 & u_2 \end{bmatrix} \Rightarrow \begin{bmatrix} RTI & PI \end{bmatrix}.
\end{aligned}
\tag{4.11}
$$

### 4.4.3 Steady State (Nominal) Control and LQR Control

The *steady state controller* maintains the concentration of uninfected T cells, infected T cells and free virus at the desired steady states, and an *optimal controller* minimizes any deviations from the steady states to zero, i.e.,

$$
u_i(t) = u_i^{*} + \Delta u_i(t), \quad i = 1, 2, \tag{4.12}
$$

where $u_i^{*}$ denotes the steady state control inputs and $\Delta u_i(t)$ are small time varying components that will be determined by the LQR control. Similarly, the state variables satisfy the relation,

$$x_i(t) = x_i^* + \Delta x_i(t), \quad i = 1,2,3 \tag{4.13}$$

where $x_i^*$ denotes the constant values of states and $\Delta x_i(t)$ are the state deviations that are controlled optimally.

**Steady State (Nominal) Control**

By setting the derivatives of (4.10), the desired steady state values in terms of control inputs are obtained as,

$$\begin{aligned} 0 &= s - Dx_1^* - (1-u_1^*)\beta x_1^* x_3^*, \\ 0 &= (1-u_1^*)\beta x_1^* x_3^* - \mu_2 x_2^*, \\ 0 &= (1-u_2^*)kx_2^* - \mu_1 x_3^*. \end{aligned} \tag{4.14}$$

From the above equations, relationships between $x_1^*$ and $x_2^*$ can be derived as,

$$x_2^* = \frac{s - Dx_1^*}{\mu_2} \tag{4.15}$$

The above relationship is independent of the state $x_3^*$. Therefore, once the target values of $x_1$ (and $x_3$) are defined – $x_{1tar}^*$ (and $x_{3tar}^*$ respectively), the target value for $x_2$ (i.e. $x_{2tar}^*$) can be easily determined from (4.15). The control inputs required to maintain the states at their target values are obtained from (4.14) as,

$$\begin{aligned} u_{1tar}^* &= 1 - \frac{\mu_2 x_{2tar}^*}{\beta x_{1tar}^* x_{3tar}^*} \\ u_{2tar}^* &= 1 - \frac{\mu_1 x_{3tar}^*}{k x_{2tar}^*} \end{aligned} \tag{4.16}$$

**Full Order LQR Control**

To design LQR control, the nonlinear, HIV model with control (4.10) is first linearized about an operating point ($[x_{1tar}^*, x_{2tar}^*, x_{3tar}^*]$, $[u_{1tar}^*, u_{2tar}^*]$). (The choice of this operating point is discussed in the following section). Thus, for small perturbations near the target values,

$$\begin{aligned} x_1 &= x_{1tar}^* + \Delta x_1, \\ x_2 &= x_{2tar}^* + \Delta x_2, \\ x_3 &= x_{3tar}^* + \Delta x_3, \end{aligned} \tag{4.17}$$

corresponding to small adjustments in the control variables,

$$\begin{aligned} u_1 &= u_{1tar}^* + \Delta u_1, \\ u_2 &= u_{2tar}^* + \Delta u_2, \end{aligned} \tag{4.18}$$

and neglecting the higher order terms in the Taylor's approximation, one can write

$$\Delta \dot{x} = \left.\frac{\delta f}{\delta x}\right|_{(x_{tar}^*, u_{tar}^*)} \Delta x \; + \; \left.\frac{\delta f}{\delta u}\right|_{(x_{tar}^*, u_{tar}^*)} \Delta u \tag{4.19}$$

or,

$$\begin{aligned} \begin{bmatrix} \Delta \dot{x}_1(t) \\ \Delta \dot{x}_2(t) \\ \Delta \dot{x}_3(t) \end{bmatrix} &= \begin{bmatrix} -D-(1-u_{1tar}^*)\beta x_{3tar}^* & 0 & -(1-u_{1tar}^*)\beta x_{1tar}^* \\ (1-u_{1tar}^*)\beta x_{3tar}^* & -\mu_2 & (1-u_{1tar}^*)\beta x_{1tar}^* \\ 0 & (1-u_{2tar}^*)k & -\mu_1 \end{bmatrix} \begin{bmatrix} \Delta x_1(t) \\ \Delta x_2(t) \\ \Delta x_3(t) \end{bmatrix} \\ &+ \begin{bmatrix} \beta x_{1tar}^* x_{3tar}^* & 0 \\ -\beta x_{1tar}^* x_{3tar}^* & 0 \\ 0 & -k x_{2tar}^* \end{bmatrix} \begin{bmatrix} \Delta u_1(t) \\ \Delta u_2(t) \end{bmatrix}. \end{aligned} \tag{4.20}$$

The linear HIV model (4.20) is of the form $\Delta \dot{x} = A\Delta x + B\Delta u$ and is in terms of the target states and target control inputs.

The quadratic performance criterion for optimal LQR control is given as,

$$J = \frac{1}{2}\int_0^\infty \left[ \Delta \boldsymbol{x}^T(t) Q \Delta \boldsymbol{x}(t) + \Delta u_{opt}^T(t) R \Delta u_{opt}^T(t) \right] dt, \tag{4.21}$$

and the optimal control deviations $\Delta u_{opt}(t)$ is defined as,

$$\Delta u_{opt}(t) = -R^{-1} B^T P \Delta x(t) = -K \Delta x(t). \tag{4.22}$$

The reader is referred to Section 2.4.2 for a detailed formulation of a full order LQR design. The LQR component of the long term strategy is described in Figure 4.7.

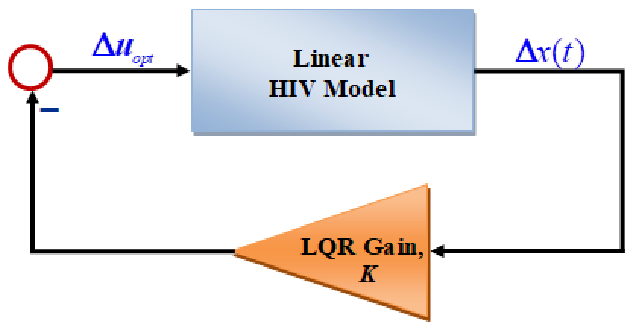


**Figure 4.7**: LQR control for the *full order* HIV model

The combination of the steady state control and LQR control in the long term treatment strategy is illustrated in Figure 4.8. The nominal solution block represents the steady state controller.

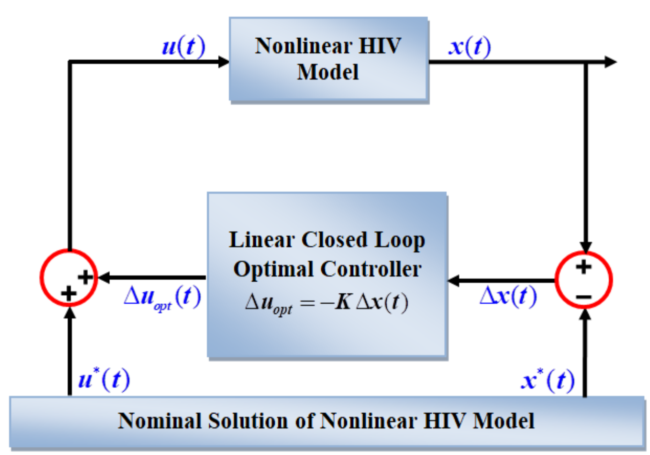


**Figure 4.8:** Long term optimal treatment strategy for HIV

**Selection of Target Values**

The U.S. Department of Health and Human Services offers guidelines for the antiretroviral treatment of HIV [82]. Desired levels of healthy T-cells $(x_1)$ and viral load $(x_3)$ are recommended for several phases of treatment. The normal CD4$^+$ T cell count ranges from 500 – 1000 per mm$^3$. The guidelines recommend the viral load to be suppressed below 50 per mm$^3$. Based on these guidelines, target values for the states are chosen as $x_{1tar}^*$ = 490 per mm$^3$ and $x_{3tar}^*$ = 30 per mm$^3$ [25]. Target values of $x_{2tar}^*$ and control inputs, $u_{1tar}^*$ and $u_{2tar}^*$, are calculated from equations (4.15) and (4.16) respectively. The target steady state values (operating points) are,

$$\begin{aligned}\left[x_{1tar}^*, x_{2tar}^*, x_{3tar}^*\right]^T &= \left[490, 0.0833, 30\right]^T; \\ \left[u_{1tar}^*, u_{2tar}^*\right]^T &= \left[0.4333, 0.1356\right]^T;\end{aligned} \tag{4.23}$$

The $A$ and $B$ matrices of the linear HIV model about the operating point (4.23) were obtained as,

$$A = \begin{bmatrix} -0.0204 & 0 & -0.006664 \\ 0.000041 & -2.4 & 0.006664 \\ 0 & 86.44 & -0.24 \end{bmatrix}; \quad B = \begin{bmatrix} 0.3528 & 0 \\ -0.3528 & 0 \\ 0 & -8.33 \end{bmatrix} \tag{4.24}$$

## 4.5 Time Scale Analysis and Synthesis of HIV Model

The ultimate objective of time scale synthesis is to apply the slow and fast control laws in the long term treatment strategy and evaluate its effectiveness in maintaining the patient at the desired target values. Figure 4.9 highlights the role of time scale synthesis in the long term strategy, where the full order LQR gain block is transformed into slow and fast gains through time scale synthesis.

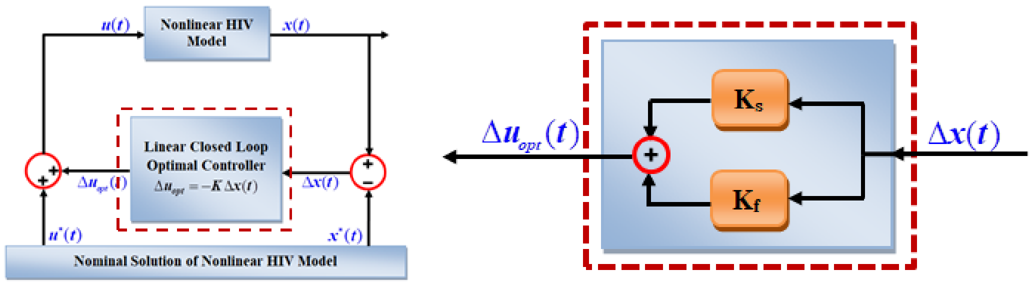


**Figure 4.9:** Time scale synthesis of LQR control in HIV treatment

But as a preliminary evaluation, the performance of time scale LQR design is first assessed outside the long term strategy, i.e. on the *linear* HIV model to see if the slow and fast controllers are capable of regulating small deviations in the system. To achieve this, the linear HIV model is subjected to time scale analysis that results in slow and fast subsystems, each of which are assigned a quadratic performance index. The corresponding slow and fast control laws are derived and combined to form a composite control. The performance of this time scale design is compared to a full order LQR design on the linear HIV model, which was described in Section 4.4.3.

### 4.5.1 Time Scale Analysis of Linear HIV Model

The eigenvalues of the linear model in (4.24) are evaluated and found to be different from each other by an order of magnitude, thereby confirming the presence of time scales (Table 4.4). The linear model was then subjected to Time Scale Analysis described in Section 2.3. When rewritten in the standard time scale form,

$$\begin{aligned} \dot{x} &= A_1 x + A_2 z + B_1 u, \\ \dot{z} &= A_3 x + A_4 z + B_2 u, \end{aligned} \qquad (4.25)$$

the states of the linear HIV model are, $x = [x_1(t)]$ and $z = [x_2(t), x_3(t)]^T$, and the matrices

$A_1$ to $A_4$ and $B_1$ to $B_2$ were defined as,

$$A_1 = [-0.0204], \qquad A_2 = [0 \quad -0.006664], \qquad B_1 = [0.3528 \quad 0],$$
$$A_3 = \begin{bmatrix} 0.000041 \\ 0 \end{bmatrix}, \qquad A_4 = \begin{bmatrix} -2.4 & 0.006664 \\ 86.44 & -0.24 \end{bmatrix}, \qquad B_2 = \begin{bmatrix} -0.3528 & 0 \\ 0 & -8.33 \end{bmatrix}. \tag{4.26}$$

### 4.5.2 Separation of HIV dynamics

The slow and fast subsystems, $x_s(t)$ and $x_f(t)$ obtained after applying the two-stage transformation (Section 2.3.2) are,

$$\begin{aligned} \dot{x}_s(t) &= A_s x_s(t) + B_s u(t), \\ \dot{z}_f(t) &= A_f z_f(t) + B_f u(t), \end{aligned} \tag{4.27}$$

where, the matrices were obtained as,

$$\begin{aligned} A_s &= [-0.006267], & A_f &= \begin{bmatrix} -2.4 & 0.006626 \\ 86.44 & -0.2541 \end{bmatrix}, \\ B_s &= [9.5868 \quad 6.4536], & B_f &= \begin{bmatrix} -0.3507 & 0 \\ 0.7482 & -8.33 \end{bmatrix}. \end{aligned} \tag{4.28}$$

The decoupled HIV model dynamics is represented as,

$$\begin{array}{c} \dot{x}_s \\ \dot{z}_f \end{array} \begin{bmatrix} \Delta\dot{x}_1 \\ \Delta\dot{x}_2 \\ \Delta\dot{x}_3 \end{bmatrix} = \begin{bmatrix} \overset{A_s}{-0.006267} & 0 & 0 \\ 0 & -2.4 & 0.006626 \\ 0 & 86.44 & -0.2541 \end{bmatrix}_{A_f} \begin{bmatrix} \Delta x_1 \\ \Delta x_2 \\ \Delta x_3 \end{bmatrix} + \begin{bmatrix} 9.5868 & 6.4536 \\ -0.3507 & 0 \\ 0.7482 & -8.33 \end{bmatrix}^{B_s}_{B_f} \begin{bmatrix} \Delta u_1 \\ \Delta u_2 \end{bmatrix} \tag{4.29}$$

The eigenvalues of the full order and reduced order systems were compared to ensure that the decoupled subsystems retain the slow and fast dynamics. The results in Table 4.4 confirm that an almost perfect decoupling was performed on the HIV dynamics. The accuracy parameter of Newton's algorithm could be adjusted to get the exact same eigenvalues for both the systems. The decoupled HIV subsystems are now utilized for the time scale synthesis of optimal LQR control.

**Table 4.4**: Comparison of eigenvalues of full order and reduced order HIV model

| **Full order system** | **Eigenvalues** |
|---|---|
| $A$ | eig($A$) = -0.0063276<br>-0.014025<br>-2.64 |
| **Reduced order systems** | **Eigenvalues** |
| $A_s$ (Slow subsystem) | eig( $A_s$ ) = -0.006267 |
| $A_f$ (Fast subsystem) | eig( $A_f$ ) = -0.014085<br>-2.64 |

### 4.5.3 Slow and Fast LQR Control

The slow subsystem defined in (4.27), has a performance index,

$$J_s = \frac{1}{2}\int_0^\infty \left[ \Delta x_s^T(t) Q_s \Delta x_s(t) + \Delta u_s^T(t) R_s \Delta u_s(t) \right] dt, \tag{4.30}$$

whose optimal control signal $\Delta u_s^{opt}(t)$ for the slow subsystem is derived as,

$$\Delta u_s^{opt}(t) = -K_s \Delta x_s(t) = -R_s^{-1} B_s^T P_s \Delta x_s(t). \tag{4.31}$$

Similarly, for the fast subsystem (4.27), the LQR control is derived as,

$$\Delta u_f^{opt}(t) = -K_f \Delta x_f(t) = -R_f^{-1} B_f^T P_f \Delta x_f(t), \tag{4.32}$$

The control fed back to the system is a *composite control* signal of the form,

$$\Delta u_{opt}(t) = \Delta u_s^{opt}(t) + \Delta u_f^{opt}(t). \tag{4.33}$$

All the parameters in the above equations and their detailed formulations are provided in Section 2.4.2. The independent processing of control laws highlights the fact that computational '*stiffness*' associated with the HIV dynamics was handled effectively. Also the two LQR gains, $K_s$ and $K_f$, are now of lower orders, 1st and 2nd order matrices respectively, compared to the full order gain, $K$ which is a 3rd order matrix. The time scale synthesis of LQR is presented in Figure 4.10.

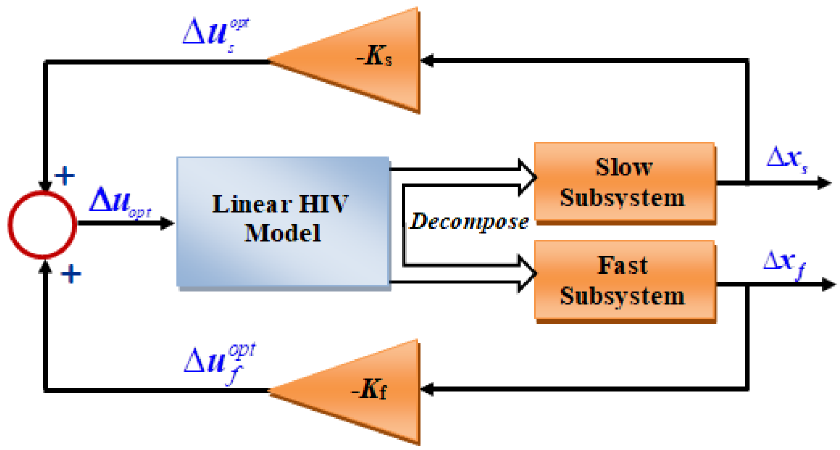


**Figure 4.10:** LQR control for linear HIV model using time scale separation

### 4.6 Simulations and Results of LQR Control

The LQR design is performed in MATLAB® and Simulink® for full order and reduced order cases. The numerical values of the system parameters are provided in Table 4.1 and the weights for the optimal control $Q_s$, $Q_f$, $R_s$ and $R_f$ are chosen based on trial and error. The controllability conditions for both the cases are tested using MATLAB®'s '`ctrb(A,B)`' command.

#### 4.6.1 Full Order LQR Results

The controllability matrix was found to have a full rank of 3 and the linear HIV model is therefore controllable. The weighting matrices are chosen as,

$$Q=\begin{bmatrix}0.001 & 0 & 0\\ 0 & 0.001 & 0\\ 0 & 0 & 0.001\end{bmatrix};\quad R=\begin{bmatrix}1 & 0\\ 0 & 1\end{bmatrix} \tag{4.34}$$

which lead to a LQR gain,

$$K=\begin{bmatrix}0.0060723 & -0.76054 & -0.022914\\ -0.0010398 & -0.54206 & -0.017779\end{bmatrix} \tag{4.35}$$

A Simulink® model for the full order linear HIV model is built as shown in Figure 4.11. The full order gain, $K$ is applied to all the states. The saturation block in the model has upper and lower limits set to one and zero, respectively, due to the fact that the control variables in (4.10) are normalized to the interval $0 \le u_j \le 1,\ j=1,2$ [25]. The initial conditions of the simulations are chosen to denote small deviations from the desired steady state values.

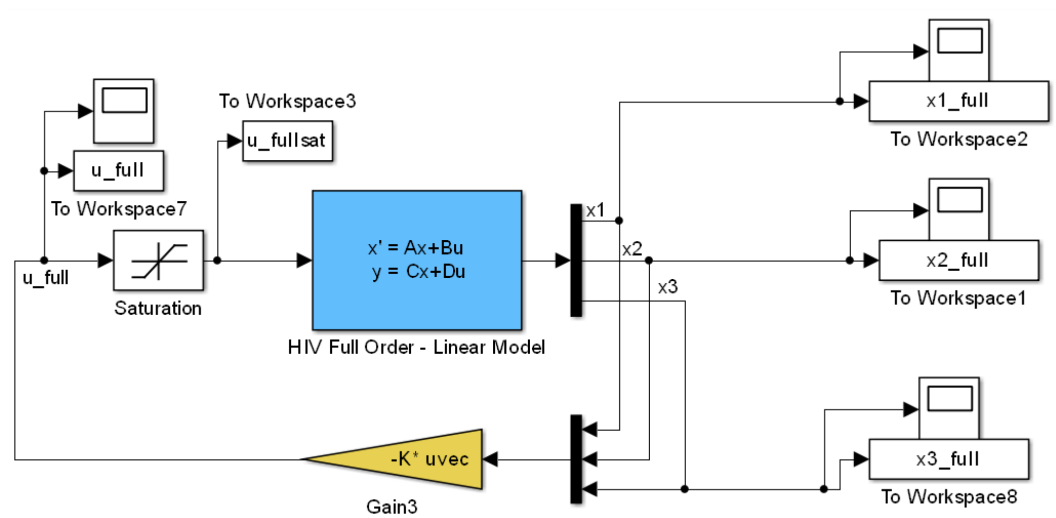


**Figure 4.11:** Simulink model - *full order* LQR design of linear HIV model

The results of the simulation are provided in Figure 4.12. From the plots, it is observed that all the state deviations are brought to zero by dispensing small amounts of control.

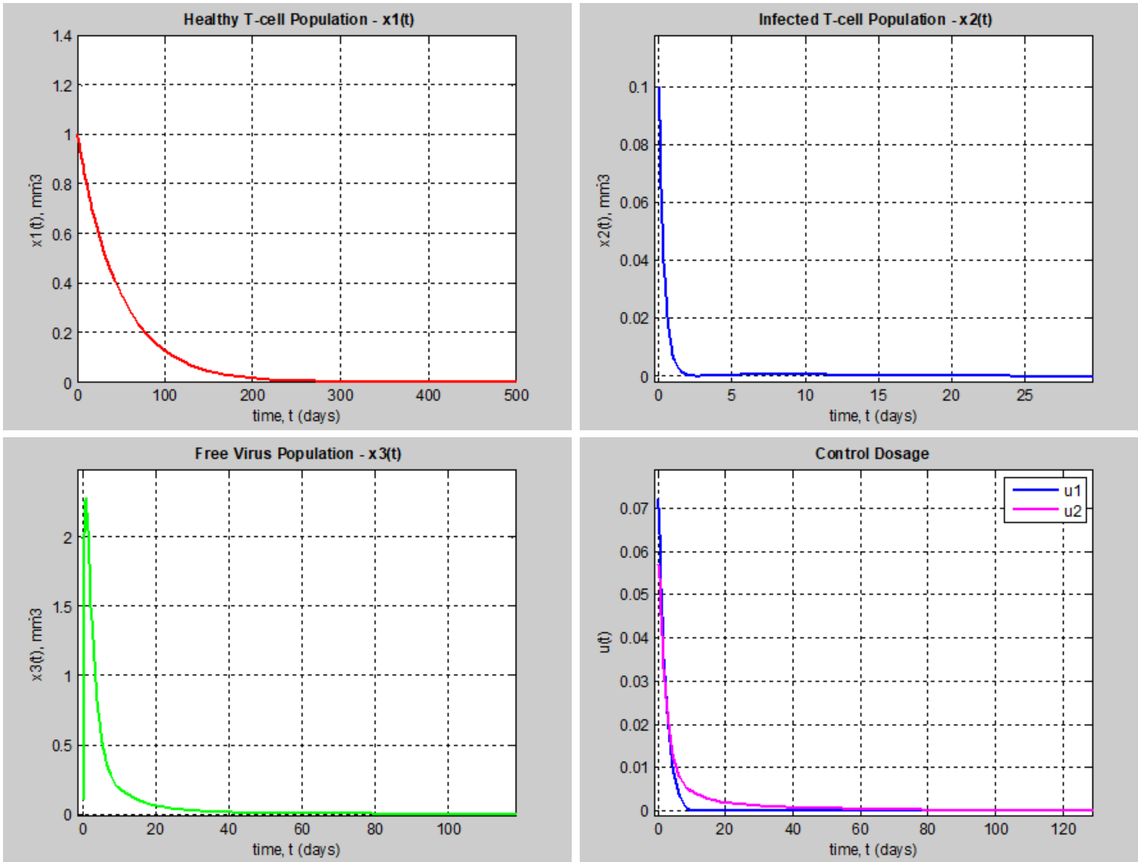


**Figure 4.12:** LQR control response of the full order, linear HIV model

The state deviation $\Delta x_1(t)$ is observed to take a longer time to reach zero compared to other states. This could be due to the slow time scale characteristic of the state $x_1(t)$. The time taken for the states to decline to zero could be further minimized by adjusting the $Q$ matrix of the quadratic function.

### 4.6.2 Reduced Order LQR Results

The controllability matrices for the slow and fast subsystems are verified. A full rank of 1 and 2 were obtained for the controllability matrices of the slow and fast subsystems, respectively, thereby rendering them controllable. By choosing the weighting matrices as,

$$Q_s = [0.001], \quad R_s = \begin{bmatrix} 1 & 0 \\ 0 & 1 \end{bmatrix},$$
$$Q_f = \begin{bmatrix} 0.001 & 0 \\ 0 & 0.001 \end{bmatrix}, \quad R_f = \begin{bmatrix} 1 & 0 \\ 0 & 1 \end{bmatrix}, \tag{4.36}$$

the slow and fast gains are calculated to be,

$$K_s = \begin{bmatrix} 0.025787 \\ 0.017359 \end{bmatrix}; \quad K_f = \begin{bmatrix} -0.72262 & -0.021494 \\ -0.54855 & -0.01788 \end{bmatrix}, \tag{4.37}$$

respectively. The Simulink® model is built for the reduced order transmission line as shown in Figure 4.13. The slow optimal gain, $K_s$ is applied to the state $x_1$ (uninfected T cell) and the fast gain, $K_f$ is applied to the states $x_2$ (infected T cell) and $x_3$ (free virus).

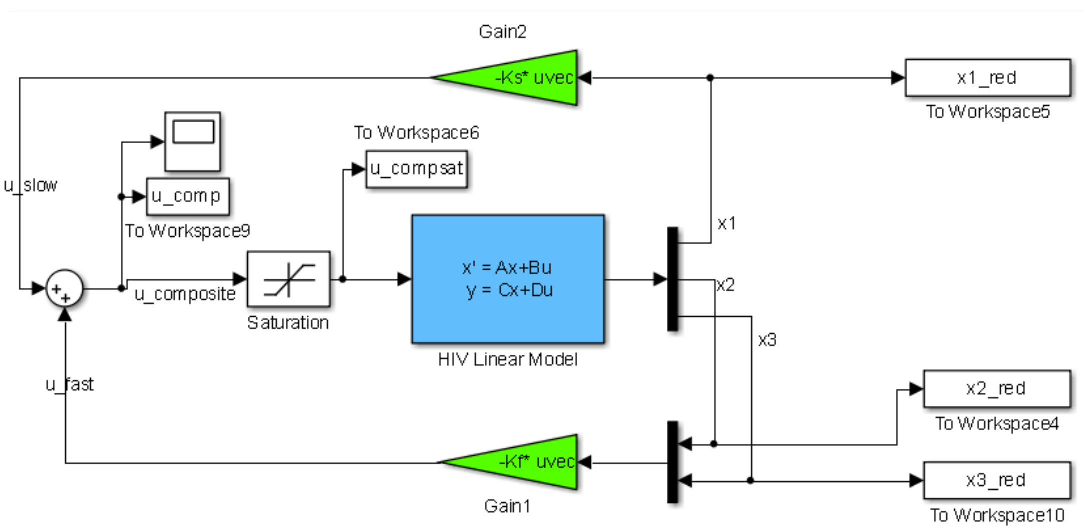


**Figure 4.13:** Simulink model - *reduced order* LQR design of linear HIV model

The saturation block enforces the upper and lower bounds for the normalized control inputs as in the previous case. The plots of the states and control signal are provided in Figure 4.13.

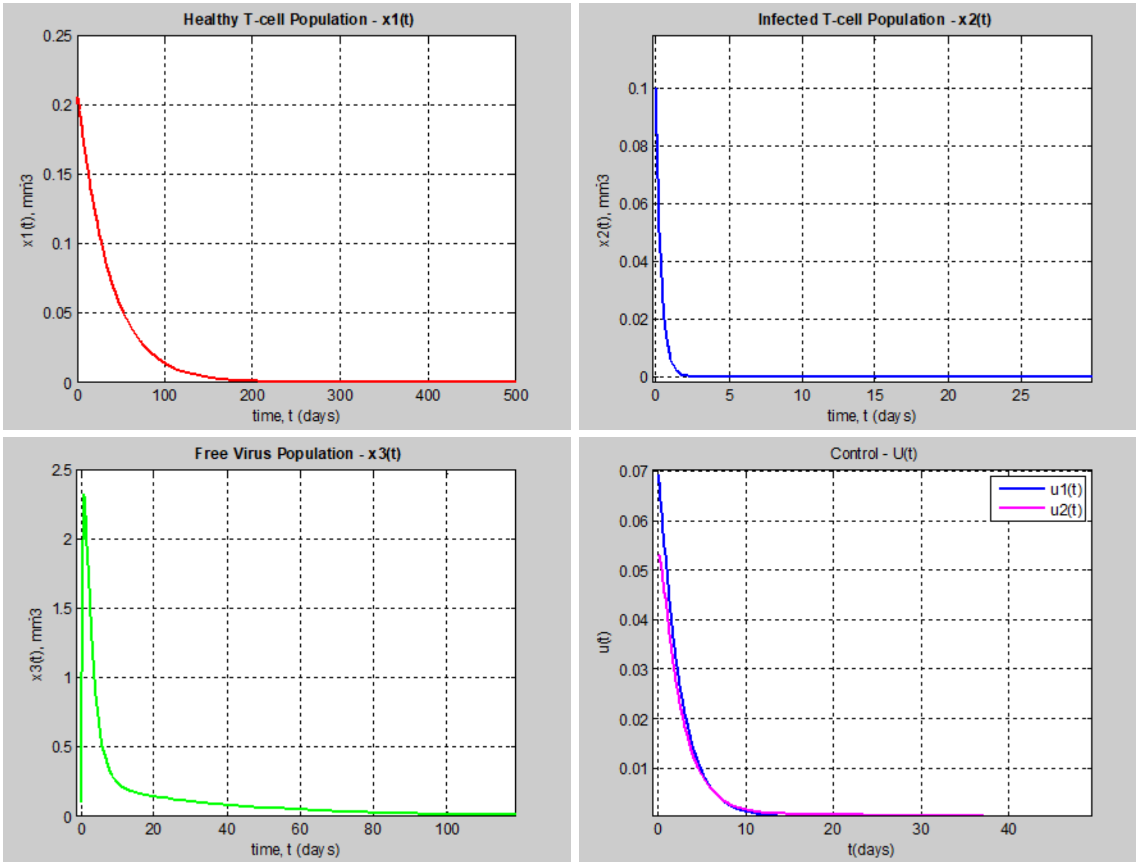


**Figure 4.14:** LQR control response of the reduced order, linear HIV model

The slow and fast controllers are observed to successfully minimize the deviations to zero. It is observed that small deviations in the states demanded only small control efforts to regulate them to zero as in the previous case. The time taken for the states to decline to zero could be further minimized by adjusting the weights $Q_s$ and $Q_f$ of the respective quadratic functions.

### 4.6.3 Comparison of Full order and Reduced Order LQR Results

Each of the state plots and control signals in the full order system are compared to their reduced order counterparts and the results are provided in Figures 4.15 and 4.16.

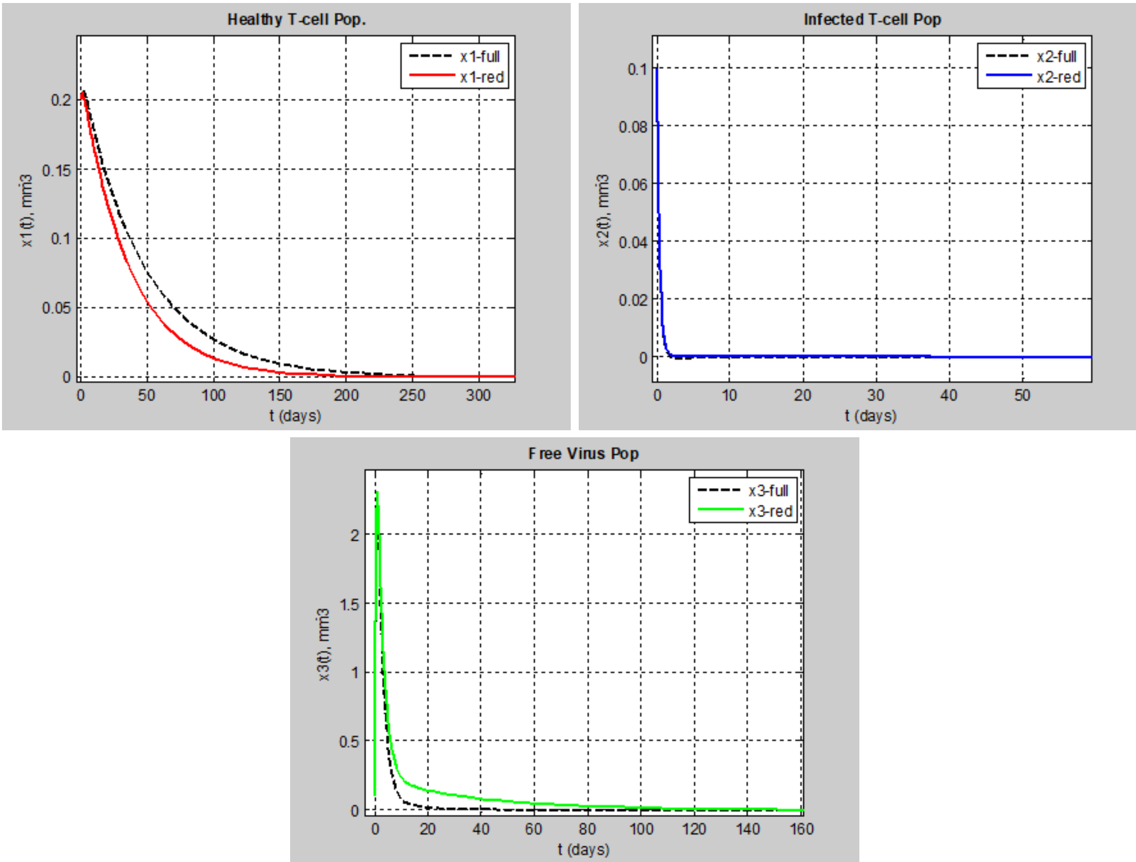


**Figure 4.15:** Comparison of full order and reduced order LQR - states $x_1$, $x_2$ and $x_3$

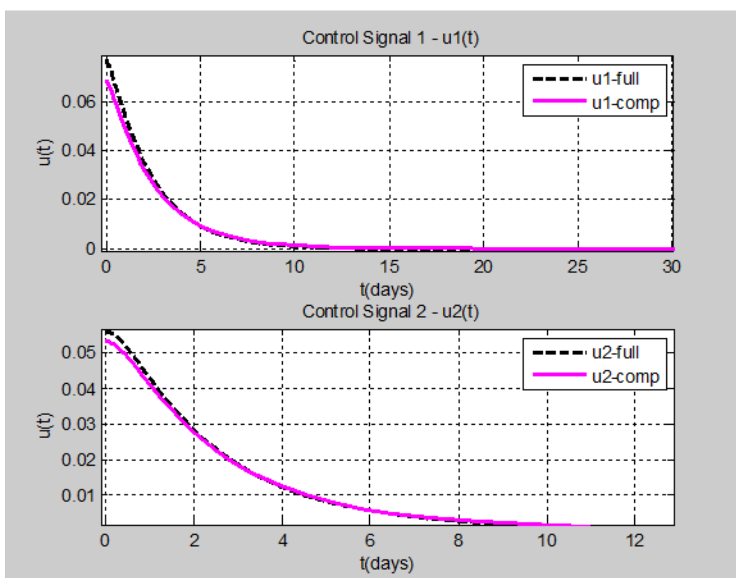


**Figure 4.16:** Comparison of full order and composite LQR control signals

The plots verify the closeness of full order LQR and reduced order control which establishes the efficacy of time scale methods, that almost identical control action was obtained with lower order controllers. The reduced order design demands lesser computational effort than its full order counterparts, and the resulting control laws are relatively simple. The strengths of this approach become substantial when HIV model dimensions exceed a third order or a fourth order, which is mostly the case with HIV treatment models. In such scenarios, the proposed control approach, that facilitates model order reductions, becomes inevitable for designing simple and practical treatment plans.

### 4.7 Long Term Treatment of HIV with Composite LQR Control

In the previous sections, the LQR component of the long term treatment plan was evaluated on the linear HIV model (i.e. LQR gains were fed back to linear HIV model) and the results indicated that the time scale design was at par with that of the full order design. In this section, a more practical scenario is investigated where the composite (slow + fast) LQR control is fed back to the *nonlinear* HIV model as part of the optimal long term treatment plan.

The ability of the composite LQR controller to maintain the states at the desired target values is investigated. A block diagram describing the LQR feedback on the nonlinear HIV treatment model is provided in Figure 4.17. The steady state values are provided by the nominal solution block. The block and dashed arrows describes the decomposition procedures that led to the design of slow and fast gains, $K_s$ and $K_f$. The solid arrows indicate the flow of signals in the model. A Simulink model is built to implement the long term treatment strategy with composite control (Figure 4.18).

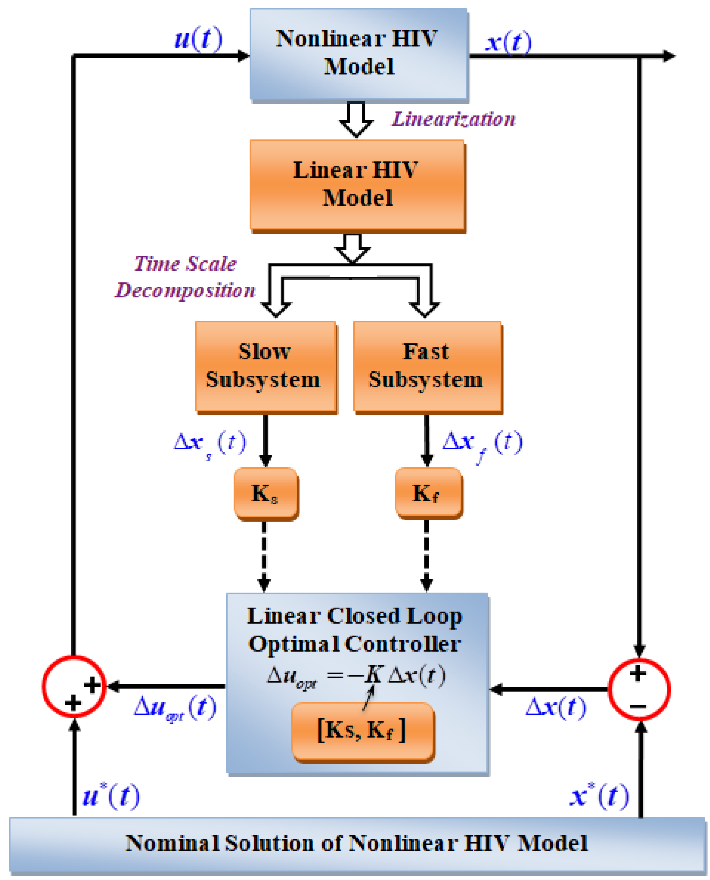


**Figure 4.17:** Time scale synthesis of long term treatment strategy with *nonlinear* HIV model

The 'Nonlinear HIV Model' block implements the dynamic equations in the HIV treatment model (4.10). The 'nominal solution' block supplies the desired steady state values of [490; 0.0833; 30] for $x_1(t)$, $x_2(t)$ and $x_3(t)$, and [0.4333, 0.1356] for $u_1(t)$ and $u_2(t)$. These values meet the U.S. Department of Health and Human Services HIV Therapy Guidelines. The slow and fast state deviations, $\Delta x_s(t)$ and $\Delta x_f(t)$ are fed to the respective gains. The composite LQR control $\Delta u_{opt}(t)$ is combined with the nominal control and fed back to the nonlinear HIV block.

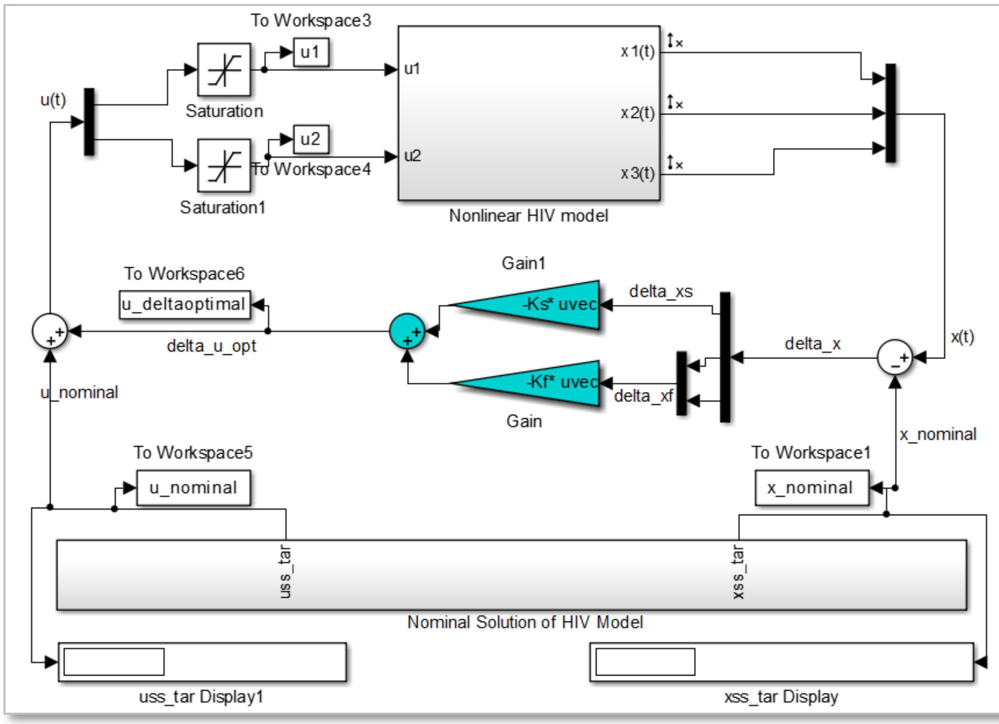


**Figure 4.18:** Simulink model for composite LQR control of nonlinear HIV model

The initial conditions for this simulation are obtained from [25] and were chosen such that they are outside the range of the desired target values. Table 4.5 lists the choice of initial conditions.

**Table 4.5:** Initial conditions for simulating nonlinear HIV model [25]

| Parameter | Description | Numerical Value |
|---|---|---|
| $x_1(0)$ | Healthy T- cell population | 560 per mm$^3$ |
| $x_2(0)$ | Infected T- cell population | 0.084 per mm$^3$ |
| $x_3(0)$ | Infectious HIV population | 60 per mm$^3$ |

The results of simulation – state and control responses are displayed in Figure 4.19 and Figure 4.20, respectively. It can be observed from the plots that the composite LQR controller was successful in maintaining the states of the nonlinear model at the desired levels. The state $x_1(t)$ was observed to reach the target value in approximately 150 days. The virus population was brought down to the steady state value very rapidly in slightly less than 3 days, and it remains at that level for the rest of the simulation period of 500 days. The concentration of infected T cells remained at the target value of 0.08 per mm$^3$.

From the control responses in Figure 4.20, it was observed that $u_1(t)$ or RTI drug was not administered for an initial duration of 80 days and was increased to a value of 0.43 after a period of about 170 days. The second control, $u_2(t)$ or the PI drug was administered at

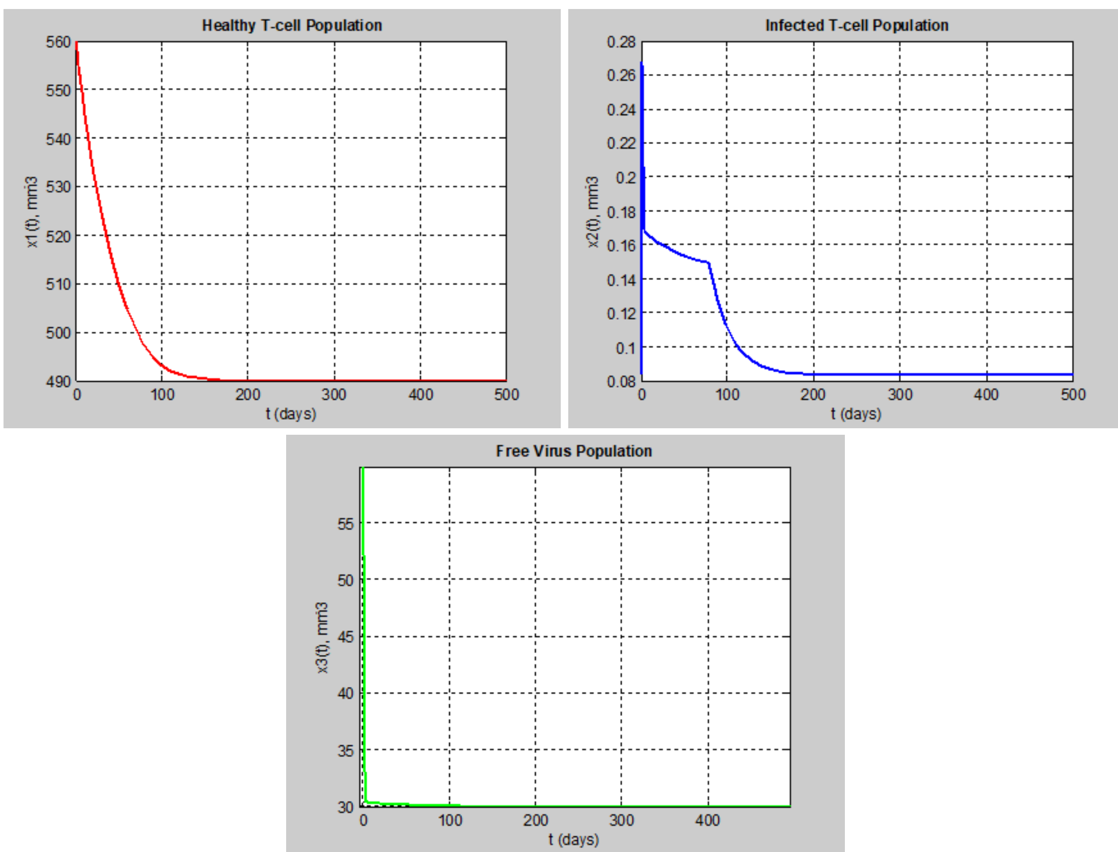


**Figure 4.19:** States of nonlinear HIV model with composite LQR control

the maximum dosage ($u_2(t) = 1$) for less than 3 days, which later on waned to a value of 0.136, the control input necessary to keep the states on target. This is evident from the detailed plot of the control response near the origin. An earlier observation on the very rapid decline of virus concentration (< 3 days) could be linked to the high PI dosage for the same amount of time. Since RTIs were not administered during that period, maximum dosage of PI was required to suppress the initial viral load in the body. After about 200 days the control dosage stabilizes to the designed target values.

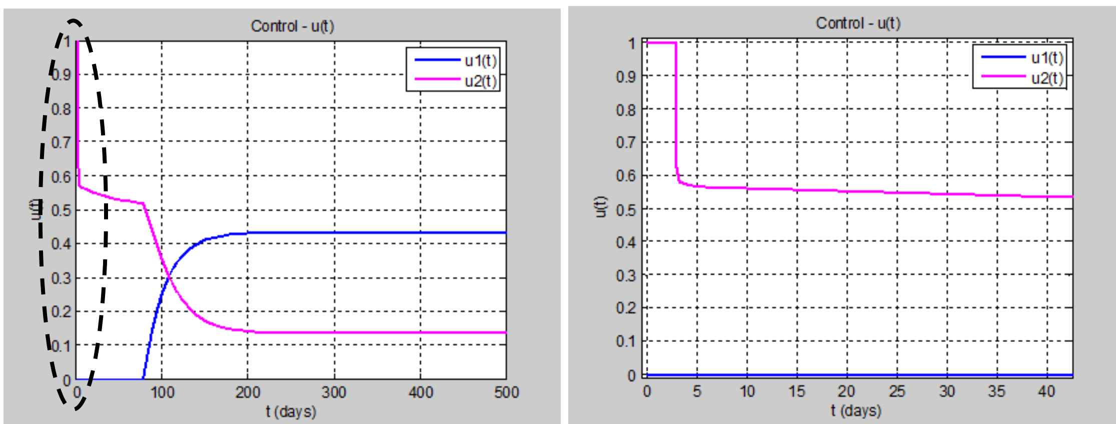


**Figure 4.20:** Control inputs of the optimal control of nonlinear HIV model (left); Detailed plot of control inputs near origin (right)

The results imply that lower order control laws were very effective in maintaining the patient in a clinically stable state. The implications of time scale methods become pronounced when comprehensive models of HIV dynamics are considered, such as models involving addition of immune system interactions (i.e. CD8$^{+}$ T cell or "killer T cell" dynamics) to the existing viral and uninfected CD4$^{+}$ T cell dynamics [20]. This modeling approach supports investigations of a new treatment plan called Structured Treatment Interruption (STI) which is a planned interruption of drugs at 'favorable' times in the course of ART. The addition of CD8$^{+}$ dynamics renders the simplest model with an order 6. Time scale methods presented in this research could help in pursuing effective control strategies even with such detailed models that yield simple and effective feasible treatment plans.

### 4.8 Research Work on Measles Infection

A brief amount of time was spent studying the measles disease model during the initial research period. The disease model couldn't be analyzed thoroughly for the application of SPaTS methods, as there was difficulty in assessing the time scale behavior of the model with certainty. Standard procedures like linearization and eigenvalue calculations were performed on this model, but a uniform time scale behavior couldn't be established from the simulation results. A brief overview of measles, the issues encountered and the summary of the work performed is provided in the following sections.

#### 4.8.1 Disease Background

Measles, a highly contagious disease among children, is one of the most common and often a fatal disease in the world. It is caused by the measles virus, a single stranded RNA virus of the genus *Morbillivirus* that infects the respiratory system and attacks the immune system. The infected individuals transmit the virus to over 90% of unprotected close contacts, making children under the age of 5 very vulnerable [95]. There is no specific treatment for measles, but unlike HIV/AIDS, measles is preventable by the Measles Mumps-Rubella (MMR) vaccine, and routine measles vaccination for children is the key public health strategy to prevent the disease.

However, WHO reported this disease, in 2017, as one of the leading causes of death among young children globally, despite the availability of a safe and effective vaccine

[96]. Consequently, modeling of transmission dynamics and optimal vaccination schemes are mainstream research areas of this infectious disease. This research work was conducted with the objective of investigating the optimal vaccination strategy for control of this disease through the application of time scale methods.

### 4.8.2 Measles Transmission and Control Dynamics

Epidemiological models have been widely used in literature for understanding the transmission of diseases and for testing various prevention and control therapy schemes [97], [98]. These models stratify the population into compartments which represent the status of their health with respect to the pathogen in the system. The Susceptible-Infectious-Recovered (SIR) model is one of the common compartmental models, consisting of three compartments representing the number of susceptible, infectious and recovered/immune individuals. The dynamic model for this research is adopted from literature [47], and is a SIR model with vaccination schemes.

The state space model for the measles transmission and control is described as [47],

$$\begin{aligned}\frac{dS}{dt} &= b - \mu S - \psi(t)S - \beta(t)SI,\\ \frac{dI}{dt} &= -\mu I + \beta(t)SI - \alpha I,\\ \frac{dR}{dt} &= -\mu R + \psi(t)S + \alpha I,\end{aligned} \tag{4.38}$$

where *S*, *I* and *R* are the state variables. The total population is defined as,

$$N(t) = S(t) + I(t) + R(t). \tag{4.39}$$

The influx rate into the population is denoted by *b*, $\mu$ is the exit rate from the population compartment (rather than mortality) and $\alpha$ is the recovery rate. The vaccination rate (control) is expressed by the term $\psi(t)$ and is assumed to be periodic. The contact rate is given by $\beta(t)$ and is assumed to be periodic with annual periodicity *T*, as the population considered here is a large population that is well mixed like the children of several large schools located close together [47]. The numerical values of the parameters are listed in Table 4.6.

**Table 4.6:** Measles Model Parameters [47], [99]

| Parameter | Description | Numerical Value |
|---|---|---|
| $b$ | Population influx/birth rate | 0.02 (life expectancy = 50 years) |
| $\mu$ | Death rate | 0.02 |
| $\alpha$ | Recovery rate | 100 |
| $\beta(t)$ | Contact rate: $\beta(t) = \beta_0 \left(1 + \varepsilon \sin\left(2\pi t / T\right)\right)$ | $\beta_0$ = 1800<br>$\varepsilon$ = 0.5<br>$T$ = 1 year |

### 4.8.3 Model Simulation

The nonlinear model in (4.38) was simulated in MATLAB® and Simulink® with the parameters in Table 4.6. The initial conditions were chosen based on the assumptions that a very small percentage of the population is infected, there is no recovery of the infected individuals, and $N(t) = S(t) + I(t) + R(t) = 1$. The initial conditions were $[0.999, 0.001, 0]$. The control variable $\psi(t)$ was assumed to be zero, as the inherent dynamics of the model is independent of the control input. The plots of the states with respect to time are displayed in Figure 4.21.

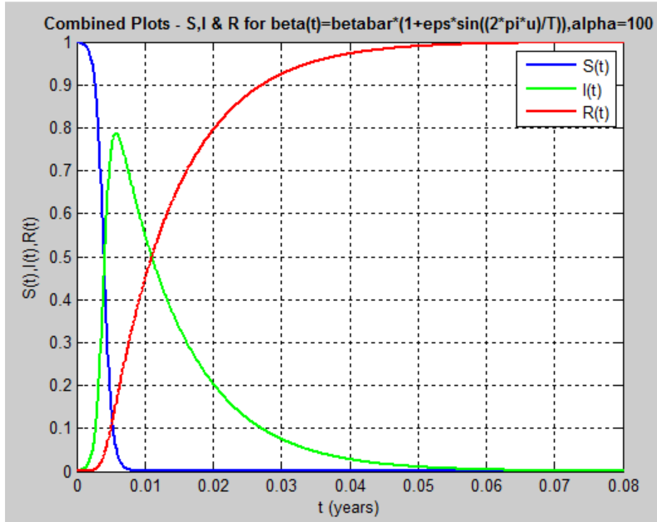


**Figure 4.21:** State responses of the measles model ( $\beta(t) = \beta_0(1+\varepsilon\sin(2\pi t/T))$ )

### 4.8.4 Linearization and Eigenvalues

The presence of slow and fast dynamics couldn't be inferred from the system responses (Figure 4.21), and therefore its eigenvalues were evaluated. The nonlinear model was linearized at various instants of time, and the results obtained indicated some discrepancies in the eigenvalues. Table 4.9 displays the eigenvalues obtained after linearization. The eigenvalues obtained for time instants, $t = 1$ and $t = 2$, displayed only two eigenvalues for a $(3\times3)$ system matrix *A*. This was an unexpected result from the MATLAB® simulations, and the version of the software used then was recalled to be 'R2007b'.

**Table 4.7**: Linearization of measles model at various time instants

| **Time instant 't' in years** | 0 | 0.004 | 0.006 | 0.01 | 0.03 | 0.06 | 0.1 | 1 | 2 |
|---|---|---|---|---|---|---|---|---|---|
| **Eigenvalues** | -0.02<br>0.0861<br>1700 | -0.02<br>-2.5+ 288i<br>-2.5 - 288i | -0.02<br>-106<br>-1360 | -0.02<br>-100<br>-1030 | -0.02<br>-100<br>-147 | -0.02<br>-8.19<br>-99 | -0.02<br>-0.199<br>-97.2 | -0.02<br>-65.8 | -0.02<br>-30.8 |

To investigate further on this discrepancy, one of the model parameters was modified to see if the system gives appropriate eigenvalues, i.e. 3 sets of eigenvalues for all time instants. The contact rate parameter, $\beta(t)$ was changed to a constant value from a sinusoidal periodic function, i.e. $\beta(t) = \beta_0 = 1800$. The eigenvalues were evaluated again, and are provided in Table 4.8. The system responses were also observed for this case and did not seem to vary much from that of the periodic contact rate's case (Figure 4.22).

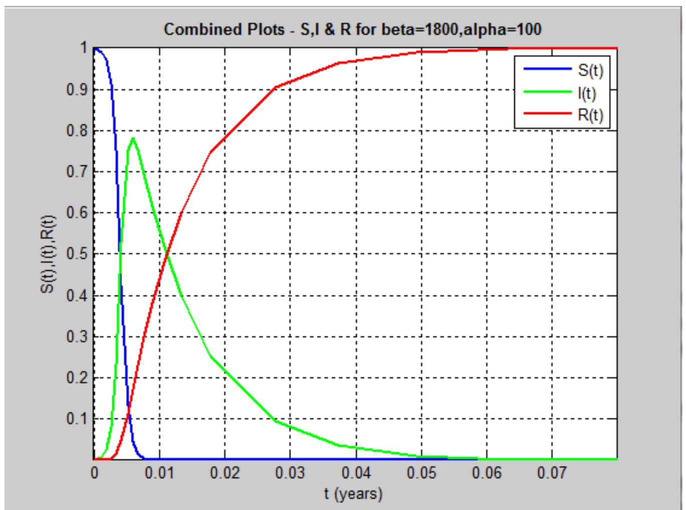


**Figure 4.22:** State responses of the measles dynamic model with $\beta(t) = 1800$

**Table 4.8**: Linearization of measles model with $\beta(t) = 1800$

| **Time instant 't' in years** | 0 | 0.004 | 0.006 | 0.01 | 0.03 | 0.06 | 0.1 | 1 | 2 |
|---|---|---|---|---|---|---|---|---|---|
| **Eigenvalues** | 0<br>0.106<br>1700 | 0<br>15.9 + 283i<br>15.9 – 283i | 0<br>-106<br>-1320 | 0<br>-100<br>-999 | 0<br>-100<br>-135 | 0<br>-6<br>-100 | 0<br>-0.124<br>-100 | 0<br>-100 | 0<br>-0.298<br>-100 |

The new eigenvalues indicated that for time $t = 2$, there were 3 eigenvalues, but for $t = 1$, there were only two eigenvalues. Also another observation made was that one of the eigenvalues was zero for all time constants. The MATLAB code was 'run' several times with different solvers (variable and fixed step) but the same results were repeated. The discrepancies in the results might be associated with the specific MATLAB version and the toolboxes that were available at that time. The author recalls that during the initial research work in life sciences, a few mathematical models were shortlisted for pursuing research, and measles and HIV models were a priority. The technical difficulty with the measles model led to continuation of research with the HIV model.

The measles model was revisited after completion of HIV research and the eigenvalue analysis was performed again with the current MATLAB® version (used for transmission line and HIV research), 'R2013a'. The linearization m-file is run again in the new version for both periodic and constant cases of contact rate, $\beta(t)$, with no code modifications, and the results are observed to be more appropriate and relevant. There are three sets of eigenvalues as expected for a 3$^{rd}$ order system, at all time instants, and all of them are non-zero. The results are provided in Table 4.9.

**Table 4.9**: Linearization results of measles model with MATLAB®- R2013a

| **Time instant '*t*'** (in years) | **Eigenvalues** | **Eigenvalues** |
|---|---|---|
| | Periodic contact rate $\beta(t)=\beta_0\left(1+\varepsilon\sin\left(2\pi t/T\right)\right)$ | Constant contact rate $\beta(t)=1800$ |
| $t$ = 0 | -0.02<br>0.0861<br>1696.3 | -0.02<br>0.0861<br>1696.3 |
| $t$ = 0.004 | -0.02<br>-2.4961+ 288i<br>-2.4961 - 288i | -0.02<br>15.912+ 282.62i<br>15.912+ 282.62i |
| $t$ = 0.006 | -0.02<br>-105.84<br>-1358.4 | -0.02<br>-106.43<br>-1323.5 |
| $t$ = 0.01 | -0.02<br>-100.08 | -0.02<br>-100.09 |

| **Time instant '*t*'** (in years) | **Eigenvalues** | **Eigenvalues** |
|---|---|---|
| | Periodic contact rate $\beta(t)=\beta_0\left(1+\varepsilon\sin\left(2\pi t/T\right)\right)$ | Constant contact rate $\beta(t)=1800$ |
| | -1027.9 | -999.47 |
| $t$ = 0.03 | -0.02<br>-100.4<br>-147.35 | -0.02<br>-100.4<br>-134.98 |
| $t$ = 0.06 | -0.02<br>-8.192<br>-98.98 | -0.02<br>-6.9251<br>-99.118 |
| $t$ = 0.1 | -0.02<br>-0.199<br>-97.23 | -0.02<br>-0.155<br>-97.81 |
| $t$ = 1 | -0.02<br>-65.8<br>-0.02 | -0.02<br>-65.75<br>-0.02 |
| $t$ = 2 | -0.02<br>-30.8<br>-0.02 | -0.02<br>-30.788<br>-0.02 |

The eigenvalues clearly indicates time scale behavior, and SPaTS methods can be easily applied for the measles model. The design of optimal vaccination schemes through time scale analysis and synthesis is a topic of future research.

## 4.9 Conclusion

A time domain model describing the dynamics of HIV infection is presented, and is analyzed for its inherent time scale behavior. The presence of time scales is identified through linearization and non-dimensionalization procedures, which qualified the HIV model for application of SPaTS methods. Acknowledged in literature for its model order reduction, stiffness relief properties, and flexibility with control laws, SPaTS methods are applied for the synthesis of an optimal HIV treatment strategy in this study. The simulation results manifests the effectiveness of this method in that comparable control was achieved with the lower order slow and fast controllers (in the time scale approach) compared to the conventional full order design. Lower order control laws translate to simple treatment plans that can be implemented in practice.

Even though mathematical modeling, experimental data and clinical data analysis were critical in transforming this fatal disease to a chronically managed disease, many aspects of the disease still remains unknown today. Extensive models incorporating various aspects of HIV dynamics might offer better insights towards inhibiting viral production. One example is the model incorporating the dynamics of the immune system, specifically the CD8+ 'killer' T cells which are beneficial towards investigating Structured Treatment Interruptions (STI). Development of control laws with such detailed models demand substantial computational efforts, and SPaTS methods could assist with the design of feasible control strategies.

Eradicating HIV from the body or assisting the body to fight the infection remains the ultimate goal. Future work would investigate revision of the current model to incorporate the immune system dynamics for a STI approach, which enhances the immune system responses to decimating the virus in the body. Analysis and design of measles model is another area of future research in the area of Life Sciences, where time scale methods will be applied for design of optimal vaccination schemes for controlling the disease transmission.

# Chapter 5

# Summary, Conclusions and Future Work

## 5.1 Summary and Conclusions

In this Dissertation, dynamic models of an overhead power transmission line and an HIV infection were analyzed. Nonlinear state space models were used for describing the dynamical processes. The eigenvalues of the linearized system were observed to be in distinct groups which indicated that the system had inherent slow and fast dynamics. In the transmission line model, time scale behavior was by virtue of the *slow* temperature dynamics and the *fast* electrical dynamics, whereas in the HIV infection model, it was due to the *slow* dynamics of the uninfected T cells compared to the very *rapid* viral dynamics. This made, the selected models, prime candidates for time scale analysis and design.

The SPaTS theory was very effective in designing linear optimal controllers with reduced model orders, for both transmission line and HIV dynamics.

1) In the case of transmission lines, a second order linear model was decoupled into two $1^{st}$ order, independent slow and fast subsystems. LQR optimal controllers were designed with these reduced order models, with the control objective of minimizing perturbations in transmission lines, which could arise from loading of electric motors or abrupt changes in source voltages or lighting strikes to the line. The performance of the time scale LQR design was evaluated by comparing the linear model's performance to that of a general full order design.

2) For the HIV infection model, a third order linear system was decoupled into a 1st and 2nd order, independent slow and fast subsystems, respectively. A long term treatment strategy incorporating LQR optimal control for maintaining the patient at steady state levels was investigated, with the objective of minimizing any deviations from the steady state values to zero. Time scale synthesis of the long term strategy was performed where the composite (slow + fast) control was fed back to the original nonlinear HIV model, to test its efficacy in maintaining the patient at steady state values (long term treatment strategy).

3) In both the cases, it was seen from simulation results that the performance of the reduced-order control matched the performance of the full order control very closely. These results hold far reaching implications in that, SPaTS could be used to reduce the very high model dimensions into lower order subsystems which would significantly reduce online and offline computation requirements. The stiffness associated with time scale systems is greatly reduced by the separation procedure, and this enhances the computational efficacy of control designs. Also, the independent slow and fast controllers allow for parallel and distributed processing of information with corresponding sampling rates i.e. slow system with slow sampling rate and fast system with fast sampling rate.

(a) In the context of transmission lines, this would imply that SPaTS methods would be well-suited for designing software controllers for DLR technology that can be implemented real-time. SCADA systems which form the backbone of modern industrial processes will be a key component of the evolving smart grid, for real-time monitoring, management and control of power transmission. The online controllers in SCADA systems for calculating real-time ampacity and corresponding line temperatures could benefit from the SPaTS design methods as the reduced order controllers offer significant computational savings compared to their full order counterparts.

(b) For the HIV model, the lower order control laws translate to simpler treatment schemes compared to the higher order control laws that are complex and difficult to implement.

4) Furthermore, when it comes to reliability of the control system, time scale synthesis provides more reliability with two controllers for subsystems instead of one central controller for the original system. The simulation results indicated that the performance of a transmission line model with a single controller, either slow or fast, by itself gives a performance nearly close to that with the combined (composite) controller performance. The reliability feature of the time scale synthesis becomes very significant for transmission lines in the event of faults in the line or controller failure. The multiple controllers in place are able to keep the system stable while the other controller has failed due to a fault or due to malicious cyber-attacks.

## 5.2 Future Work

In this study, several strengths of the SPaTS method are presented: decoupling of slow and fast dynamics, model order reduction while preserving system dynamics which facilitated reduction in online and offline computational requirements, processing slow subsystems with low sampling rate and fast subsystems with higher sampling rate and increased reliability of systems with two independent controllers for the subsystems.

However, the controller design studied here was limited in scope, as it was applied to a linear system only. This is due to the fact that decoupling of slow and fast subsystems is currently possible only for linear singularly perturbed systems. For optimal regulation and tracking of nonlinear systems, the closed-loop optimal control strategies are obtained using State-Dependent Differential or Algebraic Riccati Equations (SD-DRE or ARE) for finite and infinite horizon cases [100]. A topic for future investigation is to apply the theory of SPaTS to closed-loop nonlinear optimal control problems using SD-DRE technique.

Furthermore, detailed models of medium and long length transmission lines with distributed parameter modeling would be considered in future research for any unaccounted line current dynamics to enhance the computational accuracy of line ampacity levels. Also, integration of forecasted weather information into the existing time domain models of transmission lines would be a potential enhancement for the GLASS software at INL. Comprehensive power system models for transient analysis studies (incorporating generator, transmission line and load dynamics) would be another interesting area for the application of SPaTS methods.

Another potential area of interest would be the investigation of optimal treatment strategies for HIV infection where models incorporate *stochastic* components of viral dynamics and the host's immune system ($CD8^+$ T cell) dynamics. This would offer better insights into the viral dynamics and the host interactions, and would help in designing STI schemes for controlling the HIV infection. Investigation of SPaTS in developing optimal control strategies for measles is another avenue for future research in Life Sciences.

# Appendix A

## A.1 Transmission Line Model Data

| | | |
|---|---|---|
| Conductor type | ACSR – Drake 26/7<br>(Aluminum Conductor Steel Reinforced) -<br>26 outer Aluminum conductors & 7 Steel<br>core conductors | 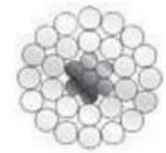 |

**Table A.1:** Parameter values used in the transmission line model [3]

| ***Property*** | ***Variable*** | ***Value*** |
|---|---|---|
| Line length | *len* | 60 km |
| Wind speed | $v_w$ | 0.61m/s |
| Projected area of conductor ($m^2$/linear m) | $A'$ | 0.02814 m |
| Solar absorptivity | $\alpha$ | 0.8 |
| Emissivity | $\varepsilon$ | 0.8 |
| Ambient air temperature | $T_a$ | 40 °C |
| Conductor outside diameter | $D_0$ | 28.14mm |
| Resistance @ low temperature | $R(T_{low})$ | *R(25 °C)* = 7.283 10-5 Ω/m |
| Resistance @ high temperature | $R(T_{high})$ | *R(75 °C)* = 8.688 10-5 Ω/m |
| Azimuth of line - east to west direction | $Z_l$ | $Z_l$ = 90° |
| Latitude | *Lat* | 30° North |
| Solar altitude | $H_c$ | Calculated for 11:00 am on June 10 (Day 161) |
| Day of the year | *N* | 161 |
| Line elevation | $H_e$ | 0 m |
| Hour angle | $\omega$ | -15° |
| Mass per unit length of aluminum | $m_{Al}$ | 1.116 kg/m |
| Mass per unit length of steel | $m_{Steel}$ | 0.5119 kg/m |
| Specific heat of aluminum | $C_{p,Al}$ | 955 J/kg .°C |
| Specific heat of steel | $C_{p,Steel}$ | 476 J/kg .°C |
| Angle between wind and conductor axis | $\phi$ | 90° |
| Load resistance | $R_{load}$ | 100 Ω |

| *Property* | *Variable* | *Value* |
|---|---|---|
| Line Inductance | *L* | $6.565 * 10^{-7}$ H – *Calculated from ACSR Datasheet* [101] |

| **Line Inductance Calculation** |
|---|
| $L = 2\times10^{-7}\ln\left(\dfrac{D_m}{GMR}\right)\times1609\ \Omega/\text{mile}$<br><br>Using $D_m$ = 1ft and GMR = 0.0375 ft from the datasheet in Table A.2 and converting units to per meter, the value of $L$ was found to be $6.565\times10^{-7}H$. |

## A.2 Data Sheet for ACSR – Drake 26/7 Conductor [102]

**Table A.2**: ACSR 795 kcmil 26/7 Datasheet – Inductance and GMR Information

**Aluminum Conductor Steel Reinforced**

**Electrical Properties**

| | SIZE & STRANDING | | RESISTANCE | | | | 60 HZ REACTANCE 1 FOOT EQUIVALENT SPACING | | | |
|---|---|---|---|---|---|---|---|---|---|---|
| | | | DC (Ohms/1000 Ft.) | AC-60-HZ(Ohms/1000 Ft.) | | | | Inductive (Ohms/1000 Ft.) | | |
| CODE WORD | AWG or kcmil | Aluminum/ Steel | @20° | @25° C | @50° C | @75° C | Capacitive (Megohms-1000 Ft.) | @25° C | @50° C | @75° C |
| TURKEY | 6 | 6/1 | 0.6419 | 0.6553 | 0.750 | 0.8159 | 0.7513 | 0.1201 | 0.1390 | 0.1439 |
| SWAN | 4 | 6/1 | 0.4032 | 0.4119 | 0.4794 | 0.5218 | 0.7149 | 0.1152 | 0.1314 | 0.1369 |
| SWANATE | 4 | 7/1 | 0.3989 | 0.4072 | 0.4633 | 0.5165 | 0.7102 | 0.11533 | 0.1239 | 0.1303 |
| SPARROW | 2 | 6/1 | 0.2534 | 0.2591 | 0.3080 | 0.3360 | 0.6785 | 0.1100 | 0.1235 | 0.1277 |
| SPARATE | 2 | 7/1 | 0.2506 | 0.2563 | 0.2966 | 0.3297 | 0.6737 | 0.1081 | 0.1176 | 0.1206 |
| ROBIN | 1 | 6/1 | 0.2011 | 0.2059 | 0.2474 | 0.2703 | 0.6600 | 0.1068 | 0.1191 | 0.1224 |
| RAVEN | 1/0 | 6/1 | 0.1593 | 0.1633 | 0.1972 | 0.2161 | 0.6421 | 0.1040 | 0.1138 | 0.1163 |
| QUAIL | 2/0 | 6/1 | 0.1265 | 0.1301 | 0.1616 | 0.1760 | 0.6241 | 0.1017 | 0.1117 | 0.1135 |
| PIGEON | 3/0 | 6/1 | 0.1003 | 0.1034 | 0.1208 | 0.1445 | 0.6056 | 0.0992 | 0.1083 | 0.1095 |
| PENGUIN | 4/0 | 6/1 | 0.0795 | 0.0822 | 0.1066 | 0.1157 | 0.5966 | 0.0964 | .01047 | 0.1053 |
| | | | | | | | | Inductive (Ohms/1000 Ft.) | GMR (Ft.) | |
| WAXWING | 266.8 | 18/1 | 0.0644 | 0.0657 | 0.0723 | 0.0788 | 0.576 | 0.0934 | 0.0197 | |
| PARTRIDGE | 266.8 | 26/7 | 0.0637 | 0.0652 | 0.0714 | 0.0778 | 0.565 | 0.0881 | 0.0217 | |
| MERLIN | 336.4 | 18/1 | 0.0510 | 0.0523 | 0.0574 | 0.0625 | 0.560 | 0.0877 | 0.0221 | |
| LINNET | 336.4 | 26/7 | 0.0506 | 0.0517 | 0.0568 | 0.0619 | 0.549 | 0.0854 | 0.0244 | |
| ORIOLE | 336.4 | 30/7 | 0.0502 | 0.0513 | 0.0563 | 0.0614 | 0.544 | 0.0843 | 0.0255 | |
| CHICKADEE | 397.5 | 18/1 | 0.0432 | 0.0443 | 0.0487 | 0.0528 | 0.544 | 0.0856 | 0.0240 | |
| IBIS | 397.5 | 26/7 | 0.0428 | 0.0438 | 0.0481 | 0.0525 | 0.539 | 0.0835 | 0.0265 | |
| LARK | 397.5 | 30/7 | 0.0425 | 0.0434 | 0.0477 | 0.0519 | 0.533 | 0.0824 | 0.0277 | |
| PELICAN | 477.0 | 18/1. | 0.0360 | 0.0369 | 0.0405 | 0.0441 | 0.528 | 0.0835 | 0.0263 | |
| FLICKER | 477.0 | 24/7 | 0.0358 | 0.0367 | 0.0403 | 0.0439 | 0.524 | 0.0818 | 0.0283 | |
| HAWK | 477.0 | 26/7 | 0.0357 | 0.0366 | 0.0402 | 0.0438 | 0.522 | 0.0814 | 0.0290 | |
| HEN | 477.0 | 30/7 | 0.0354 | 0.0362 | 0.0389 | 0.0434 | 0.517 | 0.0803 | 0.0304 | |
| OSPREY | 556.5 | 18/1 | 0.0309 | 0.0318 | 0.0348 | 0.0379 | 0.518 | 0.0818 | 0.0284 | |
| PARAKEET | 556.5 | 24/7 | 0.0307 | 0.0314 | 0.0347 | 0.0377 | 0.512 | 0.0801 | 0.0306 | |
| DOVE | 556.5 | 26/7 | 0.0305 | 0.0314 | 0.0345 | 0.0375 | 0.510 | 0.0795 | 0.0313 | |
| EAGLE | 556.5 | 30/7 | 0.0300 | 0.0311 | 0.0341 | 0.0371 | 0.505 | 0.0786 | 0.0328 | |
| PEACOCK | 605.0 | 24/7 | 0.0282 | 0.0290 | 0.0378 | 0.0347 | 0.505 | 0.0792 | 0.0319 | |
| SWIFT | 636.0 | 36/1 | 0.0267 | 0.0281 | 0.0307 | 0.0334 | 0.509 | 0.0806 | 0.0300 | |
| KINGBIRD | 636.0 | 18/1 | 0.0269 | 0.0278 | 0.0306 | 0.0332 | 0.507 | 0.0805 | 0.0301 | |
| ROOK | 636.0 | 24/7 | 0.0268 | 0.0277 | 0.0300 | 0.0330 | 0.502 | 0.0786 | 0.0327 | |
| GROSBEAK | 636.0 | 26/7 | 0.0267 | 0.0275 | 0.0301 | 0.0328 | 0.500 | 0.0780 | 0.0335 | |
| EGRET | 636.0 | 30/19 | 0.0266 | 0.0273 | 0.0299 | 0.0326 | 0.495 | 0.0769 | 0.0351 | |
| FLAMINGO | 666.6 | 24/7 | 0.0256 | 0.0263 | 0.0290 | 0.0314 | 0.498 | 0.0780 | 0.0335 | |
| STARLING | 715.5 | 26/7 | 0.0238 | 0.0244 | 0.0269 | 0.0292 | 0.490 | 0.0767 | 0.0355 | |
| REDWING | 715.5 | 30/19 | 0.0236 | 0.0242 | 0.0267 | 0.0290 | 0.486 | 0.0756 | 0.0372 | |
| COOT | 795.0 | 36/1 | 0.0217 | 0.0225 | 0.0247 | 0.0268 | 0.492 | 0.0780 | 0.0335 | |
| TERN | 795.0 | 45/7 | 0.0216 | 0.0225 | 0.0246 | 0.0267 | 0.488 | 0.0764 | 0.0352 | |
| CUCKOO | 795.0 | 24/7 | 0.0215 | 0.0223 | 0.0243 | 0.0266 | 0.484 | 0.0763 | 0.0361 | |
| CONDOR | 795.0 | 54/7 | 0.0215 | 0.0222 | 0.0244 | 0.0265 | 0.484 | 0.0759 | 0.0368 | |
| DRAKE | 795.0 | 26/7 | 0.0214 | 0.0222 | 0.0242 | 0.0263 | 0.482 | 0.0756 | 0.0375 | |
| MALLARD | 795.0 | 30/19 | 0.0213 | 0.0220 | 0.0241 | 0.0261 | 0.477 | 0.0744 | 0.0392 | |
| RUDDY | 900.0 | 45/7 | 0.0191 | 0.0200 | 0.0218 | 0.0237 | 0.479 | 0.0755 | 0.0374 | |

**Table A.3**: ACSR 795 kcmil 26/7 Datasheet – Inductance at different temperatures [101]

## Electrical Data for ACSR Conductors

| | | Resistance | | | | Reactance at 60 Hz ** | | | | |
|---|---|---|---|---|---|---|---|---|---|---|
| Codeword | Size (AWG/kcmil) | DC at 20°C (ohm/kft) | AC at 25°C (ohm/kft) | AC at 50°C (ohm/kft) | AC at 75°C (ohm/kft) | Capacitive (megohm-kft) | Inductive at 25°C (ohm/kft) | Inductive at 50°C (ohm/kft) | Inductive at75°C (ohm/kft) | Ampacity* (A) |
| Turkey | 6 | 0.642 | 0.655 | 0.750 | 0.816 | 0.751 | 0.120 | 0.139 | 0.144 | 105 |
| Swan | 4 | 0.403 | 0.412 | 0.479 | 0.522 | 0.715 | 0.115 | 0.131 | 0.137 | 140 |
| Swanate | 4 | 0.399 | 0.407 | 0.463 | 0.516 | 0.710 | 0.113 | 0.124 | 0.130 | 140 |
| Sparrow | 2 | 0.253 | 0.259 | 0.308 | 0.336 | 0.678 | 0.110 | 0.123 | 0.128 | 185 |
| Sparate | 2 | 0.251 | 0.256 | 0.297 | 0.330 | 0.674 | 0.109 | 0.118 | 0.121 | 185 |
| Robin | 1 | 0.201 | 0.206 | 0.247 | 0.270 | 0.660 | 0.107 | 0.119 | 0.122 | 210 |
| Raven | 1/0 | 0.159 | 0.163 | 0.197 | 0.216 | 0.642 | 0.104 | 0.114 | 0.116 | 240 |
| Quail | 2/0 | 0.126 | 0.130 | 0.162 | 0.176 | 0.624 | 0.102 | 0.112 | 0.113 | 275 |
| Pigeon | 3/0 | 0.100 | 0.103 | 0.121 | 0.145 | 0.606 | 0.0992 | 0.108 | 0.109 | 315 |
| Penguin | 4/0 | 0.0795 | 0.0822 | 0.107 | 0.116 | 0.597 | 0.0964 | 0.105 | 0.105 | 365 |
| Waxwing | 266.8 | 0.0644 | 0.0657 | 0.0723 | 0.0788 | 0.576 | 0.0903 | 0.0903 | 0.0903 | 445 |
| Partridge | 266.8 | 0.0637 | 0.0652 | 0.0714 | 0.0778 | 0.565 | 0.0881 | 0.0881 | 0.0881 | 455 |
| Merlin | 336.4 | 0.0510 | 0.0523 | 0.0574 | 0.0625 | 0.560 | 0.0826 | 0.0826 | 0.0826 | 515 |
| Linnet | 336.4 | 0.0506 | 0.0517 | 0.0568 | 0.0619 | 0.549 | 0.0854 | 0.0854 | 0.0854 | 530 |
| Oriole | 336.4 | 0.0502 | 0.0513 | 0.0563 | 0.0614 | 0.544 | 0.0843 | 0.0843 | 0.0843 | 530 |
| Chickadee | 397.5 | 0.0432 | 0.0443 | 0.0487 | 0.0528 | 0.544 | 0.0856 | 0.0856 | 0.0856 | 575 |
| Ibis | 397.5 | 0.0428 | 0.0438 | 0.0481 | 0.0525 | 0.539 | 0.0835 | 0.0835 | 0.0835 | 590 |
| Pelican | 477 | 0.0360 | 0.0369 | 0.0405 | 0.0441 | 0.528 | 0.0835 | 0.0835 | 0.0835 | 640 |
| Flicker | 477 | 0.0358 | 0.0367 | 0.0403 | 0.0439 | 0.524 | 0.0818 | 0.0818 | 0.0818 | 670 |
| Hawk | 477 | 0.0357 | 0.0366 | 0.0402 | 0.0438 | 0.522 | 0.0814 | 0.0814 | 0.0814 | 660 |
| Hen | 477 | 0.0354 | 0.0362 | 0.0398 | 0.0434 | 0.517 | 0.0803 | 0.0803 | 0.0803 | 660 |
| Osprey | 556.5 | 0.0309 | 0.0318 | 0.0348 | 0.0379 | 0.518 | 0.0818 | 0.0818 | 0.0818 | 710 |
| Parakeet | 556.5 | 0.0307 | 0.0314 | 0.0347 | 0.0377 | 0.512 | 0.0801 | 0.0801 | 0.0801 | 720 |
| Dove | 556.5 | 0.0305 | 0.0314 | 0.0345 | 0.0375 | 0.510 | 0.0795 | 0.0795 | 0.0795 | 730 |
| Rook | 636 | 0.0268 | 0.0277 | 0.0303 | 0.0330 | 0.502 | 0.0786 | 0.0786 | 0.0786 | 780 |
| Grosbeak | 636 | 0.0267 | 0.0275 | 0.0301 | 0.0328 | 0.499 | 0.0780 | 0.0780 | 0.0780 | 790 |
| Drake | 795 | 0.0214 | 0.0222 | 0.0242 | 0.0263 | 0.482 | 0.0756 | 0.0756 | 0.0756 | 910 |
| Tern | 795 | 0.0216 | 0.0225 | 0.0246 | 0.0267 | 0.488 | 0.0769 | 0.0769 | 0.0769 | 890 |
| Rail | 954 | 0.0180 | 0.0188 | 0.0206 | 0.0223 | 0.474 | 0.0748 | 0.0748 | 0.0748 | 970 |
| Cardinal | 954 | 0.0179 | 0.0186 | 0.0205 | 0.0222 | 0.470 | 0.0737 | 0.0737 | 0.0737 | 990 |
| Curlew | 1033.5 | 0.0165 | 0.0172 | 0.0189 | 0.0205 | 0.464 | 0.0729 | 0.0729 | 0.0729 | 1040 |
| Bluejay | 1113 | 0.0155 | 0.0163 | 0.0178 | 0.0193 | 0.461 | 0.0731 | 0.0731 | 0.0731 | 1070 |
| Bittern | 1272 | 0.0135 | 0.0144 | 0.0157 | 0.0170 | 0.451 | 0.0716 | 0.0716 | 0.0716 | 1160 |
| Lapwing | 1590 | 0.0108 | 0.0117 | 0.0128 | 0.0138 | 0.434 | 0.0689 | 0.0689 | 0.0689 | 1340 |
| Bluebird | 2156 | 0.00801 | 0.00903 | 0.00977 | 0.0105 | 0.409 | 0.0652 | 0.0652 | 0.0652 | 1610 |

* Ampacity is with sun and wind at 2 ft/s
** Reactance at 1 foot equivalent spacing

Nexans
5

# References

[1] U.S. Department of Energy, "Economic Benefits Of Increasing Electric Grid Resilience To Weather Outages," 2013. [Online]. Available: energy.gov.

[2] "Smart Grid System Report," U.S. Department of Energy, 2010.

[3] "IEEE Standard 738 - Standard for calculating the current temperature relationship of bare overhead line conductors," 2012.

[4] "Energy.gov," Office of Energy Efficiency & Renewable Energy, May 2015. [Online]. Available: https://energy.gov/eere/wind/articles/wind-concurrent-cooling-could-increase-power-transmission-potential-much-40. [Accessed March 2017].

[5] J. P. Gentle, W. L. Parsons, M. R. West and S. Jaison, "Evolving Innovations in Technology – Grid System Planning for Wind," December 2014. [Online]. Available: https://www.windsim.com/documentation/UM_Americas_2014/05-WindSim_Americas_Annual_Meeting_2014_INL_Gentle.pdf.

[6] Image, "Neural Energy Consulting," July 2015. [Online]. Available: http://www.neuralenergy.info/2009/06/circuit-ratings.html. [Accessed October 2017].

[7] J. Gentle, K. Myers, T. Baldwin, I. West, K. Hart, B. Savage and M. Ellis, "Concurrent Wind Cooling in Power Transmission Lines," in *2012 Western Energy Policy Research Conference*, Boise, 2012.

[8] J. P. Gentle, W. L. Parsons, M. R. West and S. Jaison, "Modernizing An Aging Infrastructure Through Real-Time Transmission Monitoring," in *2015 IEEE Power*

*& Energy Society General Meeting*, Denver, CO, 2015.

[9] College of Fellows, American Institute for Medical and Biological Engineering, "Medical and Biological Engineering in the Next 20 Years: The Promise and the Challenges," *IEEE Transactions On Biomedical Engineering,* vol. 60, no. 7, pp. 1767 - 1775, 2013.

[10] WHO, "Global Health Estimates (GHE)," December 2016. [Online]. Available: http://www.who.int/healthinfo/global_burden_disease/en/. [Accessed August 2017].

[11] A. S. Perelson and P. W. Nelson, "Mathematical Analysis of HIV-1 Dynamics in Vivo," *1999 Society for Industrial and Applied Mathematics,* vol. 41, no. 1, pp. 3 - 44, 1999.

[12] "WHO Fact Sheet- The top 10 causes of death," World Health Organization, January 2017. [Online]. Available: http://www.who.int/mediacentre/factsheets/fs310/en/. [Accessed September 2017].

[13] UNAIDS, "Fact Sheet 2017," 2017. [Online]. Available: http://www.unaids.org/en/resources/fact-sheet. [Accessed September 2017].

[14] UNAIDS, "Core Epidimeolgy Slides 2017," June 2017. [Online]. Available: http://www.unaids.org/en/resources/documents/2017/20170720_Core_epidemiology_slides. [Accessed September 2017].

[15] UNAIDS, "'Ending AIDS: Progress towards the 90-90-90 targets'," July 2017. [Online]. Available: http://www.unaids.org/en/resources/documents/2017/20170720_Global_AIDS_upd

ate_2017. [Accessed September 2017].

[16] "HIV/AIDS," National Institute on Drug Abuse (NIDA), July 2012. [Online]. Available: https://www.drugabuse.gov/publications/research-reports/hivaids/what-haart. [Accessed September 2017].

[17] AVERT, "Global HIV and AIDS Statistics," AVERT, August 2017. [Online]. Available: https://www.avert.org/global-hiv-and-aids-statistics. [Accessed September 2017].

[18] R. V. Culshaw, "Review of HIV models: The role of the natural immune response and implications for treatment," *Journal of Biological Systems,* vol. 12, no. 2, p. 123–135, 2004.

[19] F. deSouza, "Modeling the dynamics of HIV-1 and CD4 and CD8 lymphocytes," *IEEE Engineering in Medicine and Biology Magazine*, vol. 18, no. 1, 1999.

[20] D. Wodarz and M. A. Nowak, "Mathematical models of HIV pathogenesis and treatment.," *BioEssays: News and reviews in molecular, cellular and developmental biology*, vol. 24, p. 1178–1187, 2002.

[21] A. M. Croicu, "Short and Long Term Optimal Control of a Mathematical Model for HIV Infection of CD4+T Cells," *Bulletin of Mathematical Biology,* vol. 77, no. November 2015, p. 2035–2071, 2015.

[22] M. M. Hadjiandreou, R. Conejeros and D. I. Wilson, "Long-term HIV dynamics subject to continuous therapy and structured treatment interruptions," *Chemical Engineering Science*, vol. 64, no. 7, pp. 1600-1617, 2009.

[23] Y. Zhou, Y. Liang and J. Wu, "An optimal strategy for HIV multitherapy," *Journal*

*of Computational and Applied Mathematics*, vol. 263, pp. 326-337, 2014.

[24] J. Karrakchou, M. Rachik and S. Gourari, "Optimal control and infectiology: application to an HIV/AIDS model," *Applied Mathematics and Computation,* vol. 177, p. 807–818, 2006.

[25] V. Radisavljevic-Gajic, "Optimal Control of HIV-Virus Dynamics," *Annals of Biomedical Engineering*, vol. 37, no. 6, p. 1251–1261, 2009.

[26] M. A. L. Caetano and T. Yoneyama, "Short and long period optimization of drug doses in the treatment of AIDS," *Annals of the Brazilian Academy of Sciences,* vol. 74, no. 3, p. 379–392, 2002.

[27] J. M. Murray, G. Kaufmann, A. D. Kelleher and D. A. Cooper, "A Model of primary HIV-1 infection," *Mathematical Biosciences,* vol. 154, pp. 57-85, 1998.

[28] H. R. Joshi, "Optimal control of an HIV immunology model," *Optimal Control Applications and Methods,* vol. 23, p. 199–213, 2002.

[29] J. H. Ko, W. H. Kim and C. C. Chung, "Optimized Structured Treatment Interruption for HIV Therapy and Its Performance Analysis on Controllability," in *43rd IEEE Conference on Decision and Control*, Atlantis, Bahamas, 2004.

[30] H. T. Banks, H.-D. Kwon, J. A. Toivanen and H. T. Tran, "A state-dependent Riccati equation-based estimator approach for HIV feedback control," *Optimal Control Applications and Methods,* vol. 27, p. 93–121, 2006.

[31] S. Wang, P. Hottz, M. Schechter and L. Rong, "Modeling the Slow CD4+ T Cell Decline in HIV-Infected Individuals," *PLOS Computational Biology,* vol. 11, no. 12, p. e1004665, 2015.

[32] R. J. deBoer, "Time Scales of CD4+ T Cell Depletion," *PLOS Medicine,* vol. 4, no. 5, p. e193, 2007.

[33] A. Yates, J. Stark, N. Klein, R. Antia and R. Callard, "Slow Depletion of Memory CD4+ T Cells in HIV Infection," *Public Library of Science (PLOS) Medicine*, vol. 4, no. 5, p. e177, 2007.

[34] D. S. Naidu, "Singular perturbations and Time Scales in Control Theory and Applications: An Overview," *Dynamics of Continuous, Discrete and Impulsive Systems Series,* vol. 9, no. Series B, pp. 233-278, 2002.

[35] Y. Zhang, D. S. Naidu, C. Cai and Y. Zou, "Singular Perturbations and Time Scales in Control Theory and Applications: An Overview 2002-2012," *International Journal of Information Systems Sciences (IJISS),* vol. 9, pp. 1-36, 2014.

[36] P. W. Sauer, "Time-Scale Features and Their Applications in Electric Power System Dynamic Modeling and Analysis," in *American Control Conference*, CA, 2011.

[37] H. M. Nguyen and D. S. Naidu, "Singular Perturbation Analysis and Synthesis of Wind Energy Conversion Systems under Stochastic Environments," in *Proceedings of the 12th WSEAS International Conference on Advances in Systems Theory, Signal Processing and Computational Science*, Turkey, 2012.

[38] S. Jaison, D. S. Naidu and D. Zydek, "Time Scale Analysis and Synthesis of Deterministic and Stochastic Wind Energy Conversion Systems," *WSEAS Transactions on Systems and Control,* Vols. 189-198, 2014.

[39] J. H. Chow, J. R. Winkelman, M. A. Pai and P. W. Sauer, "Singular perturbation

analysis of large-scale power systems," *International Journal of Electrical Power & Energy Systems,* vol. 12, no. 2, pp. 117-126, 1990.

[40] O. Touhami, A. Mezouar, R. Ibtiouen and S. Mekhtoub, "Sliding Mode Control and Flux Observer For A Singularly Perturbed Model Of An Induction Machine," in *2004 IEEE International Conference on Industrial Technology (ICIT)*, Tunisia, 2004.

[41] Y. Chen and Y. Liu, "Summary of Singular Perturbation Modeling of Multi-time Scale Power Systems," in *2005 IEEE/PES Transmission and Distribution Conference & Exhibition*, Dalian, China, 2005.

[42] P. Li, B. H. Zhang, J. Shu, Z. Q. Bo and A. Klimek, "Research on order reduction of power system modeling for dynamic voltage stability analysis," in *IEEE PES Transmission and Distribution Conference and Exposition*, New Orleans, 2010.

[43] J. W. Kimball and P. T. Krein, "Singular perturbation theory for DC-DC converters and application to PFC converters.," *IEEE Transactions on Power Electronics,* vol. 23, no. 6, pp. 2970 - 2981, 2008.

[44] S. Celikovsky et. al., "Singular Perturbation Based Solution to Optimal Microalgal Growth Problem and its Infinite Time Horizon Analysis," in *47th IEEE Conference on Decision & Control*, 2008.

[45] S. Jayanthi and D. D. Vecchio, "Retroactivity Attenuation in Bio-molecular Systems Based on Timescale Separation," *IEEE Transactions on Automatic Control,* vol. 56, no. 4, pp. 748 - 761, 2011.

[46] S. Monfared, V. Krishnamurthy and B. Cornell, "Stochastic modeling and signal

processing of nano-scale protein-based biosensors," in *IEEE International Workshop on Genomic Signal Processing and Statistics*, Minneapolis, 2009.

[47] O. N. Owuor, M. Johannes and M. S. Kibet, "Optimal Vaccination Strategies in an SIR Epidemic Model with Time Scales," *Applied Mathematics,* vol. 4, pp. 1-14, 2013.

[48] B. Song, C. Castillo-Chavez and J. P. Aparicio, "Tuberculosis models with fast and slow dynamics: the role of close and casual contacts," *Mathematical Biosciences,* vol. 180, p. 187–205, 2002.

[49] "AIDSinfo - FDA-Approved HIV Medicines," U.S. Department of Health and Human Services, September 2017. [Online]. Available: https://aidsinfo.nih.gov/contentfiles/upload/HIV_Pill_Brochure.pdf. [Accessed September 2017].

[50] M. Barao and J. M. Lemos, "Nonlinear control of HIV-1 infection with a singular perturbation model," *Biomedical Signal Processing and Control,* vol. 2, no. 2007, p. 248–257, 2007.

[51] N. Bobko and J. P. Zubelli, "A singularly perturbed HIV model with treatment and antigenic variation," *Mathematical Biosciences and Engineering,* vol. 12, no. 1, pp. 1 - 21, 2015 .

[52] D. S. Naidu, Singular Perturbation Methodology in Control Systems, Peter Peregrinus Ltd., London, 1988.

[53] Z. Gajic and M. Lim, Optimal control of singularly perturbed linear systems and applications- High accuracy techniques, New York: Marcel Dekker, Inc., 2001.

[54] T. Grodt and Z. Gajic, "The Recursive Reduced-Order Numerical Solution of the Singularly Perturbed Matrix Differential Riccati Equation," *IEEE Transactions on Automatic Control*, vol. 33, no. 8, pp. 751-754, 1988.

[55] S. Jaison, D. S. Naidu and D. Zydek, "Time Scale Analysis and Synthesis of Wind Energy Conversion Systems," in *WSEAS Proceedings of the 4th International Conference on Circuits, Systems,Control, Signals (CSCS '13)*, Valencia, Spain, 2013.

[56] H. M. Nguyen, D. S. Naidu and S. H. Mousavinezhad, "H∞ Optimal Filtering and Control of Wind Energy Conversion Systems," in *2013 IEEE International Conference on Electro/Information Technology (EIT2013)*, Rapid City, SD, 2013.

[57] Y. Zhang, D. S. Naidu, C. Cai and Y. Zou, "Nonlinear Model Predictive Control for regulation of a class of Nonlinear Singularly Perturbed discrete-time systems," in *2014 7th International Symposium on Resilient Control Systems (ISRCS)*, Denver, CO, 2014.

[58] "MIT OpenCourseWare," August 2010. [Online]. Available: https://ocw.mit.edu/courses/aeronautics-and-astronautics/16-30-feedback-control-systems-fall-2010/. [Accessed October 2017].

[59] D. S. Naidu, Optimal Control Systems, CRC Press, 2003.

[60] "Nebraska Public Power District," [Online]. Available: http://www.nppd.com/assets/image15_large.jpg.

[61] Public Service Commission of Wisconsin, "Underground Electric Transmision Lines," [Online]. Available:

https://psc.wi.gov/thelibrary/publications/electric/electric11.pdf.

[62] Xcel Energy, "Overhead vs. Underground - Information about Undergrounding High-Voltage Transmission Lines," [Online]. Available: https://www.xcelenergy.com/staticfiles/xe/Regulatory/Transmission/OverheadvsUnderground.pdf. [Accessed 2016].

[63] Image, "Quora.com," Main Components of Overhead tr, June 2017. [Online]. Available: www.quora.com. [Accessed September 2017].

[64] M. Farzaneh, S. Farokhi and W. Chisholm, Electrical Design of Overhead Power Transmission Lines, McGraw-Hill Companies Inc., 2012.

[65] Aluminium Association, "Aluminium Electrical Conductor Handbook by the Aluminium Association," October 2017. [Online]. Available: http://www.rmjtcable.com/d/file/manual/Aluminium_Electrical_Conductor_Handbook.pdf. [Accessed November 2017].

[66] Image, "Overhead AAC/AAAC/ACSR/ACAR Bare Conductor," alibaba.com, [Online]. Available: https://www.alibaba.com/product-detail/Overhead-AAC-AAAC-ACSR-ACAR-Bare_60465546696.html. [Accessed September 2017].

[67] M. S. Mamis, A. Kaygusuz and M. Koksal, "State variable distributed-parameter representation of transmission line for transient simulations," *Turkish Journal of Electrical Engineering & Computer Sciences*, vol. 18, no. 1, pp. 31-42, 2010.

[68] M. S. Mamiş, "Discrete-Time State-Space Modeling of Distributed Parameter Transmission Line," in *EUROCON 2007 The International Conference on "Computer as a Tool"*, Warsaw, 2007.

[69] M. S. Mamis, "State-Space Transient Analysis of Single-Phase Transmission Lines with Corona," in *International Conference on Power Systems Transients (IPST)*, New Orleans, 2003.

[70] R. Ramírez-Betancoura, C. R. Fuerte-Esquivela and T. V. Cutsemb, "A two-time scale simulation for dynamic analysis of power systems," *Electric Power Systems Research*, vol. 83, no. 1, pp. 185-195, 2012.

[71] J. R. Winkelman, J. H. Chow, J. J. Allemong and P. V. Kokotovic, "Multi-Time-Scale Analysis of a Power System," *Automatica*, vol. 16, no. 1, pp. 35-43, 1980.

[72] L. de Andrade, H. Leite and M. de Leao, "Time-domain distributed parameters transmission line model for transient analysis," *Progress In Electromagnetics Research*, vol. 53, pp. 25-46, 2013.

[73] "Fact Sheet - General Line Ampacity State Solver (GLASS)," Idaho National Laboratory, [Online]. Available: http://www4vip.inl.gov/research/general-line-ampacity-state-solver/. [Accessed October 2017].

[74] "Electric Power Monthly," U.S. Energy Information Administration, June 2017. [Online]. Available: https://www.eia.gov/todayinenergy/detail.php?id=31632#. [Accessed October 2017].

[75] S. Jaison, "Thesis - Time Scale Analysis and Synthesis of Wind Energy Conversion Systems," Idaho State University, Pocatello, Idaho, 2012.

[76] A. B. Vasileva, "Asymptotic behavior of solutions to certain problems involving nonlinear ordinary differential equations containing a small parameter multiplying the highest derivatives," *Russian Mathematical Surveys*, vol. 18, pp. 13-84, 1963.

[77] D. Kirschner, "Using mathematics to understand HIV immune dynamics," *Notices of the American Mathematical Society (AMS)*, vol. 43, no. 2, pp. 191-202, February 1996.

[78] "AP Biology," [Online]. Available: http://carignanapbio.weebly.com/immune-system.html.

[79] "HIV/ AIDS: Recent advances 2016," Slideshare , [Online]. Available: https://www.slideshare.net/prashantshukla927/hiv-aids-recent-advances-2016. [Accessed 2017 September].

[80] "HIV-1 and HIV-2," AIDSMap, [Online]. Available: http://www.aidsmap.com/HIV-1-and-HIV-2/page/1322970/. [Accessed October 2017].

[81] "HIV Replication Cycle," National Institute of Allergy and Infectious Diseases (NIAID), May 2017. [Online]. Available: https://www.niaid.nih.gov/diseases-conditions/hiv-replication-cycle. [Accessed September 2017].

[82] U.S. Department of Health and Human Services, "AIDS Info," [Online]. Available: https://aidsinfo.nih.gov/contentfiles/lvguidelines/adultandadolescentgl.pdf. [Accessed August 2017].

[83] "Wikimedia Commons," March 2017. [Online]. Available: commons.wikimedia.org. [Accessed September 2017].

[84] V. Pirrone, N. Thakkar, J. M. Jacobson, B. Wigdahl and F. C. Krebs, "Combinatorial Approaches to the Prevention and Treatment," *Antimicrobial Agents and Chemotherapy of HIV-1 Infection*, vol. 55, no. 5, p. 1831–1842, 2011.

[85] A. S. Perelson and R. M. Ribeiro, "Modeling the within-host dynamics of HIV infection," *BMC Biology,* vol. 11, no. 1, p. #96, 2013.

[86] S. Butler, D. Kirschner and S. Lenhart, "Optimal control of chemotherapy affecting the infectivity of HIV," in *Advances in Mathematical Population Dynamics-Molecules, Cells and Man,* 1997.

[87] J. M. Gregio, M. A. L. Caetano and T. Yoneyama, "State estimation and optimal long period clinical treatment of HIV seropositive patients," *Annals of the Brazilian Academy of Sciences,* vol. 81, no. 1, pp. 3-12, 2009.

[88] T. Jang, H. Kwon and J. Lee, "Free Terminal Time Optimal Control Problem of an HIV Model Based on a Conjugate Gradient Method," *Bulletin of Mathematical Biology,* vol. 73, pp. 2408-2429, 2011.

[89] K. Fister, S. Lenhart and J. Mcnally, "Optimizing chemotherapy in an HIV model," *Electronic Journal of Differential Equations,* vol. 1998, no. 32, pp. 1-12, 1998.

[90] D. Wodarz, Killer Cell Dynamics: Mathematical and Computational Approaches, New York: Springer, 2007.

[91] M. Nowak and R. May, Virus Dynamics: Mathematical Principles of Immunology and Virology, Oxford: Oxford University Press, 2001.

[92] A. S. Perelson, D. E. Kirschner and R. De Boer, "Dynamics of HIV infection of CD4+ T cells," *Mathematical Biosciences,* vol. 114, pp. 81-125, 1993.

[93] G. Ledder, Mathematics for the Life Sciences - Calculus, Modeling, Probability, and Dynamical Systems, Springer, 2013.

[94] H.-D. Kwon, J. Lee and S.-D. Yang, "Optimal control of an age-structured model

of HIV infection," *Applied Mathematics and Computation*, vol. 219, no. 5, pp. 2766-2779, 2012.

[95] A. A. Momoh, M. O. Ibrahim, I. J. Uwanta and S. B. Manga, "Mathematical Model For Control Of Measles Epidemiology," *International Journal of Pure and Applied Mathematics,* vol. 87, no. 5, pp. 707-718, 2013.

[96] "Measles Fact Sheet," World Health Organization, July 2017. [Online]. Available: http://www.who.int/mediacentre/factsheets/fs286/en/. [Accessed October 2017].

[97] R. M. Anderson and R. May, Infectious Diseases of Humans Dynamics and Control, Oxford University Press, September 1992.

[98] H. W. Hethcote, "The mathematics of infectious diseases," *Society for Industrial and Applied Mathematics (SIAM) Review*, vol. 42, no. 4, pp. 599-653, 2000.

[99] N. O. Onyango and J. Müller, "Determination of optimal vaccination strategies using an orbital stability threshold from periodically driven systems," *Journal of Mathematical Biology*, vol. 68, no. 3, p. 763–784, 2014.

[100] A. M. A. Khamis, "Advanced Tracking Strategies for Linear and Nonlinear Control Systems: Theory and Applications," Idaho State University, Pocatello, 2014.

[101] Nexans, "https://www.nexans.us," 2003. [Online]. Available: http://www.nexans.us/eservice/US-en_US/fileLibrary/Download_540190082/US/files/BareOverhead. [Accessed November 2017].

[102] Alcan Cable, "www.cablejoints.co.uk," 2014. [Online]. Available: http://www.cablejoints.co.uk/upload/Overhead_Transmission_&_Distribution_Con

ductors___ACSR,_AAC,_AAAC___Alcan.pdf. [Accessed September 2017].